POLYTECHNIQUE MONTRÉAL
affiliée à l'Université de Montréal

Remote powering and data communication over a single inductive link for implantable medical devices

AREF TRIGUI
Département de génie éléctrique

Thèse présentée en vue de l'obtention du diplôme de *Philosophiæ Doctor*
Génie éléctrique

Mai 2020

POLYTECHNIQUE MONTRÉAL
affiliée à l'Université de Montréal

Cette thèse intitulée :

Remote powering and data communication over a single inductive link for implantable medical devices

présentée par **Aref TRIGUI**
en vue de l'obtention du diplôme de *Philosophiæ Doctor*
a été dûment acceptée par le jury d'examen constitué de :

Yves AUDET, président
Mohamad SAWAN, membre et directeur de recherche
Yvon SAVARIA, membre et codirecteur de recherche
Ahmed Chiheb AMMARI, membre et codirecteur de recherche
Frédéric LESAGE, membre
Ammar B. KOUKI, membre externe

DEDICATION

To my dear parents,

To my sister and stepbrother

To my nieces and my nephew

To my professors and teachers

To all my friends

To researchers on the field of wireless power and data transfer through inductive link, I did my best to popularize my research work and make the reading of this modest manuscript as easy and pleasant as possible

. . .

ACKNOWLEDGEMENTS

First and foremost, I would like to thank God, the Almighty, for his never-ending grace and blessing throughout my research work to complete the PhD successfully. *"And my success (in my task) can only come from ALLAH. In Him I trust, and unto Him I return."* – Quran(11:88)

Then I would like to express my deepest gratitude to my advisors, Professor Mohamad Sawan, Professor Yvon Savaria and Professor Ahmed Ammari for their valuable guidance and the continuous support throughout my Ph.D. Many thanks for their patience, helpful suggestions, and for providing me with all the necessary facilities. I am very grateful to their supervision and I owe them the greatest degree of appreciation.

My sincere thanks also go to the jury members namely Prof. Yves Audet, Prof. Frederic Lesage and Prof. Ammar Kouki for their time beside their busy schedules.

I express my deepest dept of gratitude as well to my colleague and friend Mohamed Ali for his valuable help in analog IC circuit design.

I owe much gratitude as well to my fellow students, technicians and staff of Polystim and GRM for their friendship and all of their help over years.

I also extend my thanks to the technician of the Elecrical engineering department Laurent Mouden for his technical assistance and his help in the assembly of prototypes. My thanks also go to the administrative staff, in particular to Marie-Yannick Laplante, Nathalie Lévesque, and Louise Clément.

I gratefully acknowledge the funding received towards my PhD from Natural Sciences and Engineering Research Council of Canada (NSERC) and Regroupement Stratégique en Microsystème du Québec (RESMIQ). Also, I would like to thank the Canadian Microelectronic Corporation (CMC) for the access to the large panoply of design tools that enabled the manufacturing of the IC chips and prototypes.

I would like to extend my heartiest thanks to my lovable parents, my father Mr. Brahim Trigui, my mother Mrs. Awatef Wali for nurturing me with moral values, taken care of me at every turn and moment of life and for encouraging me to go on every adventure, especially

this one.

I express as well my deepest dept of gratitude to my friends and roommates Sami Hached and Naoufel Ketata to be on my side in good and difficult times.

I also place on record, my sense of gratitude to one and all who, directly or indirectly, have lent their helping hand in this venture.

RÉSUMÉ

Les implants médicaux électroniques (Implantable Medical Devices - IMDs) sont notamment utilisés pour restaurer ou améliorer des fonctions perdues de certains organes. Ils sont capables de traiter des complications qui ne peuvent pas être guéries avec des médicaments ou par la chirurgie. Offrant des propriétés et des améliorations curatives sans précédent, les IMDs sont de plus en plus demandés par les médecins et les patients. En 2017, le marché mondial des IMD était évalué à 15,21 milliards de dollars. D'ici 2025, il devrait atteindre 30,42 milliards de dollars, soutenu par un taux de croissance annuel de 9,24% selon le nouveau rapport publié par Fior Markets. Cette expansion entraîne une augmentation des exigences pour assurer des performances supérieures, des fonctionnalités supplémentaires et une durée de vie plus longue. Ces exigences ne peuvent être satisfaites qu'avec des techniques d'alimentation avancées, un débit de données élevé et une électronique miniaturisée robuste. Construire des systèmes capables de fournir toutes ces caractéristiques est l'objectif principal d'un grand nombre de chercheurs.

Parmi plusieurs technologies sans fil, le lien inductif, qui consiste en une paire de bobines à couplage magnétique, est la technique sans fil la plus largement utilisée pour le transfert de puissance et de données. Cela est dû à sa simplicité, sa sécurité et sa capacité à transmettre à la fois de la puissance et des données de façon bidirectionnelle.

Cependant, il existe encore un certain nombre de défis concernant la mise en œuvre d'un tel système de transfert d'énergie et de données sans fil (Wireless Power and Data Transfer - WPDT system). Un défi majeur est que les exigences pour une efficacité de transfert d'énergie élevée et pour une communication à haut débit sont contradictoires. En fait, la bande passante doit être élargie pour des débits de données élevés, mais réduite pour une transmission efficace de l'énergie. Un autre grand défi consiste à réaliser un démodulateur fonctionnant à haute vitesse avec une mise en œuvre simple et une consommation d'énergie ultra-faible.

Dans ce projet, nous proposons et expérimentons un nouveau système WPDT dédié aux IMD permettant une communication à haute vitesse et une alimentation efficace tout en maintenant une faible consommation d'énergie, une petite surface de silicium et une mise en œuvre simple du récepteur. Le système proposé est basé sur un nouveau schéma de modulation appelé "Carrier Width Modulation (CWM)", ainsi que sur des circuits de modulation et de démodulation inédits. La modulation consiste en un coupe-circuit synchronisé du réservoir LC primaire pendant un ou deux cycles en fonction des données transmises.

Contrairement aux techniques de modulation conventionnelles, le débit de données de la modulation CWM proposée n'est pas limité par les facteurs de qualité des bobines primaires et secondaires. D'autre part, le démodulateur CWM proposé permet une démodulation à plus grande vitesse et une mise en œuvre simple, contrairement aux démodulateurs conventionnels pour un schéma de modulation similaire. Il offre également une large gamme de débits de données sous n'importe quelle fréquence sélectionnée de 10 à 31 MHz. La fonctionnalité du système WPDT proposé est prouvée à l'aide d'une implémentation hybride d'un démodulateur intégré et de composants discrets sur des circuits imprimés. Ce système permet un débit de données maximal de 3,33 Mb/s pour une puissance transmise maximale de 6,1 mW à une distance axiale de 1 cm entre les bobines. En raison de sa généricité, le système peut atteindre une tranmission de puissance de plus de 55 mW au détriment du débit de données. L'opérateur peut sélectionner le meilleur compromis entre la transmission de puissance et le débit de données en fonction de l'application ou du besoin, sans reconfigurer le récepteur.

Ce dernier comprend un étage de récupération d'énergie réalisé par des composants électroniques commerciaux et un démodulateur CWM intégré à très faible puissance fabriqué en technologie CMOS 130 nm. Il a une très petite surface de silicium de 2100 μm^2, consomme 16,9 μW dans les pires conditions et atteint des débits de données de 1/3 la fréquence de la porteuse. À une fréquence de 27,12 MHz, un débit de données de 9,04 Mb/s est atteint pour une consommation énergétique de seulement 13,68 μW. Cela représente une efficacité énergétique de 1,5 pJ/bit, soit 8 fois plus petite que celle du meilleur démodulateur compétitif à la pointe de la technologie.

En outre, un schéma basé sur la modulation CWM codant deux bits par symbole, appelé CWM à quatre niveaux (Quad-level CWM - QCWM), est également proposé. Il permet un rapport débit/fréquence plus élevé de 2/5; correspondant à 10,84 Mb/s à une fréquence de la porteuse de 27,12 MHz; tout en consommant seulement 35,5 μW.

ABSTRACT

Implantable Medical Devices (IMDs) are electronic implants notably used to restore or enhance lost organ functions. They may treat complications that cannot be cured with medication or through surgery. Offering unprecedented healing properties and enhancements, IMDs are increasingly requested by physicians and patients. In 2017, the worldwide IMD market was valued at USD 15,21 Billion. By 2025, it is expected to attain USD 30.42 Billion sustained by a compound annual growth rate of 9.24% according to a recent report published by Fior Markets. This expansion is bringing-up more demand for higher performance, additional features, and longer device lifespan and autonomy. These requirements can only be achieved with advanced power sources, high-data rates, and robust miniaturized electronics. Building systems able to provide all these characteristics is the main goal of many researchers.

Among several wireless technologies, the inductive link, which consists of a magnetically-coupled pair of coils, is the most widely used wireless technique for both power and data transfer. This is due to its simplicity, safety, and ability to provide simultaneously both power and bidirectional data transfer to the implant.

However there are still a number of challenges regarding the implementation of such Wireless Power and Data Transfer (WPDT) systems. One main challenge is that the requirements for high Power Transfer Efficiency (PTE) and for high-data rate communication are contradictory. In fact, the bandwidth needs to be widened for high data rates, but narrowed for efficient power delivery. Another big challenge is to implement a high-speed demodulator with simple implementation and ultra-low power consumption.

In this project, we propose and experiment a new WPDT system dedicated to IMDs allowing high-speed communication and efficient power delivery, while maintaining a low power consumption, small silicon area, and simple implementation of the receiver. The proposed system is based on a new Carrier Width Modulation (CWM) scheme, as well as novel modulation and demodulation circuits. The modulation consists of a synchronized opening of the primary LC tank for one or two cycles according to the transmitted data. Unlike conventional modulation techniques, the data rate of the proposed CWM modulation is not limited by the quality factors of the primary and secondary coils. On the other hand, the proposed CWM demodulator allows higher-speed demodulation and simple implementation, unlike conventional demodulators for a similar modulation scheme. It also offers a wide range of data rates under any selected frequency from 10 to 31 MHz. The functionality of the proposed WPDT system is proven using a hybrid implementation of custom-integrated demodulator

circuits and board-level discrete components. It allows a maximum data rate of 3.33 Mb/s for a maximum power delivery of 6.1 mW at 1 cm axial distance between the coils. Due to its generic behavior, the system can also transfer more than 55 mW at 100 kb/s. An operator can select the best compromise between power transfer and data rates in accordance to application or current needs, without reconfiguring the receiver.

The latter includes a COTS power recovery stage and an ultra-low power CWM demodulator IC fabricated with 130 nm CMOS technology. It has a very small silicon area of 2100 μm^2, consumes 16.9 μW in worst condition, and reaches data rates of 1/3 of the carrier frequency. At 27.12 MHz carrier frequency, a data rate of 9.04 Mb/s is achieved at a cost of only 13.68 μW power consumption. This represents an energy efficiency of 1.5 pJ/bit, that is 8 times smaller than the best state-of-the-art competitive demodulator.

In addition, a CWM-based scheme encoding two-bit-per-symbol, called Quad-level CWM (QCWM), is also proposed. it allows higher data-rates-to-frequency ratios of 2/5; corresponding to 10.84 Mb/s at 27.12 MHz carrier frequency; while consuming only 35.5 μW.

TABLE OF CONTENTS

LIST OF TABLES

LIST OF FIGURES

LIST OF SYMBOLS AND ACRONYMS

AC	Alternating Current
ADC	Analogue-to-Digital Conversion
ASK	Amplitude Shift Keying
AWGN	Additive White Gaussian Noise
BER	Bit Error Rate
BMIs	Brain-Machine Interfaces
BW	Bandwidth
CMOS	Complementary Metal Oxide Semiconductor
COOK	Cyclic ON-OFF Keying
COTS	Commercial Off-The-Shelf
CT	Current Transformer
CWM	Carrier Width Modulation
DC	Direct Current
DFSK	Differential FSK
E/b	Energy Efficiency
ED	Envelope Detector
EDLC	Electric Double-Layer Capacitor
EM	Electromagnetic
EMI	Electromagnetic Interference
EPC	Efficient Power Conversion Corporation
Exclusiv Negative OR	XNOR
FOM	Figure Of Merit
FSK	Frequency Shift Keying
GaN	Gallium nitride
IBM	International Business Machines
IC	Integrated circuits
ICD	Implantable Cardioverter Defibrillator
ICNIRP	International Commission on Non-Ionizing Radiation Protection
IMD	Implantable Medical Device
IPT	Inductive Power Transfer
ISM	Industrial Scientific and Medical
Li/CFx	Lithium/Carbon monofluoride
Li–MnO2	Lithium/Manganese Dioxide

Li/SVO	Lithium/silver vanadium oxide
LDO	Low-Dropout
LSK	Load Shift Keying
LVAD	Left Ventricular Assist Device
Med-Tech	Medical Technology
MIM	Metal-insulator-metal
MRI	Magnetic Resonance Imaging
MUX	Multiplexer
NMOS	Negative-channel metal oxide semiconductor
NOR	Negative OR
OOK	On-Off Keying
PA	Power Amplifier
PCB	Print circuit board
PHM	Pulse Harmonic Modulation
PMA	Power Matters Alliance
PMOS	Positive-channel metal oxide semiconductor
PPM	Pulse Position modulation
PPSK	Passive Phase-Shift Keying
PSK	Phase Shift Keying
PTE	Power Transfer Efficiency
PVP	Lithium/iodine-Polyvinylpyridine
PWM	Pulse width modulation
PW-to-SP	Pulse Width to Sawtooth Peak
Q	Quality
QCPSK	Quasi-Coherent PSK
QCWM	Quad-level Carrier Width Modulation
QPSK	Quadrature phase shift keying
RF	Radio Frequency
RFID	Radio Frequency Identification
RX	Receiver
SAR	Specific absorption rate
SNR	Signal to Noise Ratio
TX	Transmitter
WPDT	Wireless Power and Data Transfer
WPT	Wireless Power Transfer
XNOR	Exclusiv Negative OR

LIST OF APPENDICES

CHAPTER 1 INTRODUCTION

1.1 Motivation

IMDs are embedded systems placed inside the body for monitoring, diagnostic and/or therapeutic purposes. To operate these devices, a continuous energy supply is required. The required power level depends on the application. It can be low (e.g. 0.1 mW for pacemakers), medium (e.g. 100 mW for neuro-stimulators and drug pumps), or high (e.g. >100 mW for retinal prosthesis and endoscopic capsules) [16, 17].

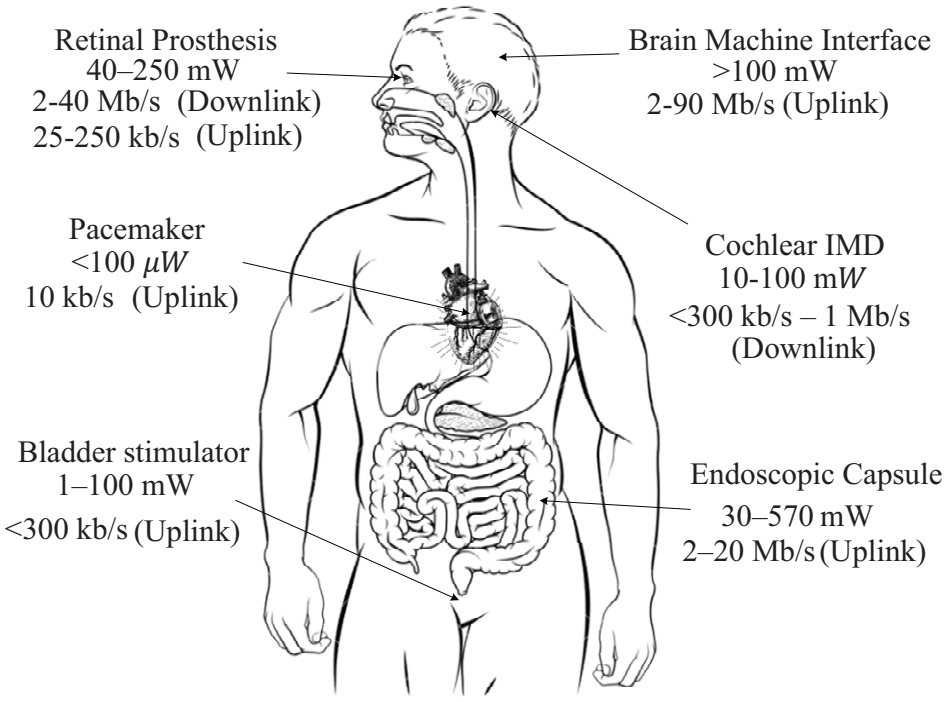

Figure 1.1 Typical power and data rate requirements of main IMDs [1–13].

Bidirectional exchange of information is usually requested for IMDs. In most cases, an external base station sends data (downlink) to control the implant or stimulate the biological tissues. In the other direction, IMDs send-back data (uplink) for two main purposes: (1) to monitor parameters variations (e.g. power and voltage levels, electrode impedance, temperature, and humidity [18]) to the external device for calibration or safety purposes; (2) to send recorded physiological activities to an external processor for data analysis, or for closed-loop stimulation control. When many bio-signals need to be monitored in real-time and continuously transmitted, high-data rates are mandatory. For example, Brain-Machine Interfaces

(BMIs) employ hundreds of electrodes. This may require data rates of up to 90 Mb/s [19]. Figure 1.1 presents an estimate of power and data rate requirements for several commercially available types of IMDs.

With their growing use, IMDs are becoming more complex, thus requiring increasingly sophisticated wireless powering and communication systems and techniques. Many approaches have been investigated to tackle the evolving requirements of IMDs in terms of power supply or/and communication systems.

Power supply methods can be categorized into two main groups: (1) in-vivo power sources that operate independently from any external device, and (2) ex-vivo power sources that use external power units to transfer energy transcutaneously to the IMD.

In-vivo power sources are solutions used to power up IMDs. Typical sources include batteries, supercapacitors [20–25], or human-based energy harvesting sources that convert energy of the human body like chemical energy [26–30], motion and temperature gradients into electricity [31,32]. Many efforts were made to meet all the IMDs' requirements using alternative in-vivo power sources. However batteries are still the most suitable and the most popular power source used for IMDs [16, 33].

Battery cells produce electrical energy by direct transformation of chemical energy and can be classified into two main types: (1) primary or single-use batteries and (2) secondary or rechargeable batteries [34–36]. Unlike the primary batteries, the secondary batteries are a power source that can be "refilled" when depleted.

Most commercial IMDs today are powered by lithium-ion based batteries which offer high energy density along with compactness, safety, reliability, and durability for many applications [37]. Therefore, some commercial IMDs, such as Medtronic neurostimulators (ex. the ACTIVA RC Neurostimulator for deep brain stimulation) were equipped with lithium-ion rechargeable cells [38]. Currently, lithium-ion rechargeable batteries are also used in several IMDs under development, such as neurostimulators to cure epilepsy and Parkinson's diseases, cochlear implants, Left Ventricular Assist Devices (LVADs), and artificial hearts. Manufacturing high quality lithium-ion batteries is a well-mastered process. However, elaborated tests are required to ensure their safety. Actually, secondary batteries should be well sealed and monitored all the time to prevent overheating and damage. Manufacturers usually implement cut-off safety features to ensure a safe use of the devices [39–41]. Also, minimizing the size and weight of the batteries while providing maximal autonomy are still among the main design challenges of IMD battery sources. More information about batteries meant for IMDs is presented in Annexe A.

On the other hand, several ex-vivo power sources or wireless power transfer solutions have been investigated in the literature. These solutions are based on external source units and they may support both power and data transfers. The best known wireless transfer techniques use RF [42, 43], optical [44, 45], ultrasonic [46–48], capacitive [49], and inductive links [14, 50]. However, due to its simplicity, reliability, and safety, the inductive link is the most widely adopted technique in commercially available IMDs [51] for both wireless powering and bidirectional data transmission. The operation principle of the other listed techniques, their main advantages and drawbacks are summarized in Table 1.1, whereas each of these methods may be the subject of further research.

1.1.1 Power Supply and Data Communication via inductive link for IMDs

The idea of inductive wireless power transfer came to Nikola Tesla in the early twentieth century [56]. Tesla was able to demonstrate wireless powering by inductively lighting light bulbs [57]. Later, Tesla's concept inspired many generations of researchers. However, it is only during the last decades that a major interest in inductive powering started. This is due to the proliferation of portable devices such as mobile phones and laptops. Many research laboratories and industrial companies (including Med-Tech) have shown interest in WPT using inductive coupling [58]. Currently, the field is developing rapidly, especially after the emergence of three WPT standards (Qi, PMA and Rezence) targeting the spreading of wirelessly chargeable products (such as smartphones, home appliances, electric cars and drones) [59, 60].

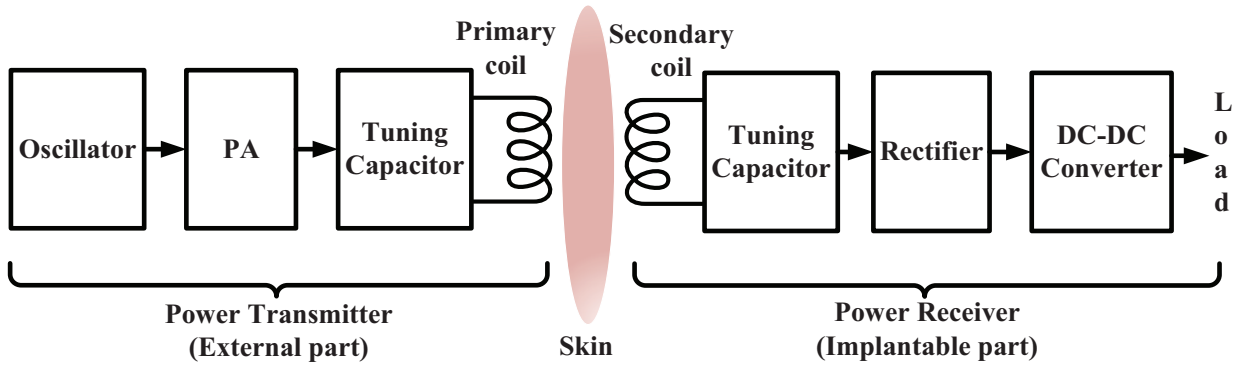

Figure 1.2 Typical model of an IPT system for IMDs

The principle of a traditional Inductive Power Transfer (IPT) system is implemented by using two coils positioned in proximity to each other (Fig. 1.2). When an AC current flows through

Table 1.1 Summary of the major advantages and drawbacks of some wireless power and data transfer approaches

Wireless power/data transfer techniques	**Link principle**	**Advantages**	**Drawbacks**
RF link	Far-field antennas are used at each end of a link. An AC current flowing through a transmitter antenna generates electromagnetic fields that propagate through air and human body. It is then captured by the receiver antenna.	Long-range and high-speed data communication.	High power consumption. High interference problems. High absorption of the electromagnetic (EM) radiation by the body tissue and eventual health hazards at sufficiently high power density.
Optical link	Light emitting and photosensitive devices are used in the transmitter and the receiver respectively.	High level of immunity against electromagnetic interference (EMI). Extremely high-data rates.	High absorption of the electromagnetic (EM) radiation by the body tissue and eventual health hazards at sufficiently high power density.
Ultrasound link	An ultrasound transducer is used to convert electrical signals into ultrasound waves. A piezoelectric receiver is implanted in the human body to convert the ultrasound mechanical energy into electrical charges.	Ultrasound may penetrate deep into the body.	High reflection in the air-tissue interface. The need for a matching layer (such as a coupling gel) between the transducer and the skin.
Capacitive link	Two aligned parallel plates are placed one on the inner side of the skin and the other on the external side of the body. The skin acts as a lossy dielectric due to its conductive properties. An AC voltage applied to the transmitter electrode plate (since a DC current will be blocked by a capacitor) generates an electric field through the skin.	High immunity level against electromagnetic interference (EMI) since the field lines are well confined between the two plates. Data rate is not limited by the channel capacity and signals with a wide range of harmonics, like square waves, can be transmitted easily [52–54].	Relatively low power delivery capacity (tens to few hundred microwatts). Capacitor size $\sim$ at least ten times the desired range [55].

the primary coil, an AC magnetic flux is created in its vicinity. Part of this flux is picked-up by the secondary coil and converted to an AC voltage across it. The power transmitter driving the primary coil is mainly composed of an oscillator and a power amplifier that generates an AC current with a specific frequency and amplitude. A tuning capacitor is placed upstream of the primary coil and another tuning capacitor is located downstream of the secondary coil. These capacitors and coils form LC resonant circuits to ensure maximum transfer power efficiency [50]. At the receiver, the harvested AC power is DC regulated using a rectifier and a DC-DC converter to supply the load and/or recharge a battery [61].

The IPT system is a promising approach for powering cutting edge biomedical devices. It is easy to implement and allows efficient and safe wireless power transfer. There is no risk of tissue heating if exposure limits (for the magnetic field strength) are respected. Its transmitter and receiver coils are in proximity, so the link is less sensitive to interference and external noise. In addition to supplying power, IPT systems also offer the capability of data communication. This IPT technique is therefore frequently used to power various commercially available IMDs.

For commercial IMDs, IPT generally serves two purposes: (1) to recharge the internal battery as in the STIMuSTEP Drop Foot Stimulator system (Finetech Medical Ltd., Welwyn Garden City, UK). [62], the Eon spinal cord stimulator (St. Jude Medical Inc., Saint Paul, Minnesota) [63], and the Aura6000 Targeted Hypoglossal Neurostimulation System (ImThera Medical, Inc., San Diego, California) for the treatment of obstructive sleep [64]. (2) or to directly provide power to the IMD, as is the case for the MAESTRO cochlear implant system and the ARGUS II retinal prosthesis system, developed by MED-EL and Second Sight Medical companies, respectively [65–67]. Figure 1.3 shows two of these commercial products. The MED-EL cochlear implant picks up between 20 mW and 40 mW from an external unit. This power is used to stimulate auditory nerve fibers through several electrodes in contact with the cochlea, as shown in Fig. 1.3a [58]. For best coil alignment, permanent magnets are used in the center of each coil (TX coil and RX coil). On the other hand, ARGUS II retinal implant is powered by 45 mW used to stimulate the retinal neurons according to processed video images captured by a camera [58]. The camera and the external coil are attached to glasses, as shown in Fig. 1.3b. Moreover, a RX coil is strapped around the eye to ensure a better alignment with the TX coil. In addition to supplying power, external units of both the implant systems send data and stimulation commands to implantable units through the same inductive link.

However, despite its widespread use and its benefits, the inductive link has some limitations. The most challenging issue is its high sensitivity to link misalignments and load variations

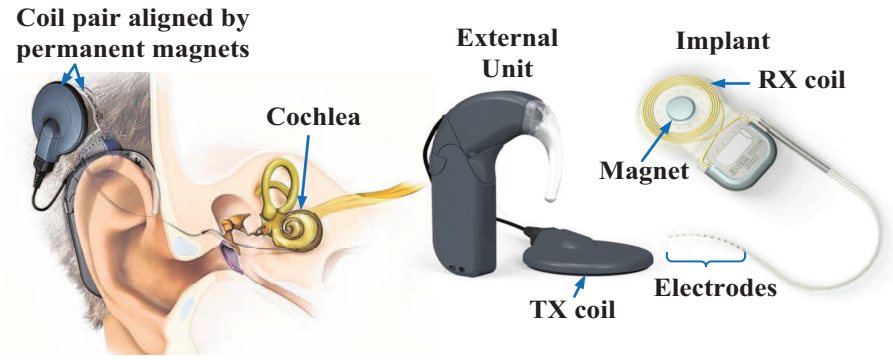

(a)

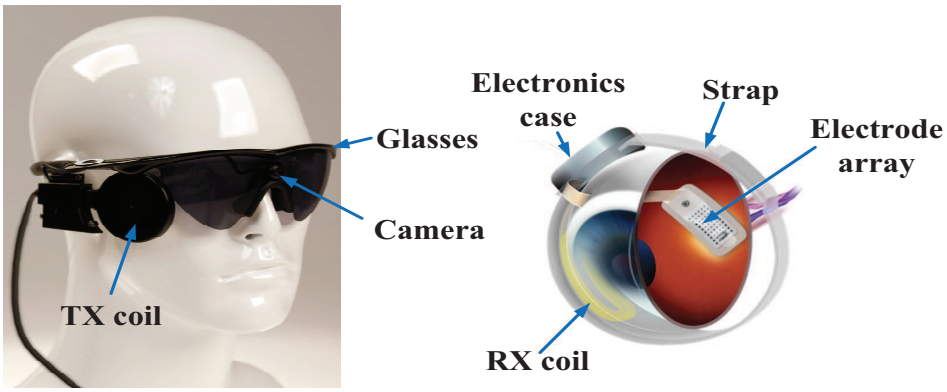

(b)

Figure 1.3 Commercially available IMDs using IPT (a) MAESTRO cochlear Implant system and, (Adapted with permission from MED-EL) (b) ARGUS II retinal prosthesis system (Adapted with permission from Second Sight)

that highly affect the transfer power efficiency. This issue remains among the most popular research topics in IMDs. Different approaches have been proposed. Some works proposed closed-loop systems for reducing the sensitivity to misalignment and coupling factor variations. These studies are reviewed and discussed in [68,69]. The reviewed works aim to ensure high efficiency of the power transmitter, high efficiency of the power receiver, high efficiency power transfer, and minimizing load voltage variations.

Likewise, other research works in the IPT field aim to find the optimal geometry and structure; using numerical simulation optimization approaches; to reduce losses, size, interference, and sensitivity to coupling variations and to enhance the power transfer efficiency and the power delivered to the load [70–73]. Other challenges emerge when the inductive link is also exploited for data transmission. In that case, ensuring high power transfer efficiency and high-data rate at the same time is very challenging, when a simple and low power consump-

tion solution is required. This challenging fulfillment will be the subject of this thesis.

1.2 Challenges

Ensuring simultaneous wireless inductive transfer of power and data is a challenging process. In fact, it is difficult to ensure high-data rates, continuous power transfer, low power consumption, high robustness against noise, and simplicity of implementation at the same time.

This is due to two main challenges. Firstly, an efficient power transfer and a high data rates communication are conflicting goals. In fact, the bandwidth needs to be widened for high data rates, but narrowed for efficient power delivery. The second challenge is that a high-speed demodulator often consumes a lot of energy and occupies a large silicon area.

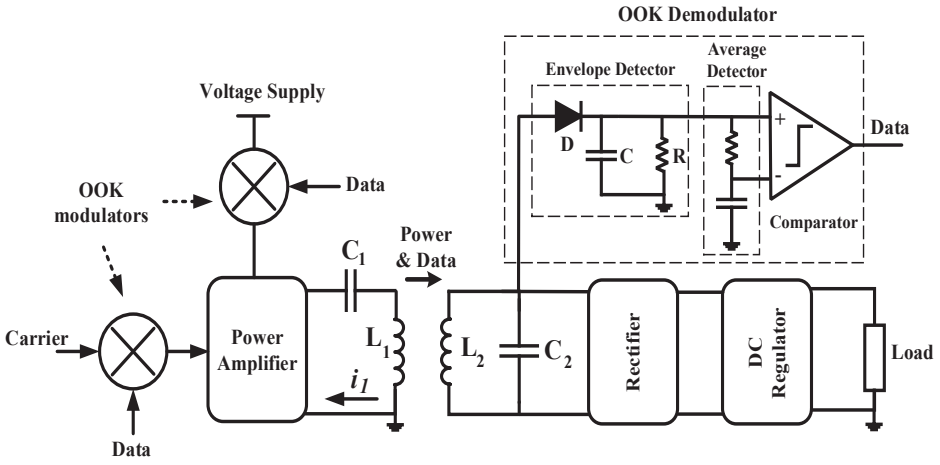

Figure 1.4 Typical block diagram of data and power transmission via an inductive link using OOK modulation

Considered as the simplest and the least power-hungry modulation technique, special attention is given to the OOK modulation (which is an amplitude modulation with 100% modulation index) and a detailed analysis of its limitations will be discussed here to explicitly introduce our proposed solution.

Figure 1.4 shows a typical block diagram of an inductive power and data transfer system using OOK modulation. At the external part, the data can be simply modulated by mixing the data bitstream with the carrier signal [74] or the DC supply voltage [75]. The resulting signal drives a class E power amplifier (PA) in order to amplify the current i_1 crossing the external coil L_1. This generates a magnetic field in L_1 surroundings. At the internal side, the magnetic energy is recovered by the secondary coil (L_2), then rectified and regulated to

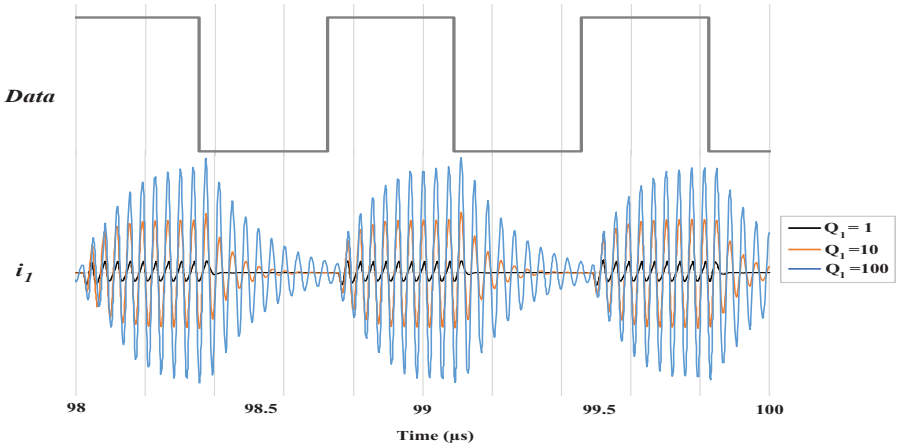

Figure 1.5 The modulated OOK signal i_1 with Q_1 variation

convert the AC power to a regulated DC voltage to supply the IMD. A typical configuration of an OOK demodulator consists of a voltage mode envelope detector, an average detector to produce the average voltage of the extracted envelope, and a voltage comparator to compare the envelope with its average and recover the baseband data.

Despite its low design complexity and reduced power consumption, the data rate of OOK modulation is generally low for two main reasons:

1) **The Q factor issue**: The maximal achievable data rate is limited by the quality factors of the transmitter and receiver coils due to the inverse relationship between the Q factors and the bandwidth BW; as given by (1.1).

$$BW = \frac{f_c}{Q} \tag{1.1}$$

with f_c is the carrier frequency.

In fact, high Q factors increase the transient time, and thus limit the data rate [76]. To better understand the quality factor impact on the data rate, a time-domain simulation of the primary coil current i_1, using OOK modulation at a data rate equivalent to $f_c/10$, is performed for different quality factors of the primary coil Q_1, as shown in Fig. 1.5. Obviously, the amplitude of i_1 and consequently the generated magnetic field strength increase at high Q factor. However, a tank circuit; or LC circuit exchanges voltage and current between the capacitor and the inductor just like a pendulum exchanges kinetic and potential energies. In an ideal tank circuit with no energy dissipation (infinite value of the quality factor), the free-running oscillation of the LC circuit would continue

indefinitely, just as a frictionless pendulum would continue to oscillate indefinitely at its resonant frequency. Therefore, i_1 oscillations at high Q factors would take a long time to die away after On-Off transition of the data signal, as shown in Fig. 1.5. This figure clearly shows that a resonating tank with higher Q factor, which contributes to high PTE, responds more slowly to signal variations and reduces the maximal data rate.

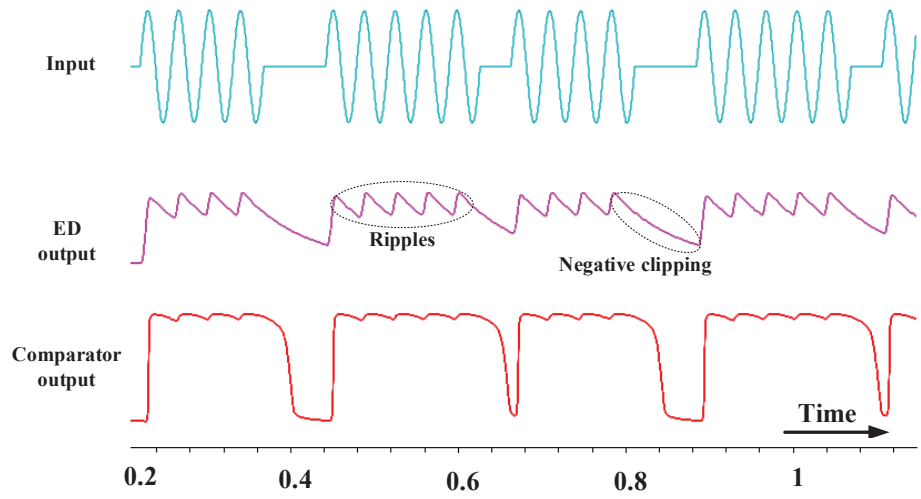

Figure 1.6 Simulated voltage waveforms (using Cadence) of OOK demodulator

2) **The limited speed of the demodulator circuit:** This is mainly due to the envelope detector (ED), which represents the weakest-link of the chain in Amplitude Shift Keying (ASK) demodulators. Typically, the ED is composed of a diode followed by a capacitor C in parallel with a resistor R, as shown in Fig. 1.4. The time constant $\tau = RC$ determines the discharging time of the capacitor. For a faithful extraction of the modulated signal envelope, the time constant should satisfy the following inequality [77].

$$\frac{1}{f_c} \ll \tau \ll T_{min_{data}} \tag{1.2}$$

where $T_{min_{data}}$ is the shortest time interval between two binary words. This condition cannot be fulfilled for high data rate applications. [78].

Figure 1.6 shows the simulated waveforms in an OOK demodulation stages when an ideal OOK signal with short $T_{min_{data}}$ (equal to one or two cycles) is used as input. Even with an optimal time constant τ, the envelope detector (ED) output voltage has high ripples and negative peak clipping. Under practical situations, this signal will be

degraded to some extent due to the presence of noise and amplitude disturbances [79]. It has also been shown that the ED can consume significant power due to high dissipated power in the diode during the conduction phase.

1.3 Research Goals and Contributions

This work aims to tackle the Q factor issue and the limited speed of the demodulator circuit. The main objective of this project is to propose and experiment a complete wireless power and downlink data transfer system dedicated to IMDs. This WPDT system should ensure a high data rate without compromising the Wireless Power Transfer (WPT) efficiency while maintaining a low power consumption and a small and simple implementation of the implantable device. Another objective is to propose a generic WPDT that operates under a wide range of data rates. So, the operator can select the best compromise Power-Data rates depending on the application or need, without reconfiguring the receiver.

Several key research contributions, which address these goals, are highlighted below:

1) **New modulation schemes (CWM and Quad-level Carrier Width Modulation (QCWM)) published in [15, 80–82] and in Chapter 3 and 4:**

   A novel approach for downlink data transmission based on a carrier-width modulation CWM is proposed. As the name indicates, the modulated parameter is the width of the carrier or the number of carrier cycles.

   This modulation technique allows simultaneous transfer of power and data over a single inductive link without the data rate being limited by the quality factor of the primary LC tank. Contrary to conventional modulation techniques, our modulation is performed at a specific time and location. It consists of a data-driven synchronized opening of the primary LC tank (location) for one or two cycles at the current zero-crossing instant (time). Using this approach, a data rate up to 1/3 of the carrier frequency can be achieved. Also, since the carrier is time modulated, the modulated signal has a high robustness against any amplitude disturbances.

   A CWM-based scheme encoding two-bit-per-symbol, called Quad-level CWM (QCWM) is also proposed. It consists of sending two bits per symbol by using four combinations of duty ratio. QCWM allows high data-rates-to-frequency ratios. It offers a data rate of 2/5 the carrier frequency.

2) **High speed and ultra-low power demodulators ICs, published in [15, 80–82] and in Chapter 3 and 4:**

Using a 0.13-μm CMOS process and 1.2 V power supply, both CWM and QCWM demodulators were implemented and fabricated. They respectively dissipate, in worst conditions, 16.9 and 35.5 μW. Compared with state-of-the-art demodulators used for inductive forward data transmission, the proposed demodulators are distinctive given their low-energy efficiency, due to their ultra-low power consumption, despite the high data rates of the transmission. They also occupy a very small silicon areas of 2137 and 3256 μm^2.

The very competitive expected performance is due to the use of an original pulse width to sawtooth waveform converter. This module is proposed to avoid the conventional envelope detector limitations. It allows a fast transient response to CWM or QCWM modulated signals while achieving an ultra-low power consumption of 4.8 µW and occupying a small silicon area of 486 μm^2.

3) **Generic CWM demodulator, published in [81, 82] and in Chapter 4:**

The On/Off duration of the modulated signal and the demodulator design are carefully chosen to reach a generic high-performance powering and data communication system. In fact, the Off durations of the modulated signal are chosen the same for an infinity of CWM modulated schemes while the CWM demodulator is designed to depend only on these Off durations. At the same carrier frequency, an infinite CWM schemes may be effectively demodulated without any reconfiguring of the demodulator. In addition, a wide frequency range between 10 and 31 MHz may be covered by this demodulator only by re-selecting two voltage references.

Due to the demodulator genericity, an operator can select the best data rates depending on his application or need, without the need to redesign the receiver. Also, it offers the possibility of varying the data bit rate in the same application but at different instants, if the application requirements are variable over time.

4) **High-Q transmitter allowing high data rate data transmission described in [83] and in Chapter 5 :**

A novel high-Q power and data transmitter is designed and implemented. It generates high speed modulated signals despite the use of high-Q coils. This kind of transmitter has previously proposed 23 years ago in a patent. However, few information has been reported concerning the whole system, the design analysis, and the used-carrier frequency. In the present project, a complete system with all technical details and faced

challenges are presented and discussed.

The proposed transmitter is also conceived to be generic that operates under a wide range of data rates at 10 MHz carrier frequency. It allows, in combination with the receiver, a maximum data rate of 3.33 Mb/s for a maximum power delivery of 6.1 mW at 1 cm coil separation distance. The system may reach more than 55 mW at 100 kb/s.

1.4 Thesis Organization

This thesis is organized as follows:

Chapter 2 describes and compares state-of-the-art inductive coupling methods used for simultaneous remote powering and data communication in IMDs, with particular focus on solutions exploiting a single inductive link.

Chapter 3 consists of the published paper [15] that addresses the first and the second research contributions of this work. It presents analytical and simulation results of an inductive link implementing the proposed CWM modulation, discusses the main design considerations of the demodulator, and shows experimental validation results.

Chapter 4 consists of the published paper [82]. It also addresses the first two contributions in addition to the third contribution. It presents the generic CWM demodulator able to cover a wide range of carrier frequencies from 10 to 31 MHz; a sensitivity analysis on the main block (PW-to-SP converter) of the proposed demodulators; and the QCWM demodulator circuit design; as well as experimental validation of the generic-CWM and QCWM demodulators.

Chapter 5 consists of the submitted paper [83] that approaches mainly the fourth contribution. It describes a complete system of wireless power and downlink data transfer, based on CWM modulation. It provides implementation details and experimental results of the proposed WPDT system with more emphasis on the transmitter design.

Chapter 7 elaborates a general discussion and conclusion of the entire thesis and presents recommendations to future work.

CHAPTER 2 LITERATURE REVIEW

2.1 Introduction

Due to the constantly growing geriatric population and the projected increase of the prevalence of chronic diseases that are refractory to drugs, Implantable Medical Devices (IMDs) such as neurostimulators, endoscopic capsules, artificial retinal prostheses, and brain-machine interfaces are being developed. According to many business forecast firms, the IMD market is expected to grow and they are subject to much research aiming to overcome the numerous challenges of their development. One of these challenges consists of designing a wireless power and data transmission system that has high power efficiency, high-data rates, low power consumption, and high-robustness against noise. This is in addition to minimal design and implementation complexity.

This chapter is a comprehensive survey of the latest techniques used to power up and communicate between an external base station and an IMD. It is organized into three sections. Section 2.2 describes the multiple wireless links solutions proposed to tackle the Q factor issue previously discussed. Section 2.3 provides a comprehensive survey on main modulation schemes for data communication that can be used to ensure both power and data transfer over a single inductive link. The advantages and drawbacks of these modulation schemes for forward and backward data communication are studied. Section 2.4 presents safety considerations related to transcutaneous power and data links for IMDs and their biological, physical, electromagnetic and EMI impacts and concerns.

2.2 Multiple links for Simultaneous Remote Powering and Data Communication

Multiple dedicated wireless links are among the possible solutions implemented to simultaneously transfer power and data to IMDs.

There have been different state-of-the-art methods for using multiple wireless links. Each method has its advantages and drawbacks depending on the application [14,84–87]. Figure 2.1 shows two possible scenarios. In Fig. 2.1a, three inductive links are used [14], one link for power delivery and two links for forward and backward communications. In Fig. 2.1b, RF and inductive links are employed: two separate pairs of coils are used for powering and forward communication. An RF link is adopted for backward communication in order to guarantee a higher data rates telemetry and longer distance transmission [87]. However, with this topology, more energy can be dissipated in the implantable part.

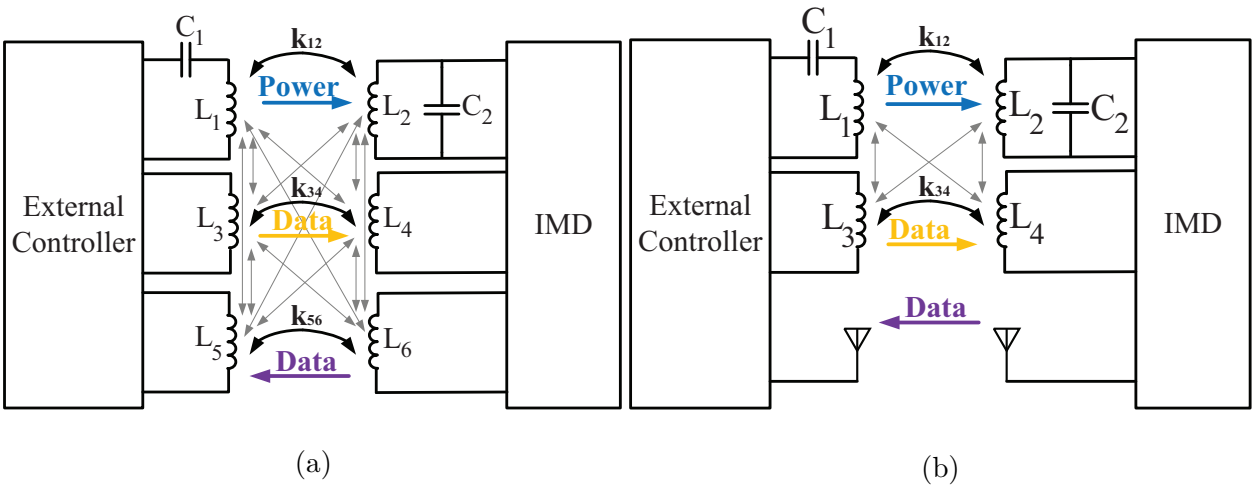

Figure 2.1 topologies used for wireless power delivery and data transmission: (a) Separate inductive links. (b) Hybrid RF/Inductive links

When, using multiple dedicated wireless channels, each link can be optimized separately. The power transfer link is optimized to have the highest Quality (Q) factors for the primary and secondary coils and the lowest power loss, while each data transfer link is optimized to provide the highest bandwidth (high-data rate). Unfortunately, this approach of implementing separate links for power and data communication adds complexity to circuits and coil structures. It also suffers from strong cross talk between the links. As shown in Fig. 2.1a, for a set of 6 coils, there are 15 distinct coupling factors. Only three of them (black arrows) allow the transfer of power and data. The others (gray arrows) induce disturbances in the power and data carriers due to the waves interference. Obviously, data carriers are most concerned about the interferences.

To reduce these interferences, several geometrical approaches (coil arrangement) have been proposed. Among others, the coplanar approach [14] and the orthogonal approach [88] are shown in Fig. 2.2. These approaches show that minimal interference and coils cross-coupling can be obtained. However, the coplanar structure is sensitive to misalignment and the interference minimization improvements ensured by the orthogonal structure are made at the detriment of the coupling factors ensuring power and data transfer.

Another solution to solve the interference issue and achieve higher data rates is based on an appropriate modulation approach proposed to replace the carrier signal with a series of sharp and narrow pulses. This method is called Pulse Harmonic Modulation (PHM) [89]. To transmit bit “1” two narrow pulses with specific time delays and amplitude are generated by the PHM transmitter. The first pulse is used to initiate oscillations on the PHM receiver. The second pulse is sent with lower amplitude, which generates 180° out of phase oscillations

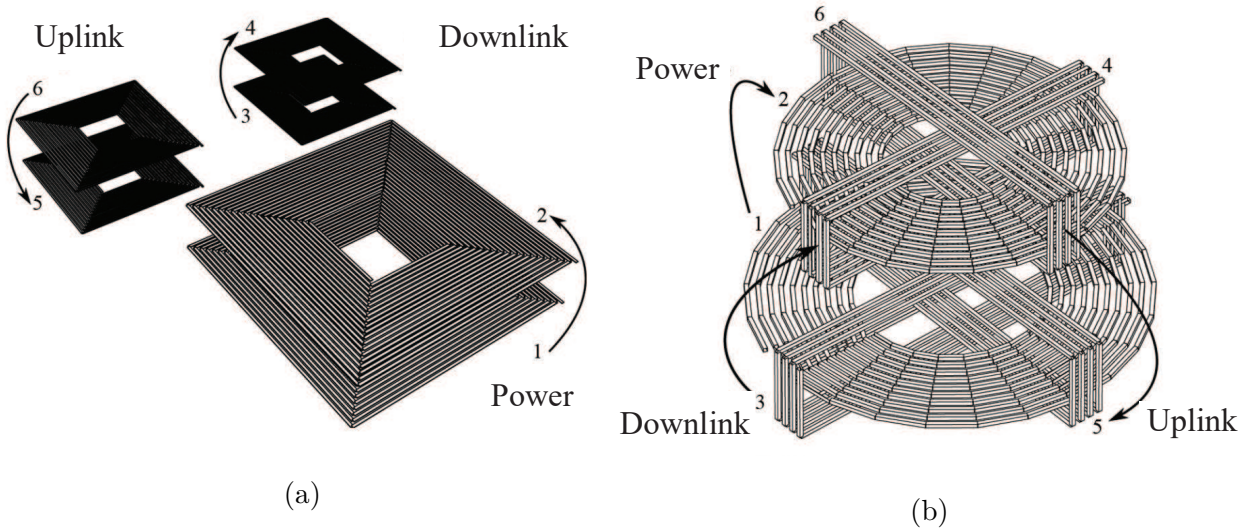

Figure 2.2 Multicarrier wireless link with (a) Coplanar coil geometry, and (b) Orthogonal coil geometry [14].

to suppress the oscillation of the first pulse. For bit "0", no pulses are transmitted. The maximal data rate achieved by this method is 20 Mb/s under a carrier frequency of 66.7 MHz, at 1 cm coupling distance, and without dissipating much power in the IMD. However, it has been proven that PHM is not robust enough against strong power carrier interferences [90]. Moreover, as it is a carrier less modulation technique, it cannot be used to simultaneously transfer power to IMDs. Its implementation requires a separate set of coils for the power transfer.

As a consequence, to the added complexity and interference problems of using separate links for power and data communication and aiming for smaller and simpler circuits and systems for IMDs, ensuring simultaneous remote powering and data transfer over a single inductive link would have potential benefits even on human safety and health as will be shown in next sections.

2.3 Remote powering and data communication over a single inductive link

A single pair of coils can be used for both data and power transfer simultaneously [91], as shown in Fig. 2.3. Nevertheless, achieving high PTE and high-data rates at the same time over a single inductive link is a challenging task. In fact, for an efficient power transfer, a high Q factor of the inductive coils is needed. However, the high Q factor is reflected by a narrow bandwidth of data transmission limiting the achievable data rate. Therefore, transferring data and power over a single inductive link has conflicting requirements. Such

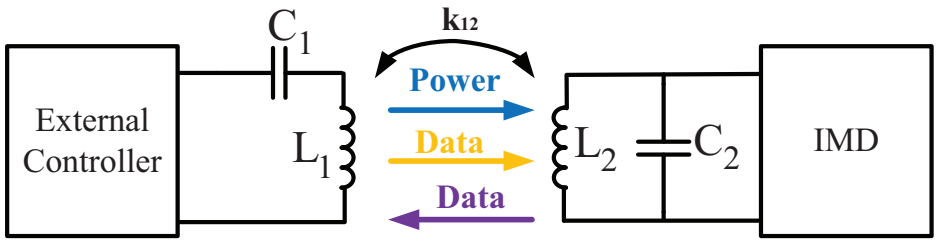

Figure 2.3 Single inductive link to transfer both power and bidirectional data

a challenging problem can be solved using appropriate modulation schemes for the forward and the backward data communication. In this section, a comprehensive survey details possible modulation schemes that can be used to ensure both power and data transfer over a single inductive link. The advantages and drawbacks of different modulation alternatives are exposed.

2.3.1 Remote Powering and Downlink Communication Over a Single Inductive Link

The downlink data transfer is mainly based on the carrier modulation to create detectable variations through the secondary coil. Conventional modulation solutions are first reviewed, and an interesting modulation called Suspended-carrier modulation is then discussed.

Conventional modulation schemes (ASK, PSK, FSK)

Conventional carrier modulation schemes are commonly implemented using Amplitude Shift Keying (ASK), Frequency Shift Keying (FSK), or Phase Shift Keying (PSK), as illustrated in Fig. 2.4. The choice of a modulation scheme depends considerably on the application requirements. For systems requiring continuous power transmission, high-data rates, and high immunity against noise, PSK modulation and its derivatives (such as Quadrature PSK, Differential PSK or quasi-coherent PSK) are often used. However, these techniques suffer from implementation complexity and high power consumption [92]. FSK modulation has the same advantages and limitations as PSK but requires a wider bandwidth (so that both modulated frequencies can pass through the link) [93].

For lower power consumption and design complexity, ASK is generally preferred. Indeed, using ASK, complex synchronization circuitry is needless for data recovery. However, this modulation scheme has its proper limitations. It is weakly immune to disturbances that affect the carrier amplitude, including noise, coupling variations, and interferences.

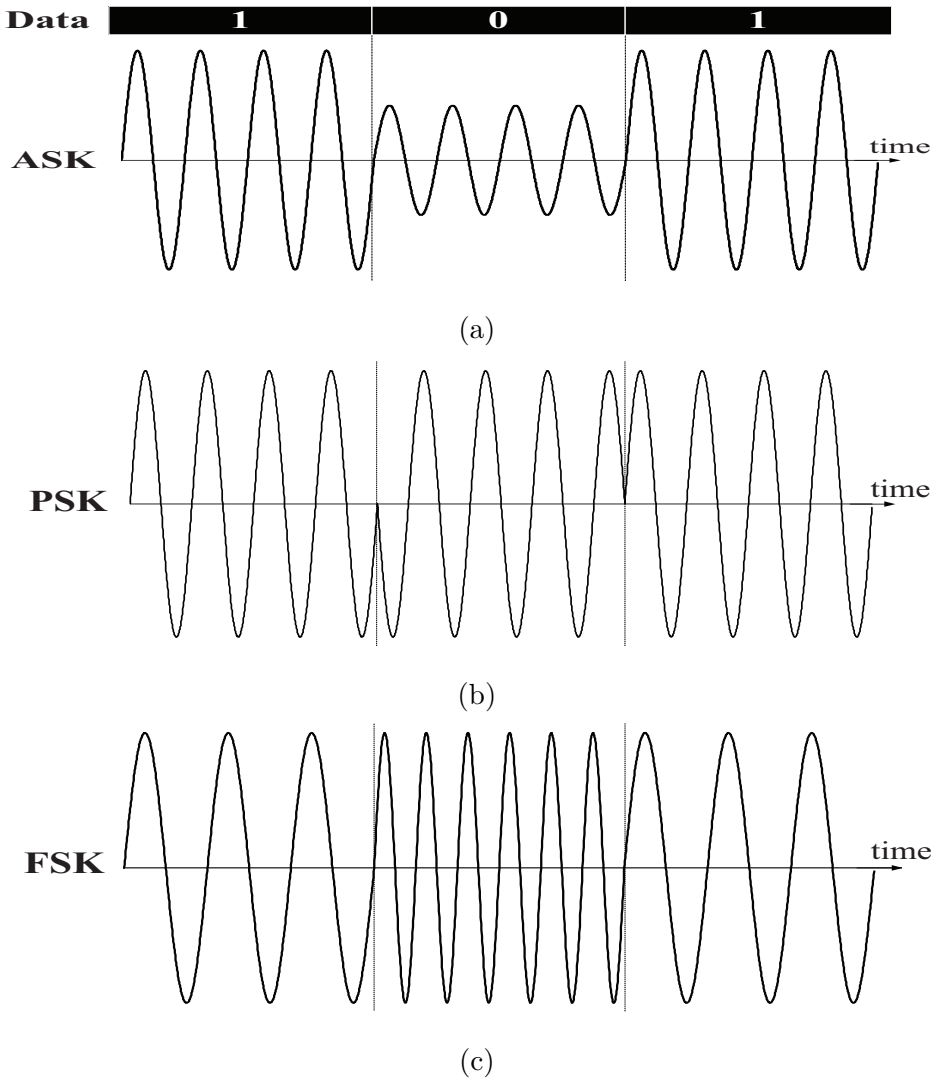

Figure 2.4 Typical modulation schemes: (a) ASK, (b) PSK, and (c) FSK

For better immunity to disturbances, the On-Off Keying (OOK) modulation can be used as part of its signal that has a 100% modulation index, as shown in Fig. 2.5a. However, this method cannot transfer power continuously because of the complete absence of the carrier wave during "0" bit periods. Therefore, some kind of energy storage devices are required to supply power when it is not being transferred [94].

Another alternative is to encode the duration instead of the amplitude as in ASK-PWM (Pulse Width Modulation) and ASK-PPM (Pulse Position Modulation), as shown in Fig. 2.5b and Fig. 2.5c [95]. As the baseband data is encoded by different pulse widths or pulse positions, these methods are more robust against noise and amplitude disturbance than their ASK counterparts. They can also ensure a better power transfer and efficiency if the

suspension and trigger times of the carrier are optimized.

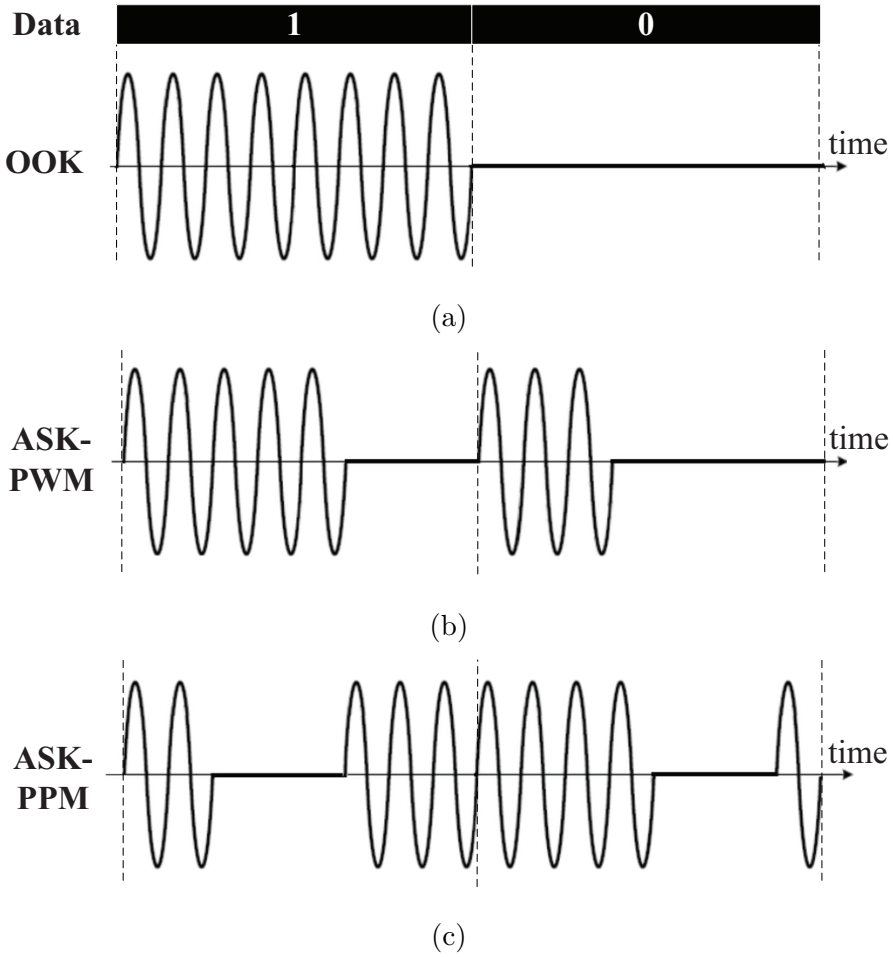

Figure 2.5 Different ASK data encoding schemes (a) On-Off Keying, (b) Pulse width, and (c) Pulse position.

Another limitation of the ASK modulation and its derivatives (ASK-PWM and ASK-PPM), is their inability to achieve high-data rates. Actually, while using such techniques, the bandwidth was shown to be limited to 1/10th of the carrier frequency [96]. There are two main limitation sources of the data rates when ASK and its derivatives modulations are used over the power carrier:

- The Q factor: due to the inverse relationship between the Q factor and the bandwidth BW; as given by (2.1); a high Q factor contributing to high PTE [68] is conflicting with reaching high-data rates. Consequently, the maximum data rate is limited by the bandwidth that

should be as narrow as needed to enhance PTE.

$$BW = \frac{f_c}{Q} \tag{2.1}$$

- The demodulator limitations: for a long time, the conventional and simple approach used to demodulate ASK signals is to employ an envelope detector circuit. However, this circuit is the weakness of ASK demodulators, as revealed in [80]. In short, for an exact envelope detection, the RC time constant of the envelope detector, also called τ, should meet the following condition:

$$\frac{1}{f_c} \ll \tau \ll \frac{1}{f_m} \tag{2.2}$$

where f_m is the highest message bandwidth, in Hz. However, this condition limits the maximal achievable data rate at 1/10th of the carrier frequency [96], which makes the envelope detector unsuitable for high-data-rate communication.

A solution targeting the Q factor issue, called the "suspended-carrier" method, was reported by Troyk et al. in [97].

Suspended-carrier modulation

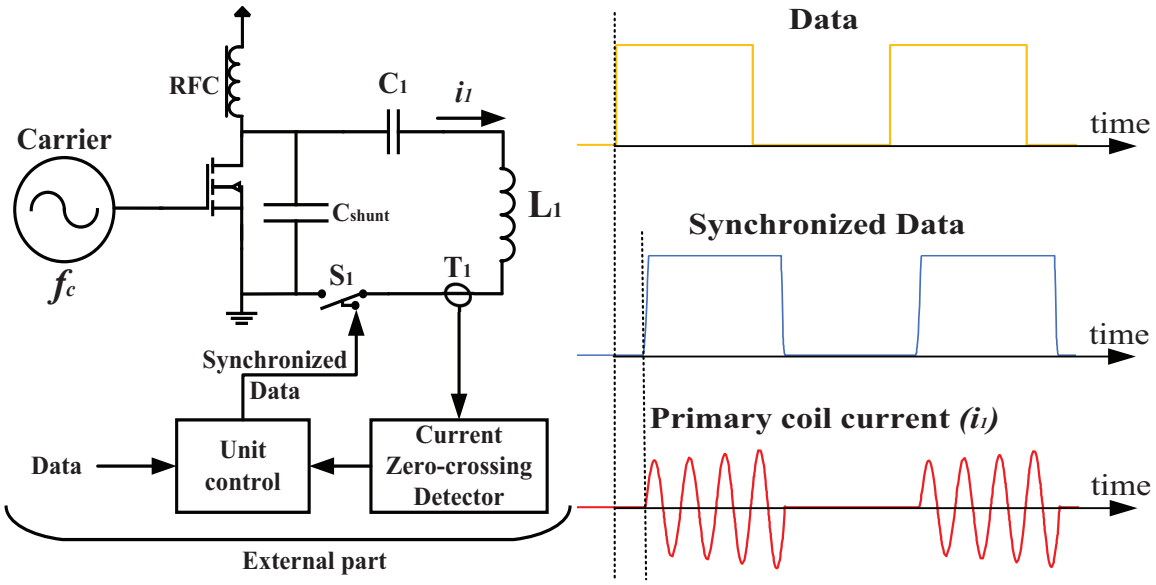

(a) (b)

Figure 2.6 Suspended-carrier modulation: (a) Schematic of the transmitter circuit diagram, and (b) the corresponding circuit operation waveforms

Table 2.1 An experimental comparison of demodulators used for downlink communication over a single inductive link.

Reference	Modulation Scheme	CMOS Technology (µm)	Frequency (MHz)	Data rates (Mb/s)	Power consumption (µW)	Silicon area (μm^2)	Energy efficiency (pJ/b)	Q factor (primary / secondary)
[95]	PPM[2]	0.18	13.56	8.33×10^{-3}	27.8	$\cong19.4\times10^3$	3.34×10^6	High Q
[98]	Suspended-carrier[2]	Discrete	5	1	N/A	N/A	N/A	125 / N/A
[99]	ASK[2]	0.35	6	1	200	2050	200	10 / 15.2
[100]	ASK-PWM[2]	0.5	25	0.3	140	N/A	466.6	30 / 30
[101]	QCPSK[1]	0.18	4	0.8	59	5×10^3	73.75	N/A / N/A

[1] A signal generator is used to generate the modulated signal.
[2] A transmitter and a real inductive link are used to generate the modulated signal.

Suspended-carrier modulation scheme looks similar to OOK modulation scheme, but in reality, they have different system designs and different timing of modulation. OOK can be performed by switching ON and OFF, at any time, the DC supply voltage [90,102] or the AC input signal [103] of the power amplifier. For the suspended-carrier modulation, the switching is synchronized with the zero-crossing of the primary coil current and the modulation circuit consists mainly of a switch placed in series with the LC primary circuit and a current zero-crossing detector using a current-sense toroid T_1, as shown in Fig. 2.6a. Figure 2.6b shows a simulated waveform of the primary coil current using the principle of the suspended-carrier modulation.

Unlike ASK modulations, it is claimed that the suspended-carrier modulation bandwidth does not depend on the Q factor of the secondary resonant circuit [97,98,104]. Only a high-Q factor of the primary resonant circuit is required to ensure a high modulation bandwidth. Therefore, both high PTE and high-modulation bandwidth can be secured at the same time.

Theoretically, this method allows the forward telemetry to reach data rates close to the carrier frequency value. However, due to the low-speed demodulation of the actual demodulator's circuit, the maximal achievable data rate is limited to around one fourth of the carrier frequency, as revealed in [104]. The suspended-carrier modulation also has its limitations in terms of power delivery. Indeed, the power can be delivered to the implant only during the transmission of "1" data bits. This makes the power transfer taking place during almost only

50% of the working time assuming that the transmitted data bits "1" and "0" are equal. This modulation scheme is also very sensitive to amplitude disturbances, such as noise, coupling variations, and interferences.

As the suspended-carrier modulation technique was used in the commercial medical implant BION^{TM} for neuromuscular stimulation [105], few information is available concerning the whole system, the design analysis, and the used carrier frequency.

In Table III, the experimental performance of recently reported demodulators used for downlink communication over a single inductive link supporting power transfer are compared.

2.3.2 Remote Powering and Uplink Communication Over a Single Inductive Link

Two possible types of uplink communication systems, also called back-telemetry systems, are used in biomedical applications: the active and the passive back-telemetry [106].

In active back-telemetry, IMDs generate their own magnetic field to carry information. Therefore, active telemetry systems use their own energy supply, e.g. a battery [96, 107] or energy recovered from a separate coil-based inductive link [1], their own oscillator, and a pair of coils or antenna. They can therefore employ many types of modulation such as ASK, FSK, PSK, and their derivatives. A wider bandwidth and longer range of communication may be achieved using active back-telemetry. Hence, it is easier to ensure communications at high-data rate and to reach IMDs located deeper inside the body. Also, this improves robustness against misalignment and distance variations between the external and the implantable units. However, these systems suffer from high power consumption and require cumbersome circuits.

In the passive back-telemetry, information is transmitted by modulating the existing external magnetic field. The same energy used to transfer power is also used to transfer data from the IMD to the external controller. Therefore, passive wireless systems can make use of a single inductive link to transfer both power and data. As a result, they allow lower power consumption and eventually smaller device size.

As we are particularly interested in the simultaneous data and power transfer over a single inductive link, we focus only on passive back-telemetry systems. More specifically, the Load Shift Keying (LSK), the Passive Phase-Shift Keying (PPSK), and Cyclic ON-OFF Keying (COOK) approaches, which have been discussed next.

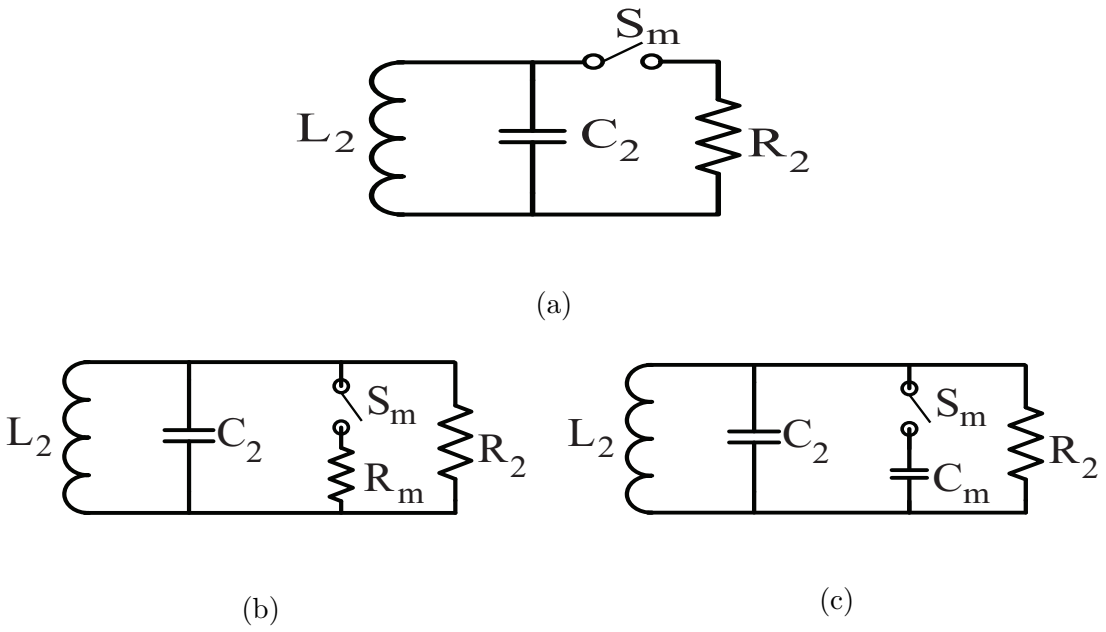

Figure 2.7 LSK modulator principle for (a) series, and (b) parallel resistive load modulation, and (c) capacitive load modulation

Load Shift Keying

The most popular passive telemetry modulation approach is the LSK, also known as impedance modulation, reflectance modulation, or absorption modulation [90, 108]. It is a well-known technique used in Radio Frequency Identification (RFID) tags, wireless sensors, and biomedical applications. LSK is achieved by changing the load impedance in accordance with the digital data.

Any variation in the secondary circuit parameters (as the coil inductance L_2, the capacitance C_2, the total load resistance R_2) or in the coupling coefficient can result in a variation of the equivalent impedance seen from the primary circuit Z_{eq}. Practically, only resistive load and the capacitive load modulations are used to perform LSK modulations. This is because resistances and capacitances are easier to vary than inductances and k values.

The resistive load modulation or load switching can be placed in-series or in-parallel as shown in Fig. 2.7a and Fig. 2.7b, respectively. In the in-series resistive load modulation, the IMD load varies between the resistive load R_2 and the open circuit state (high impedance). R_2 should be small enough to obtain a sufficient distinction between the two states. For parallel resistive load modulation, the load varies between R_2 and the short circuit (low impedance). Consequently, the parallel configuration is more suitable for a large load. Depending on the load nature and value, the best configuration could be serial, parallel, or a combination of

both (if R_2 is variable) [109].

The capacitor load modulation (Fig. 2.7c) results in a detuning of the impedance phase angle of Z_{eq}, and a detuning of the secondary resonant frequency.

$$f_{r2} = \frac{1}{2\pi\sqrt{L_2 C_2}} \tag{2.3}$$

Compared to the resistive load switching, capacitor switching provides larger variations in the reflected impedance with lower power dissipation (due to joule heating). However, secondary LC tank detuning causes an out-of-resonance operation and consequently a low power transfer efficiency. Since only a switch is added to the implantable side, all LSK configurations have the lowest power consumption and circuit complexity compared to other uplink modulator designs.

The major limitation of such modulations is the Q factor issue that was already mentioned in the previous section for forward communication: achieving high-data rates requires low coil quality factors, requirements that are conflicting for high PTE for power transfer.

Furthermore, shifting between the real load and the extra load for LSK leads to impedance mismatching and alters the PTE. In addition, the energy is deviated from the real load to the extra load during data transmission.

Recently, this issue was resolved in [110], [111] by using new uplink modulation schemes: the PPSK and the COOK. Using these recently introduced modulation approaches, simultaneous power and data transmission via a single inductive link can be achieved without the extra load.

Passive Phase-Shift Keying (PPSK)

In the PPSK method, the modulation switch S_m is connected parallelly to the secondary coil L_2 as shown in Fig. 2.8a. The key idea for a proper PPSK operation is that S_m should be switched on to short circuit L_2 at time instant t_0 when the coil voltage V_{L_2} crosses zero. S_m is switched off after only half of a carrier cycle at time instant t_1; when V_{L_2} crosses zero again.

Since at resonance, the coil current i_{L_2} and voltage V_{L_2} are in quadrature, i_{L_2} should be at its positive maximum $I_{L_{2_{max}}}$ at t_0. If no modulation is applied to the link, i_{L_2} should normally evolve to its negative maximum -$I_{L_{2_{max}}}$ at time instant t_1. However, with PPSK modulation, i_{L_2} is forced to be at $I_{L_{2_{max}}}$ instead of -$I_{L_{2_{max}}}$, which contributes toward reversing the phase of V_{L_2} and i_{L_2}. Nevertheless, the secondary LC circuit attempts to counteract against this

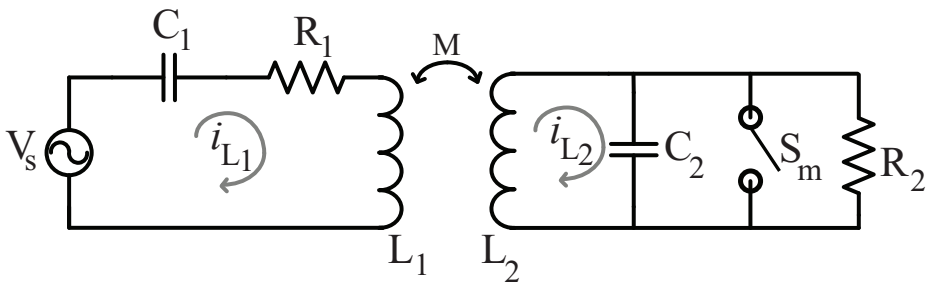

(a) PPSK and COOK circuit model

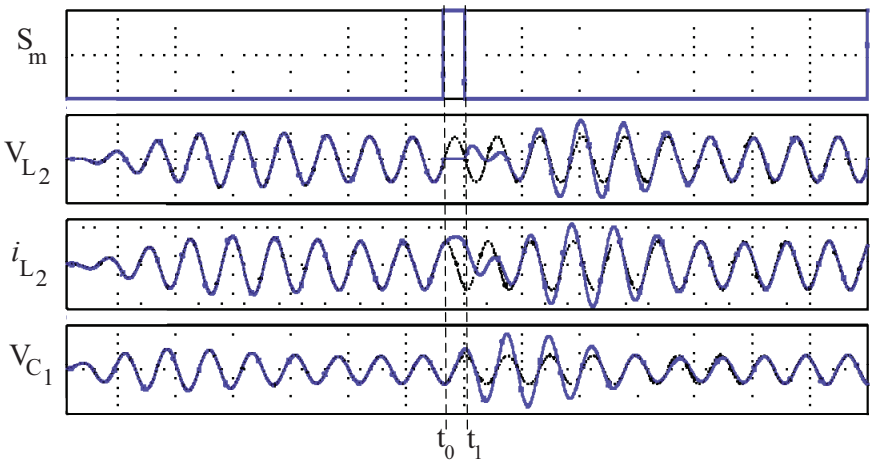

(b) PPSK

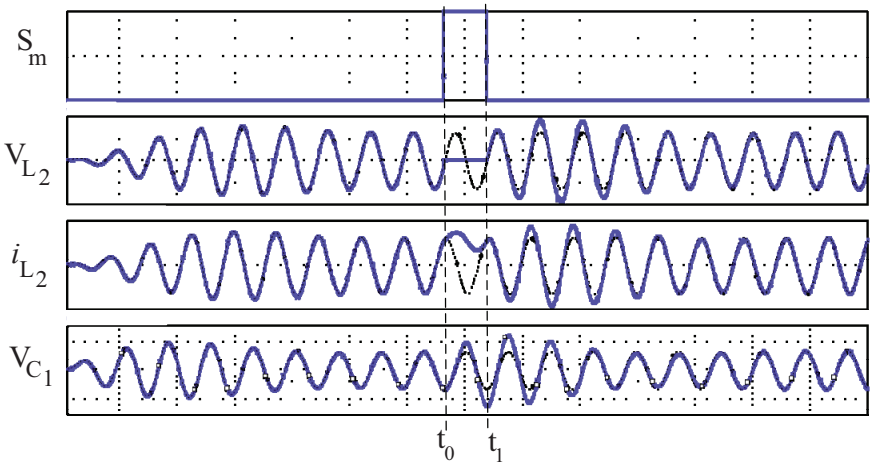

(c) COOK

Figure 2.8 (a) Simplified circuit model of an inductive link with PPSK and COOK modulations, and waveforms throughout the operation of (b) PPSK and (c) COOK modulations

phase variation in order to reach back its steady-state, creating thereby a transient response for a short period of time [110, 112]. This transient response in the secondary coil results in an amplitude variation of the primary current and therefore, a variation of the voltage at the capacitor terminals V_{C_1} is observed as shown in Fig. 2.8b.

In short, the switching of half a carrier cycle (from t_0 to t_1) provokes a passive phase shift modulation in the secondary circuit and results in an amplitude modulation in the primary circuit, which is detected as a logic "1" signal. Whereas, logic "0" is obtained at no switching of S_m. The data rates of PPSK modulation depends on the time interval of the transient response. A high-data rate is reached for a short transient response time and vice versa. Using a carrier frequency of 13.56 MHz, a data rate up to 1.35 Mb/s and a BER below 10^{-5} were achieved for a working distance between 5 and 15 mm. Also, in comparison to a conventional inductive link transferring power without data modulation, PPSK modulation resulted in only 6% lower PTE.

However, the issue related to the trade-off between PTE and data rate still remains due to resonance recovery time after each bit transmission. Obviously, low Q factors of the primary and secondary circuits are unavoidable for over-damped response and short recovery time. This is considered as the main reason that limits the data rate of PPSK modulation to only 1/10 of the carrier frequency. Moreover, due to the phase reversal of LC resonance, power losses and PTE mitigation take place during data transmission.

A PPSK modulator was implemented in [110] using 0.6 μm high-voltage CMOS technology. It mainly contains an RF clock generator and a control logic to synchronize the switching for half the carrier cycle. Concerning the recovery part, it is a typical ASK demodulator implemented using discrete components.

Cyclic ON-OFF Keying (COOK)

The same circuit model of PPSK is adopted for COOK modulation (Fig. 2.8a). However, the only difference is that with respect to the time instant t_1. In COOK modulation, S_m shorts up L_2 for a full cycle instead of half a carrier cycle, as shown in Fig. 2.8c. Unlike PPSK modulation, at t_1, V_{L_2} and i_{L_2} resume their normal course without any phase reversal of LC resonance, which avoids the resonance disturbance and reduces power losses. The single-cycle shorting of the secondary coil results on a voltage rise of the primary capacitor C_1 followed by an exponential falling to the baseline (corresponding to V_{C_1} amplitude without modulation) [111, 116, 117].

It has been proven that unlike LSK and PPSK modulation, a high Q factor of the secondary

Table 2.2 An experimental comparison of modulators used for uplink data communication over a single inductive link.

Reference	Modulation Scheme	CMOS Technology (µm)	Frequency (MHz)	Data rates (Mb/s)	Power consumption (µW)	BER	Maximum P_{DL} (mW)	Energy efficiency (pJ/b)	D_{L_1} (cm) / D_{L_2} (cm) / $d_{L_1L_2}$ (cm)	Q factor (primary / secondary)
[100]	LSK	0.5	25	2.8	100	$<10^{-6}$	N/A	35.71	3.5 / 3.5 / 2	10 / 25
[110]	PPSK	0.6 HV	13.56	1.35	N/A	$<5.9\times10^{-8}$	100	N/A	2.5 / 1.6 / 0.8	120 / 116
[111]	COOK	0.065	13.56	6.78	64	$<9.9\times10^{-8}$	11.5	9.5	6.5 / 4.2 / 1	76 / 75
[113]	LSK	Discrete	1	0.003	N/A	$<1.6\times10^{-6}$	250	N/A	4/ 2.2 / 0.7	High Q
[114]	LSK	0.18	10	2	N/A	N/A	10	N/A	3 / 2 / 0.6	N/A / N/A
[115]	LSK	Discrete	13.56	0.5	N/A	N/A	20	N/A	16.8 / 3 / 4	N/A / N/A

D_{L_1}, D_{L_2} are the diameters of the primary and secondary coils, respectively and $d_{L_1L_2}$ is the intercoil distance.

LC tank decreases the resonance recovery time and allows a high-data rate if the COOK modulation is used. Hence, a high efficiency of the power transfer and a high-data rate can be reached at the same time.

Ha et al. proposed a simple COOK modulation scheme using one-bit encoding per 4 carrier cycles and an enhanced COOK modulation scheme with two-bits encoding per 4 carrier cycles [111]. This is performed by shifting the position of the single-cycle shorting inside the four-cycle time interval. Over a single 13.56 MHz inductive link, a data rate up to 6.78 Mb/s and a BER below 9.9×10^{-8} was achieved at 1 cm distance separation between coils. Furthermore, it allows a maximal PTE of 89.2% at 100 Ω load and 1 cm coil distance separation.

To validate this new method of modulation, a 65 nm CMOS modulator was fabricated and tested. However, no COOK demodulator has been designed and the modulated signal was sampled and decoded using only an oscilloscope and the Matlab software. Basically, an envelope detector should be used to demodulate this kind of signal. However, the limitations of conventional envelope detectors circuits may definitely decrease the maximal achievable data rates.

A list of state-of-the-art modulators used for uplink communication with simultaneous remote powering over a single inductive link is shown in Table 2.2. In order to allow reproducing the setup used to measure the modulators' performance and for fair comparison purposes,

coil dimensions and intercoil distances were included in Table 2.2. Large coils and short intercoil spacing improve the coupling factor and therefore the BER and the maximum Power Delivered to the Load P_{DL}. On the other hand, any misalignment between the external and internal coils may deteriorate these parameters. Closed-loop systems can be employed to reduce the sensitivity to misalignment and coupling variations. However, these approaches may complicate the system architecture and increase its power consumption [68,69]. Mechanical approaches, such as using magnets or straps [65–67], to provide better alignment have fewer disadvantages. Appropriate geometric design approaches using printed spiral coils with multiple layers can improve both efficiency and robustness of the inductive link to coupling factor variations as discussed in [118].

To ensure simultaneous downlink/uplink communication over a single inductive link free from mutual interference, full-duplex and half-duplex communications are the two possible transmission modes [119]. The full-duplex transmission mode can be adopted when each of downlink and uplink modulation techniques vary according to different parameters of the carrier. For example, FSK or PSK that may be used for downlink communication could allow a full-duplex communication with LSK for uplink communication [92,120,121]. However, the latter, which is a kind of ASK, does not allow a full-duplex bidirectional data transmission with ASK modulation and its derivatives. Similarly, only half-duplex communication with time division duplexing can be used to avoid possible interference between downlink and uplink data transmission [110, 119, 122].

2.4 Safety Considerations

Another challenge associated with wireless transcutaneous power and data transfer for IMDs is achieving reliable energy transfer within safety and regulations on biological, physical, electromagnetic (EM) and EM interference (EMI) limits.

Medical device regulations for most safety considerations are rather vague, and constantly changing and improving [123]. They differ from a country to another, fortunately, standardization efforts are actually made to set up international regulatory guidelines and references [124–126]. Discussing these regulations goes beyond the scope of this paper. However, it is worth mentioning that sufficient clinical evidence is required and conformity with the regulatory requirements of the country where the final product will be used should be met prior commercialization. Basic information on some safety concerns is presented here.

2.4.1 Biological Safety Concerns

Medical implants including wireless systems must be biocompatible, biostable and properly sealed in order to resist against aggregations of surrounding body fluids and cells, reduce the possibility of tissue rejection reactions, and prevent physical components within the device from leaking out into the inner body. Therefore, proper selection of the implant material is a key factor for long-term success of IMDs implantation. A wide variety of metallic biomaterials, bioceramics, and biocompatible polymers can be used in medical implants. Comparative studies of these materials, their advantages and disadvantages are conducted in [127–129]. Particularly, coils or antennas need to be encapsulated with non-magnetic and electrically non-conductive materials to avoid absorption of electromagnetic flux line and eddy current losses in the coating. Otherwise, the wireless power transfer efficiency and the reliability of communication will deteriorate and heat dissipation may occur into the surrounding tissue.

2.4.2 Physical Safety Concerns

In addition to the biochemical properties, the mechanical structure and the surface properties of the implanted device need to be carefully designed. The size and shape of the medical device including the delivery system should be adapted to the implantation location which is patient and gender specific [36]. As the human body is very often in motion, the packaging must be able to endure strains and shocks. Also, to reduce the stress on the peripheral contact area of the implant/tissue, the implant should have a small volume and rounded edges. From this point of view, using a single inductive link is more appropriate than using multiple wireless links for wireless power and data transfer. The first approach may reduce the implantation tissue damage.

2.4.3 Electromagnetic safety concerns

While designing the IMDs wireless system, the electromagnetic field intensity and operation frequency have to be considered and carefully selected. They should meet international safety standards and they should not be a source of tissue damage or affect the IMD performance. The waves generated by wireless systems pass through biological tissues and are subject to frequency dependent absorption. Absorbed electromagnetic waves can lead to considerable heating of the tissues that surround implants and consequently cause irreversible tissue damage [130]. Energy absorption in tissue is quantified by measuring the specific absorption rate (SAR). It is defined as the amount of power which is dissipated per (absorbed by) unit mass

of tissue. The SI unit of SAR is watts per kilogram (W/kg). Different exposure limits to radiofrequency energy have been adopted according to countries (and even cities). However, most of the world countries use the International Commission on Non-Ionizing Radiation Protection (ICNIRP) guidelines to limit human exposure [131]. In the ICNIRP guideline, the SAR for general public should not exceed 0.08 W/kg over the whole body, 4 W/kg for arms, and legs local exposures, and 2 W/kg for head and trunk local exposures. All values are averaged over 6 minutes and all local exposures are to be averaged over 10 g. In general, 10 g of tissue occupies a volume of 2.15 cm^3, i.e. the tissue absorption should not exceed 20 mW to 40 mW in 2.15 cm^3 [132]. More details on guidelines and standards for human exposure to RF electromagnetic energy are described in [131].

2.4.4 EMI safety concerns

If not limited, electromagnetic interference (EMI) can negatively affects the operation of electronic devices. EMI is defined as disturbance that affects an electrical circuit due to electromagnetic induction or radiation. Aggressor EM fields can be emitted from components which are present within the device, such as inductors and transistors or from external sources placed in the vicinity of the IMD. EMI is a most common source of problems in medical devices.

Mobile phones, electronic security systems (store antitheft gates and airport security gates), and medical electromagnetic radiation devices (radiation therapy and magnetic resonance imaging (MRI) scanners) are some example of frequent EMI sources that may affect the operation of an IMD [133]. The electromagnetic fields produced by these sources may interfere with the IMD in several ways [134–136]: eddy currents may occur in the electrically conductive part of the implant (such as electrodes) and cause heating and damage to surrounding tissues; magnetic field gradient, during MRI for example, could exert force and torque on ferromagnetic parts of the IMD and dislocate the implant, thus damaging the device and its surrounding tissues; permanent magnets (used in commercial cochlear implants) could be demagnetized thus reducing transmission functionality.

EMI is more likely to occur if the frequency of the EM field is in the same range as the operating frequency of the IMD wireless system and if separate links are used for power and data transfer. The effects of the EMI, whether from internal or external sources, should be well considered by designers/manufacturers of medical devices.

In conclusion, the use of a single inductive link instead of multiple links for wireless power and data transfer reduces the size of the implant and alleviate design constraints on biological and physical aspects. It also reduces human exposure to EM fields and disturbances that

can affect the functionality of the implant due to EMI.

CHAPTER 3 ARTICLE 1: A 1.5 pj/bit, 9.04 Mbit/s CARRIER-WIDTH DEMODULATOR FOR DATA TRANSMISSION OVER AN INDUCTIVE LINK SUPPORTING POWER AND DATA TRANSFER

(The published paper is reproduced here)

Aref Trigui[1], Mohamed Ali [1,2], Ahmed Chiheb Ammari [3], Yvon Savaria [1], and Mohamad Sawan[1]

[1] Department of Electrical Engineering, Polytechnique Montreal (QC), Canada

[2]Microelectronics Department, Electronics Research Institute, Cairo, Egypt

[3] Department of Electrical and Computer Engineering, College of Engineering, Sultan Qaboos University, Muscat, Sultanate of Oman

Publication source:

A. Trigui, M. Ali, A. C. Ammari, Y. Savaria and M. Sawan, "A 1.5-pJ/bit, 9.04-Mbit/s Carrier-Width Demodulator for Data Transmission Over an Inductive Link Supporting Power and Data Transfer," in IEEE Transactions on Circuits and Systems II: Express Briefs, vol. 65, no. 10, pp. 1420-1424, Oct. 2018.

3.1 Abstract

This paper relates to a novel approach for downlink data transmission based on a Carrier Width Modulation (CWM). This modulation technique offers high performances and allows simultaneous data and power transmission over a single 27.12 MHz inductive link. A CWM demodulator is designed and fabricated in 130 nm CMOS technology. The proposed demodulator is intended for implantable medical devices, but can be applicable to other wireless systems. Excellent measurement results are obtained in comparison with state-of-the-art demodulators used in inductive communication systems. The proposed demodulator that was designed, fabricated and tested provides high-data rates at an ultra-low power budget and a very small silicon area of 2100 μm^2. More specifically, a data rate of 9.04 Mb/s can be achieved at a cost of only 13.68 μW power consumption. This represents an energy efficiency of 1.5 pJ/bit, that is 8 times smaller than the best state-of-the-art competitive demodulator.

Keywords - Inductive Link, downlink data transmission, Carrier Width Modulation, CWM demodulator.

3.2 Introduction

Due to their safety, simplicity and reliability, inductive links have, for a long time, been used to simultaneously transfer power and communicate with Implantable Medical Devices (IMDs) [50]. Up to date, it is the most popular if not the only wireless technique implemented in commercial IMDs. In recent years, several advanced IMDs such as endoscopic capsules, retinal prostheses, and brain machine interfaces have been developed. For all these devices, high data rate communications are required.

However, high data rate circuits generally involve high-power consumption, whereas the amount of energy wirelessly transferred should be utilized for the proper operation of the implant. For downlink (from the external device to the IMD) and uplink (from the IMD to the external device) data transfer, a special attention should be given to the demodulator and modulator designs, respectively. The aim is to achieve small size, low-power consumption, and high data rate communication in the implantable device. In this paper, we focus on the downlink communication and particularly on the demodulator circuit which plays a major role in data integrity and overall power efficiency of the IMD.

Downlink data transfer is primary based on carrier modulation to create detectable variations through the secondary coil. Commonly, such carrier variations are implemented using Amplitude Shift Keying (ASK) [99,137], Frequency Shift Keying (FSK) [138], or Phase Shift Keying (PSK). For ASK, if one of the amplitudes is equal to zero volt, the modulation is called On-Off Keying (OOK). Besides, data values can be encoded in the duration (instead of the amplitude) as in ASK-PWM (Pulse Width Modulation) and ASK-PPM (Pulse Position Modulation) [95]. ASK modulation and its derivatives are the simplest to implement and usually consume low power, but they generally fail to achieve high data rates. Also, they are highly sensitive to noise and all kinds of disturbances that may affect the carrier amplitude.

FSK modulation can offer high data rates and guarantees the best robustness against noise. However, it is rarely used because it requires a relatively wide bandwidth, in addition to its high power consumption and demodulator complexity.

On the other hand, PSK modulation and its derivatives, such as Orthogonal Quadrature PSK [14] or Quasi-Coherent PSK [101], have the advantages of lower sensitivity against noise and higher data rates. However, their main limitations are their high implementation complexity and power consumption.

Two solutions were proposed and patented by Ghovanloo et al. to achieve higher data rate (up to 20 Mb/s) without requiring too much power from the IMD [90, 139]. For these two methods, pulse-based techniques have been used over wideband inductive telemetry.

However, as these methods are carrier-less, they cannot be used to transfer both power and data over the same link. Therefore, separate sets of coils are required for data and power transfer.

Motivated by the need for high performance demodulators for downlink communication over a single inductive link that can be used for both data and power transfer, we proposed a novel modulation technique called Carrier Width Modulation (CWM), together with an original demodulator circuit allowing high data rate, ultra-low power consumption, and small silicon area.

Compared to our previous work in [81], this paper presents (1) a feasibility study; based on theoretical and simulation analysis; of the proposed generic CWM modulation technique, (2) an improved demodulator circuit design including testing blocks as well as (3) experimental validation results. Only a specific case of the generic CWM technique is considered in this paper; the one that achieves the highest data rate.

The remaining parts of this paper are organized as follows: Section II presents analytical and simulation results of an inductive link implementing the proposed CWM modulation. Section III discusses the main design considerations of the demodulator. Section IV shows experimental results and performance comparisons with competitive modulation solutions. Finally, concluding remarks are given in section V.

3.3 Proposed CWM Scheme

Figure 3.1 shows the conceptual illustration of our CWM proposed scheme. A binary data "0" is modulated by a sinewave signal during two carrier cycles $2T_c$ followed by a zero-signal for one cycle T_c. While a single sinewave cycle followed by two zero cycles are used to modulate the bit "1".

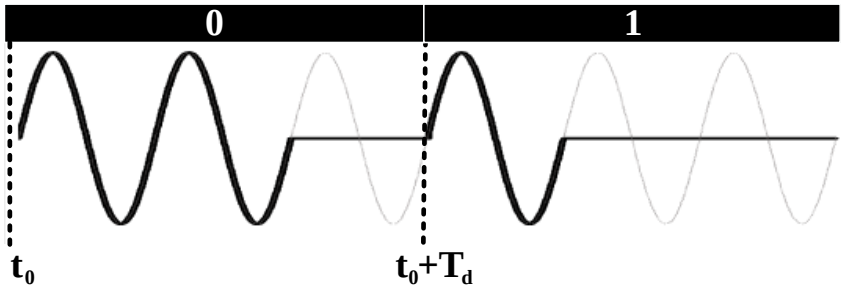

Figure 3.1 Conceptual CWM signal allowing 9.04 Mb/s data rate when using a 27.12 MHz carrier frequency

Since the data rate increases with the carrier frequency f_c, a 27.12 MHz f_c value was selected as it is the highest frequency for transcutaneous inductive transmission that belongs to the Industrial Scientific and Medical (ISM) bands [80]. At this frequency, the proposed modulation scheme allows a data rate of 9.04 Mb/s, that is equivalent to one third of the carrier frequency.

This proposed high data rate modulation is meant to be implemented using a single inductive link for simultaneous wireless power and downlink data transmission. The following question then arises: "Does the CWM modulated signal preserve its waveform after passing through an inductive link originally designed for efficient power transfer?". To appropriately answer this question, a feasibility study of a CWM modulation over an inductive link is carried out using theoretical and simulation analysis.

Figure 3.2 shows a simplified circuit model of an inductive link using CWM modulation. L_1 and r_1, L_2 and r_2 are the self-inductances and the series resistances of the primary and secondary coils, respectively. These coils are magnetically coupled through the mutual inductance M. v_s is the voltage source that drives the primary coil and R_L is the total equivalent load of the implant neglecting the non-linear load behaviour of the rectifier. Moreover, the capacitors C_1 and C_2 are used to tune the resonant frequency f_r of the primary and the secondary circuits at the carrier frequency f_c.

$$f_r = \frac{1}{2\pi\sqrt{L_1 C_1}} = \frac{1}{2\pi\sqrt{L_2 C_2}} = f_c \tag{3.1}$$

The proposed CWM signal can be generated by turning ON and OFF a switch in series with the primary coil, as shown in Fig. 3.2. This is dissimilar to the OOK modulation method, whose data modulation is implemented by switching ON and OFF the DC power supply [140] or the AC driver signal [103] of the power amplifier. Moreover, unlike OOK switching that can be performed at any time, the CWM switching is synchronized with the zero-crossing of the current i_1 flowing into the primary coil. In other words, i_1 is instantaneously interrupted at its zero-crossing. By doing so, all the energy of the primary LC circuit is stored as voltage on the series capacitor C_1 and virtually no energy is lost during the current interruption. This principle of preserving the energy in an LC tank at switching time was published in [97] and [117] for forward and backward data communication respectively. Their approaches aim to achieve high data rate with efficient power transfer over a single inductive link. The waveform of the received modulated signal, represented by the voltage at the terminals of the secondary capacitor v_2, should ideally be identical to the conceptual signal of Fig. 3.1. At first, we identified its phase Φ_{v_2} compared to the primary current phase Φ_{i_1}. Based on the phase analysis studied in [141] and the time domain simulation shown in Fig. 3.3, v_2 and

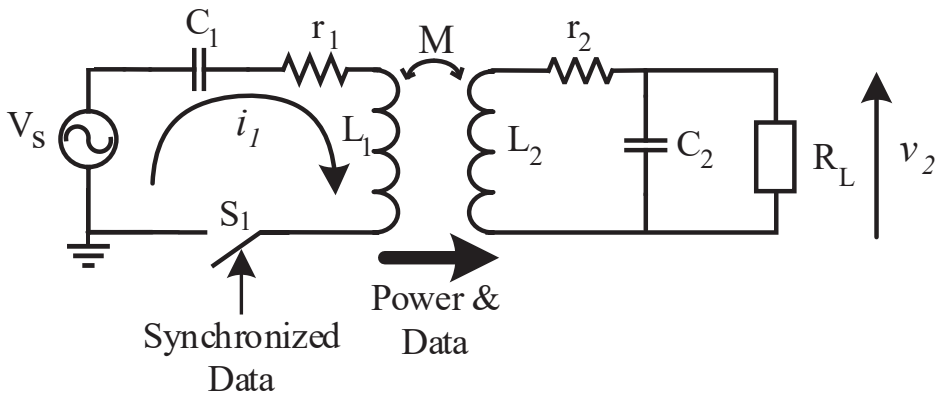

Figure 3.2 Simplified circuit model of an inductive link with CWM modulation

i_1 are in phase at resonance.

$$\Phi_{v_2} = \Phi_{i_1} \tag{3.2}$$

The variation of Φ_{i_1} and Φ_{v_2} depends mostly on the coupling factor $k = M/\sqrt{L_1 L_2}$ and the quality (Q) factor of the primary coil [141] but their phase relationship (Eq 3.2) would not change, as shown in Fig. 3.3. By definition, the quality factor of a coil is the ratio of the reactance to the real part of its impedance.

$$Q_1 = \frac{\omega L_1}{r_1}, Q_2 = \frac{\omega L_2}{r_2} \tag{3.3}$$

At resonance, these parameters are equals to the Q factors of the primary and secondary LC tank.

During the transient operation in OOK modulation, the energy stored in the primary capacitor and the coil circulates back and forth, leading to "ringing" effect figured by an unwanted oscillation of a voltage and current altering the modulated waveform. This ringing increases with the primary Q factor. The higher the Q factor, the narrower the bandwidth and consequently the longer it takes for the ringing to die out [90]. However, using CWM modulation, we will prove by simulation analysis that Q factors of the primary and secondary coils do not alter the received modulated waveform.

Figure 3.3a and Fig. 3.3b display the simulated waveforms of the primary current i_1 and the secondary voltage v_2 for different values of Q_1 and Q_2, respectively. These figures confirm that independently of Q_1 and Q_2, the suspension and resumption of i_1 oscillation occurs immediately at the switching time instants, without any ringing behaviour. However, as Q_1 increases, the dissipated energy by r_1 decreases, which implies the increase of the peak

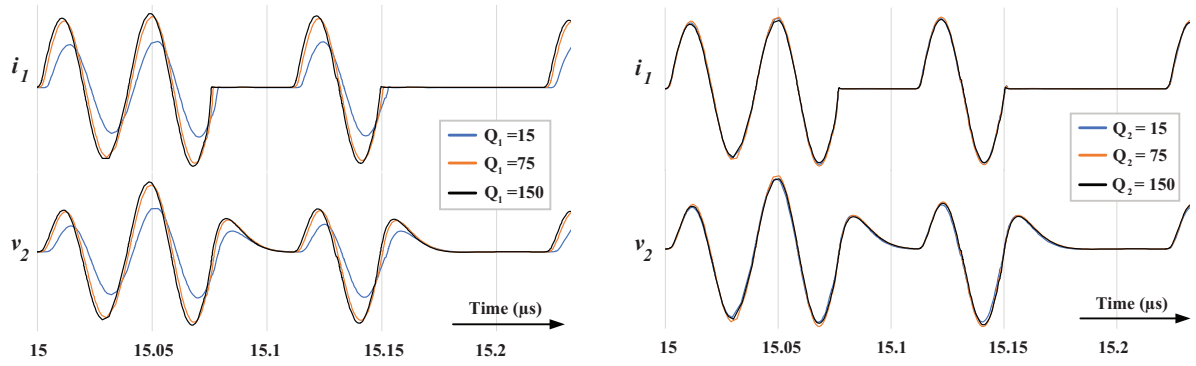

(a) (b)

Figure 3.3 The modulated signals i_1 and v_2 according (a) to the Q_1 variation (for Q_2= 15), (b) and the Q_2 variation (for Q_1= 15). The parameters are L_1= 5.27 µH, L_2= 1 µH, C_1= 6.54 pF, C_2= 34.5 pF, R_L= 100Ω, and k= 0.16

amplitude of i_1 and consequently a higher peak amplitude of v_2. On the other hand, the variation of Q_2 neither affects the waveform nor the amplitude of i_1 and v_2 (Fig. 3.3b). Since the coil geometry (size and shape) is often imposed by the IMD constraints, the proposed modulation scheme can use a wide range of coils (with different Q factors) while keeping a high data rate transmission.

Nevertheless, a half-sine wave transient v_2 voltage is observed at the primary current interruption and the v_2 resumption takes a half cycle to reach nearly its original voltage amplitude. This is consequent to the secondary capacitor and coil discharging and charging through the resistive load R_L. The CWM demodulator should therefore be designed taking into account these unwanted positive transient responses. This can be tackled either by synchronizing the CWM switching with the negative-going zero-crossing of i_1 or by inverting v_2 using an op amp in order to move the positive transient to the negative region. Consequently and as it is going to be demonstrated next, the designed CWM is insensitive to any unwanted transients if they are occuring at the negative alternances.

Based on this feasibility study, we proved that, unlike OOK modulation technique, our proposed CWM modulation method is less affected by the Q factor of the primary and secondary coils.

Further analysis of the secondary loaded Q factor on data and power transfer performances, with design improvements of the CWM demodulator aiming at tackling these impacts, will be the subject of a future work. For this paper, an ideal CWM modulated signal is gener-

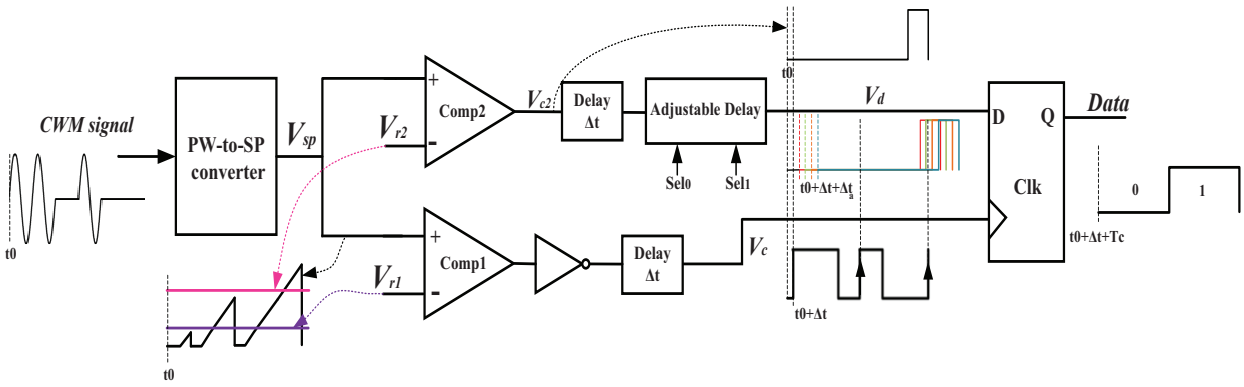

Figure 3.4 Block diagram and the associated waveforms of the CWM demodulator.

ated using an arbitrary waveform generator and only the CWM demodulator circuit will be developed.

3.4 Proposed CWM Demodulator Design

Figure 3.4 shows the block diagram of the proposed CWM demodulator. The core module of our demodulator is the front-end Pulse Width (PW) to Sawtooth Peak (SP) converter. The circuit diagram of the proposed PW-to-SP converter is shown in Fig. 3.5a. It consists of a current source (implemented as a passive resistor R), the current mirror M1-M2, and two transistors that switch alternately in order to charge or discharge the output capacitor (C_{out}). The charging occurs when the input signal of the PW-to-SP converter has an amplitude lower than the gate threshold voltage V_{th}, while the discharging happens in the opposite case. The aspect ratio (W/L) of the transistors and the values of R and C_{out} are carefully chosen to provide slow charging and very fast discharging, and accordingly a sawtooth signal V_{sp} is produced (Fig. 3.4).

The shape of V_{sp} and the performance of proposed PW-to-SP converter are relied on the width of the OFF periods. Therefore, this block is less sensitive to amplitude variations of the input signal than the conventional envelope detectors which depend substantially on the modulated signal amplitude [81]. As discussed in Section 3.3, unwanted transient at OFF periods is expected in practice. If this disruption does not exceed V_{th}, the proposed PW-to-SP converter does not perceive it and consequently it makes our demodulator robust against this kind of disturbance. That is why it is so important to move the positive transient to the negative region.

The peak values of the generated V_{sp} signal depend only on the charging duration. These

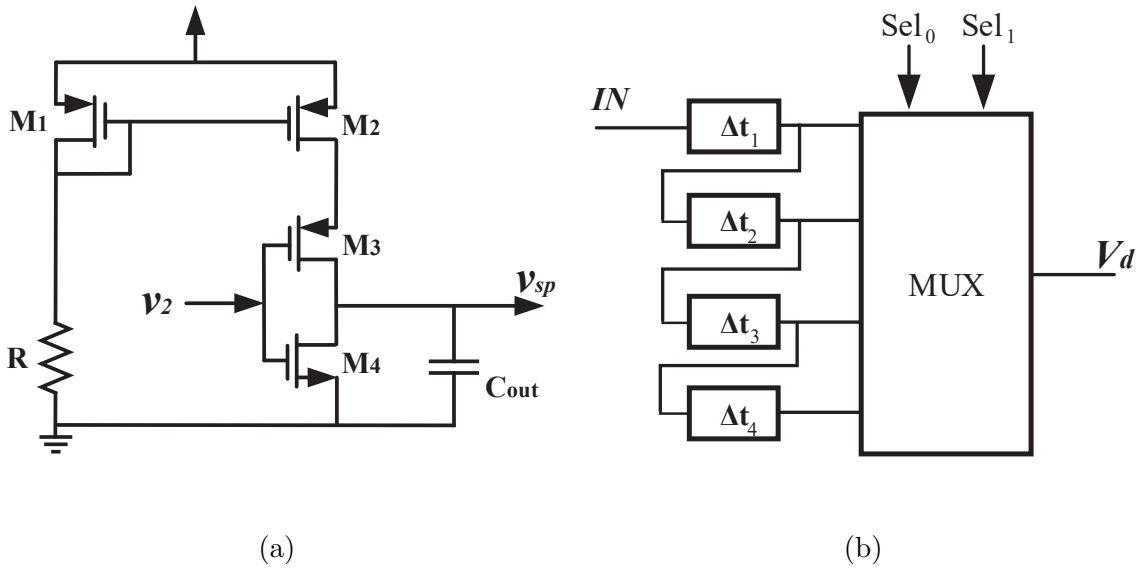

(a) (b)

Figure 3.5 (a) Circuit level implementation of the Pulse Width (PW) to Sawtooth Peak (SP) converter. (b) Block diagram of the adjustable delay.

peaks are compared with two reference voltages (V_{r1} and V_{r2}) using two comparators Comp1 and Comp2. The comparison between V_{sp} and V_{r1} is done by means of Comp1 in order to extract the envelope of the modulated signal V_c. The latter serves as a clock signal for synchronization purposes. As shown in Fig. 3.4, V_{r1} must be higher than the first sawtooth peak, resulting from the capacitor charging during the negative half cycle of the carrier. On the other hand, V_{r2} should be chosen between the second and the third sawtooth peaks, so that the data bits "1" and "0" can be distinguished. In order to acquire the baseband data signal, the output signal from Comp2 V_{c2} is delayed; such that the rising edge of V_c happens while V_{c2} is high and then fed into a D flip-flop that is synchronized through the generated signal V_c.

For this first demodulator prototype, the voltage references are applied from outside, where a resistive voltage divider has been used to produce V_{r1} and V_{r2} from the 1.2 V supply. In addition, to mitigate possible risk of desynchronization and possible delays due to process and mismatch variations, we added a delay element Δt at the output of each comparator and implemented a digitally configurable delay before the data input D of the latch element. Figure 3.5b shows the block diagram of the configurable delay, where four delay elements are integrated and one 4:1 multiplexer (MUX) is used to select the appropriate delay for synchronization. Depending on the state of the control signals (Sel_0 and Sel_1), the resulting amount of delay Δt_c can be $\sum_{i=1}^{4} \Delta t_i$, where Δt_1= 10 ns, and Δt_2= Δt_3= Δt_4= 5 ns. These

settings are implemented only for precaution measures to reduce the risk of malfunctioning after chip fabrication. In the experimental results reported in the next section, we fixed voltage reference levels to predefined values and we used only one delay element ($\Delta t_c = \Delta t_1$).

3.5 Experimental Results

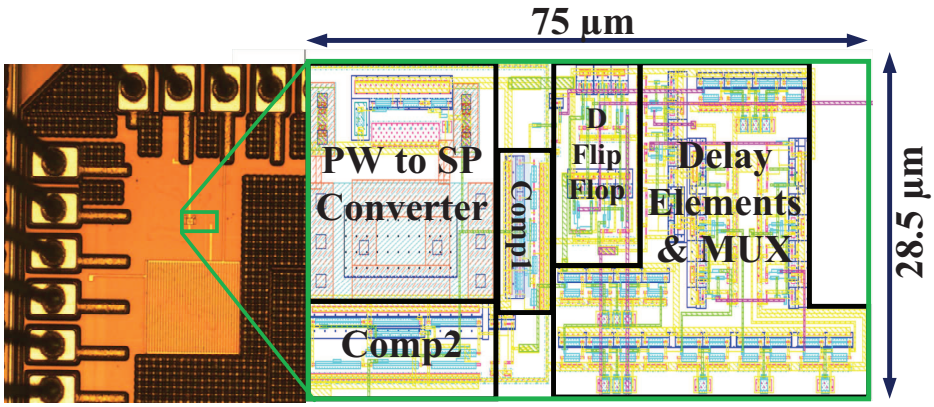

Figure 3.6 Chip micrograph and layout view of the proposed CWM demodulator.

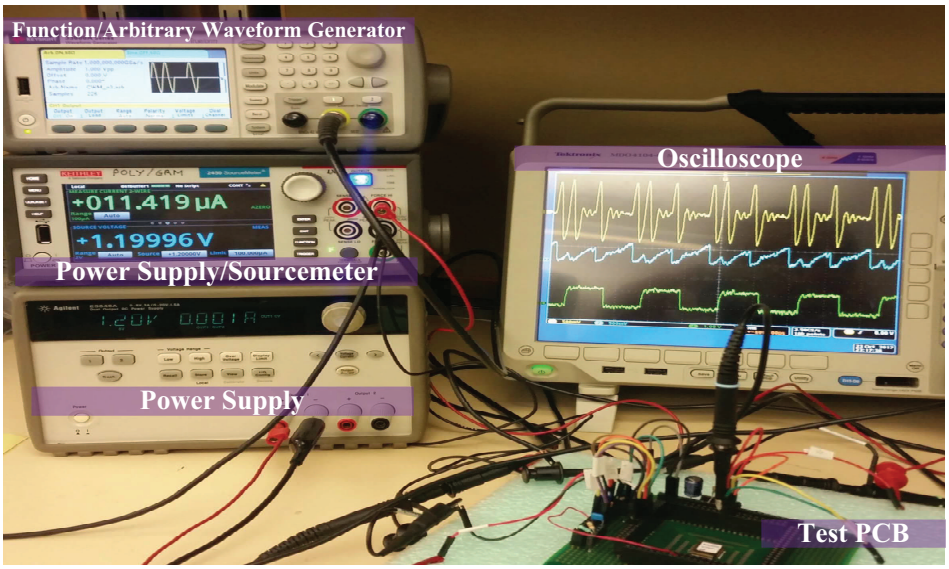

Figure 3.7 Photograph of the measurement setup.

In this paper, only standalone CWM demodulator was fabricated and tested to prove the proposed concept. To extract the experimental characteristics, a complete system will be

implemented to confirm the demodulator effectiveness in real-world usage. Figure 3.6 shows the chip micrograph and the layout view of the fabricated CWM demodulator in the IBM 130 nm CMOS technology, where a very small silicon area of 75 μm x 28.5 μm is occupied.

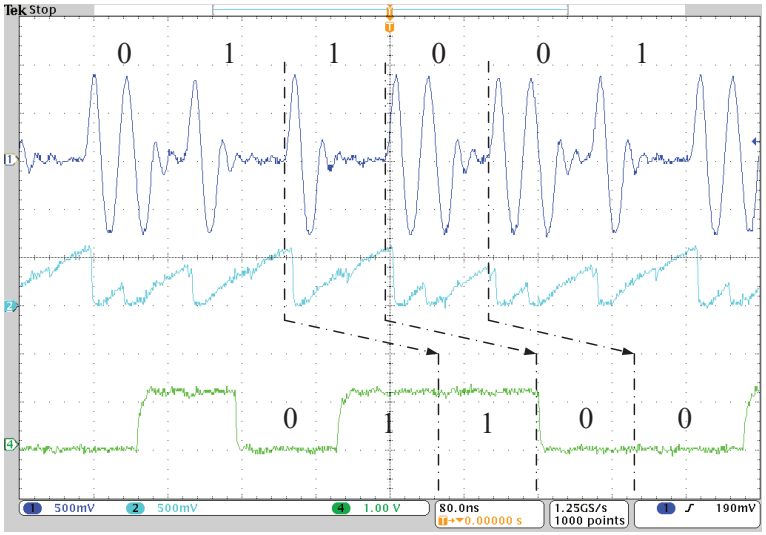

Figure 3.8 Measured waveforms: the CWM modulated signal (top), the PW-to-SP converter output (middle), and the demodulator output signal (bottom).

Figure 3.7 shows the measurement setup of the demodulator prototype. A 33622A Function/Arbitrary Waveform Generator was employed to generate the CWM ideal modulated signal. Two power supplies are used to generate 1.2V; one for supplying I/O-pads, voltage references, and all the blocks needed for testing purposes, such as inverter chains for the digital output and an analog buffer for the PW-to-SP converter output, while the other power supply (Keithley 2450 Sourcemeter) is used to supply the CWM demodulator and to sense its current consumption accurately. As shown in Fig. 3.7, the integrated demodulator was able to properly extract the baseband digital data at 9.04 Mb/s data rate ($f_c/3$) by consuming only 11.4 μA.

Figure 3.8 shows plots of the applied input signal, as well as the measured PW-to-SP converter output and the demodulator output signal. The small ripples associated to the input signal are due to the limited sampling rate of the waveform generator. As expected, the output is delayed by $\Delta t + T_d$ from the input.

A CWM inductive transmitter compatible with the proposed modulation approach will be implemented in a future work in order to measure the Bit Error Rate (BER) and the transmitted power for different distances separating the primary and secondary coils. However, for a preliminary test of robustness against noise of our proposed demodulation circuit, we

applied an Additive White Gaussian Noise (AWGN) to the applied modulated signal resulting in a Signal-to-Noise Ratio of 20 dB. The demodulator digital output remains the same as shown in Fig. 3.8; no bit error was noticed during 40 ms, i.e. for more than 10^6 demodulated bits.

Table I summarizes the measured performance of the proposed demodulator in comparison with previous state-of-the-art methods. Our demodulator requires only 3 carrier cycles per received information bit and achieves an ultra-low-power consumption of 13.68 μW at a data rate of 9.04 Mb/s corresponding to an energy efficiency (E/b) of 1.51 pJ/bit. Compared with its closest competitors, our proposed demodulator requires the minimal number of cycles per bit and the lowest energy consumption per bit in addition to occupying a very small operation area. Moreover, as the CWM modulated signal always includes the carrier for some significant fraction of the total time, the presented modulation technique can also be used for power delivery.

Table 3.1 Measured Performance of the Proposed Demodulator and Comparison with Prior Arts

Reference	Modulation scheme	CMOS Technology (µm)	Frequency (MHz)	Data Rate (Mb/s)	Number of Cycles/bit	Power Consumption (μW)	E/b (pJ/bit)	Active Area (10^3 µm^2)	Powering Ability
[99]	ASK[2]	0.35	6	1	6	200	200	2.05	Yes
[137]	ASK[1]	0.18	5	0.5	10	17	34	0.92	No
[101]	QCPSK[1]	0.18	4	0.8	5	59	73.75	5	Yes
[139]	PHM[2]	0.35	66.6	20	3.33	250	12.5	60	No
[142]	ASK[1]	0.18	13.56	6.78	2	348.75	51.44	80	No
[143]	ASK[1]	0.18	13.56	2	6.78	35	17.5	3	No
This work	**CWM[1]**	**0.13**	**27.12**	**9.04**	**3**	**13.68**	**1.51**	**2.1**	**Yes**

[1] A signal generator is adopted to produce the modulated signal.
[2] A transmitter is used to produce the modulated signal.

3.6 Conclusion

A novel modulation scheme supporting power and forward data transfer over a single inductive link and a simple CWM demodulator design was presented in this paper. The designed chip was fabricated in 130 nm CMOS and experimentally validated using an arbitrary waveform generator to produce the CWM modulated signal. The demodulator circuit consumes an ultra-low-power of 13.68 μW at 9.04 Mb/s and achieves an energy efficiency of 1.51 pJ/bit.

To our knowledge, our demodulator has the best reported energy efficiency that was measured for downlink data transfer over an inductive link. Moreover, the proposed demodulation approach can also be used for power delivery over the same inductive link. The obtained highly competitive performances are due to the use of a new effective modulation scheme together with an original PW-to-SP converter circuit.

CHAPTER 4 ARTICLE 2: ENERGY EFFICIENT GENERIC DEMODULATOR FOR HIGH DATA TRANSMISSION RATE OVER AN INDUCTIVE LINK FOR IMPLANTABLE DEVICES

(The published paper is reproduced here)

Aref Trigui[1], Mohamed Ali [1,2], Ahmed Chiheb Ammari [3], Yvon Savaria [1], and Mohamad Sawan[1,4,5]

[1] Department of Electrical Engineering, Polytechnique Montreal (QC), Canada

[2]Microelectronics Department, Electronics Research Institute, Cairo, Egypt

[3] Department of Electrical and Computer Engineering, College of Engineering, Sultan Qaboos University, Muscat, Sultanate of Oman

[4] School of Engineering, Westlake University, Hangzhou 310024, China

[5] Institute of Advanced Study, Westlake Institute for Advanced Study, Hangzhou 310024, China

Publication source:

A. Trigui, M. Ali, A. C. Ammari, Y. Savaria and M. Sawan, "Energy Efficient Generic Demodulator for High Data Transmission Rate Over an Inductive Link for Implantable Devices," in IEEE Access, vol. 7, pp. 159379-159389, 2019.

4.1 Abstract

In this paper, we present a new Carrier Width Modulation (CWM) scheme for simultaneous transfer of power and data over a single inductive link. An ultra-low power CWM demodulator is also proposed. Unlike conventional demodulators for a similar modulation scheme, the proposed CWM circuit allows higher-speed demodulation and simple implementation. It works well as a generic demodulator operating at a frequency range between 10 and 31 MHz. It also supports a wide range of data rates under any selected frequency from the operating range. A CWM-based scheme encoding two-bit-per-symbol, called Quad-level CWM (QCWM) is also proposed. The latter allows high data-rates-to-frequency ratios. Using a 0.13-μm CMOS process and 1.2 V power supply, both CWM and QCWM demodulators were implemented and fabricated. They respectively occupy die sizes of 2137 and 3256 μm^2 and

dissipate, in worst conditions, 16.9 and 35.5 μW. Compared with state-of-the-art demodulators used for inductive forward data transmission, the proposed demodulators are distinctive given their low-energy efficiency and small silicon areas.

Keywords - Carrier Width Modulation, Demodulator, Downlink Data Transmission, Inductive Link.

4.2 Introduction

There has been strong interest for wireless power transfer and fast data communication to Implantable Medical Devices (IMDs) [58,144]. The main goal is to ensure high power transfer efficiency and reliable high speed data transfer, while maintaining a small size and low power consumption of the implantable electronic circuits [145].

Among several wireless technologies such as RF [146], capacitive [147], ultrasonic [148], and optical [149] links, the inductive link, which consists of a magnetic-coupled pair of coils, is the most widely used wireless technique for both power and data transfer. This is mainly due to its ability to provide both power and bidirectional data transmission with appropriate reliability, safety, cost, and simplicity of implementation [150, 151].

Although considerable progress has been achieved in inductively coupled links for IMDs, many obstacles and design challenges still need to be addressed. Actually, the design of a transcutaneous data and power transmission system poses two main challenges. The first one is to achieve an efficient power transfer and high data rates at the same time. In fact, for conventional modulation techniques, the bandwidth needs to be widened to obtain high data rates, but narrowed to obtain efficient power delivery. The second challenge is to implement a small size and low power consumption IMD when establishing a robust high-speed communication link. The first challenge was addressed in our previous paper [15], and we proved using simulations that the bandwidth of our proposed CWM is independent of the quality factor of the primary and secondary coils Q_1 and Q_2, respectively. Therefore, high Q factors associated with narrow bandwidth do not limit the CWM communication rate.

In this paper, we mainly address the second challenge targeting downlink communications (from the external device to the IMD); particularly we focus on the demodulator circuit which plays a major role in data integrity and overall power efficiency of the IMD.

Several techniques have been proposed for downlink communication. Some notable proponents are Frequency Shift Keying (FSK) [138], Phase Shift Keying (PSK) [101], and Amplitude Shift Keying (ASK) modulation techniques [152]. PSK, FSK and their derivatives may offer high data rates and high immunity against noise, but they suffer from high implemen-

tation complexity and power consumption [153]. ASK is the most commonly used approach due to its easy implementation and the low power consumption of its demodulation circuit compared to other methods. However, the ASK scheme is less robust against disturbances that affect the carrier amplitude, such as interference and coupling variations. For better immunity, ASK with 100% amplitude modulation index; called On-Off keying (OOK); can be used [4]. Considered as the simplest and the least power-hungry modulation technique, special attention will be given to OOK and an analysis of its demodulator limitations will be discussed here to motivate our proposed solution.

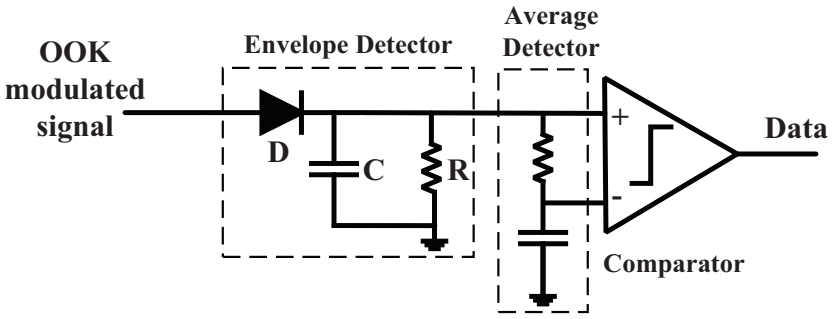

Figure 4.1 Typical block diagram of an OOK demodulator in an inductive link. It consists of an envelope detector, an average detector, and a comparator.

Despite its low design complexity and reduced power consumption, the data rate of OOK modulation, as it is the case for ASK modulation, is low due to the limited speed of its demodulator circuit. Figure 4.1 shows a typical block diagram of a conventional OOK demodulator. It uses an envelope detector (ED), which represents the weakest-link of the chain in ASK demodulators. Typically, the ED is composed of a diode followed by a capacitor C in parallel with a resistor R, as shown in Fig. 4.1. The time constant $\tau = RC$ determines the discharging time of the capacitor. For a faithful extraction of the modulated signal envelope, the time constant should satisfy the following inequality [77].

$$\frac{1}{f_c} \ll \tau \ll T_{min_{data}} \tag{4.1}$$

where $T_{min_{data}}$ is the shortest time interval between two binary words. This condition cannot be fulfilled for high data rate applications, as will be shown in Section 4.4. It has also been shown that the ED can consume significant power due to high dissipated power in the diode during the conduction phase [78].

Our work aims to solve this limitation to achieve a high data rate downlink communications over a single inductive link intended also for power transfer. In this paper, we propose two data modulation schemes for forward data transmission based on OOK called Carrier Width Modulation (CWM) and Quad-level CWM (QCWM), together with generic-CWM and QCWM demodulators allowing for high data rates, ultra-low power consumption, and small-silicon area.

Compared to our previous works in [15,80,81], this paper presents the following contributions: (1) A generic CWM demodulator able to cover a wide range of carrier frequencies from 10 to 31 MHz; (2) A sensitivity analysis on the main block (PW-to-SP converter) of the proposed demodulator; (3) An improved QCWM demodulator circuit design; as well as (4) Chip fabrication and experimental validation of the generic-CWM and QCWM demodulators.

The remaining parts of this paper are organized as follows: Section 4.3 presents analytical and simulation results of an inductive link implementing the proposed CWM modulation. Section 4.4 provides the proposed design solution allowing a high-speed demodulation as well as architectural and implementation details of the generic-CWM and the QCWM demodulators. Section 4.5 validates the functionality of the proposed demodulators and shows experimental results and performance comparisons with competitive demodulators. Finally, concluding remarks are given in Section 4.6.

4.3 Proposed Modulation Techniques

4.3.1 Modulation Schemes

The data rate of the proposed CWM technique can be configured by selecting different modulation codes and carrier frequencies f_c. This new technique looks similar to a pulse width encoded OOK modulation [154]. However, there are two key differences. The first one concerns the modulation circuit design; as will be discussed in the next section; and the second difference is related to the modulation timing. Unlike OOK switching that can be performed at any time, CWM data switching is performed at specific times which are the zero-crossing of the primary coil current.

The modulated waveform is characterized by the carrier cycle time T_c=$(1/f_c)$, the data bit period T_d and the ON and OFF widths for '1' and '0' data bits: t_{ON_1}, t_{OFF_1}, t_{ON_0} and t_{OFF_0}. These time-widths can also be expressed using the number of carrier cycles. As shown in Fig. 4.2, t_{OFF_0} and t_{OFF_1} are fixed to one cycle and two cycles, respectively. OFF widths are chosen to be as short as possible to ensure a short interruption of power transmission. However, t_{ON_0} and t_{ON_1} widths take (n-1) T_c and (n-2) T_c, respectively, where n is the number

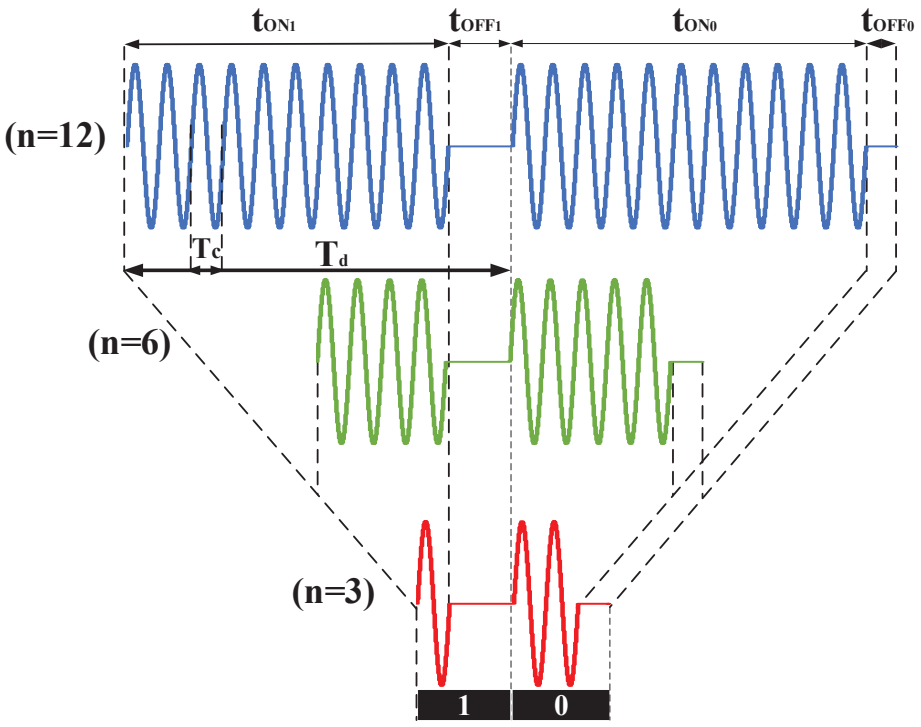

Figure 4.2 Proposed CWM scheme for different numbers of carrier cycles per data bit cycle, n: 12, 6 and 3 (from top to bottom)

of carrier cycles per data bit cycle. This number is an integer value that should be greater than or equal to 3. Three different data encoding of the proposed CWM scheme are shown in Fig. 4.2 according to various selected n values (12, 6 and 3 respectively from top to bottom).

Table 4.1 shows the corresponding data rates ($Data\ rate = 1/T_d = f_c/n$) calculated for some n values at 13.56 MHz and 27.12 MHz carrier frequencies. These frequencies belong to the range that can penetrate water and skin without tissue heating and potential damage (3 kHz-30 MHz) [50, 155]. As shown in this table, the maximal achievable data rate is obtained for $n = 3$. This topology allows achieving a data rate as high as 9.04 Mbit/s at 27.12 MHz carrier frequency.

For even higher data rates, we also proposed an enhanced CWM modulation scheme with quaternary symbols data encoding, called Quad-level CWM (QCWM) [80]. It consists of sending two bits per symbol by using four combinations of duty cycle ratio. One of the possible solutions consists on allocating a duty cycle ratio of 20% for the binary word '11', 40% for '10', 60% for '01', and 80% for '00', as shown in Fig. 4.3. In this manner, high data rates of $2/5^{th}$ of the carrier frequency can be reached. At 27.12 MHz, the binary data rate

Table 4.1 Combinations of data rates for different n values

	f_c	
	13.56 MHz	27.12 MHz
n	Data rates (Mb/s)	
100	0.1356	0.2712
50	0.2712	0.5427
6	2.26	4.52
3	4.52	9.04

would then reach 10.84 Mbit/s, i.e. 1.8 Mbit/s higher than the CWM maximal achievable data rate.

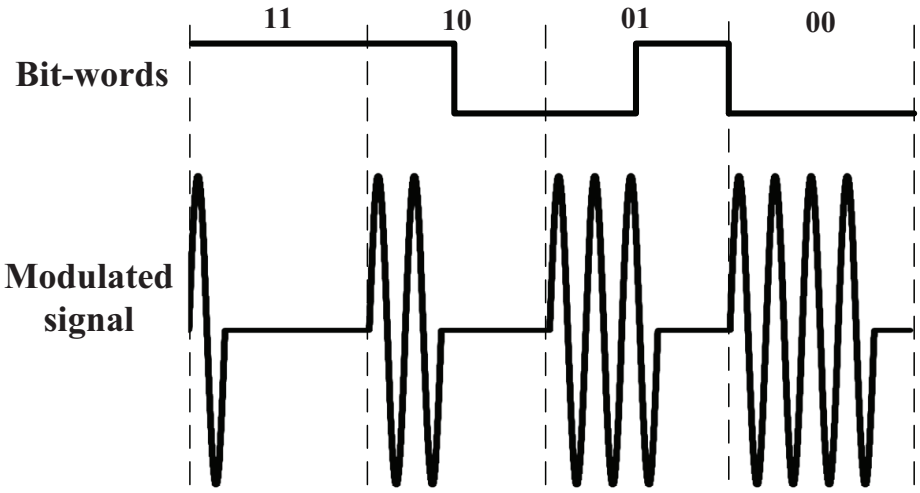

Figure 4.3 The waveforms of the proposed QCWM technique

4.3.2 Principle of Operation

CWM and QCWM data modulations can be carried out by opening and closing the primary LC circuit using a modulation switch S_1. Figure 4.4 shows a simplified circuit of the proposed wireless power and downlink data transfer system. L_1 and L_2 are the self-inductances of the primary and secondary coils, respectively, with a mutual inductance M, where $M{=}k\sqrt{L_1L_2}$ and k is the coupling factor between the two coils. C_1 and C_2 are capacitors used to tune the resonant frequency f_r $(= 1/2\pi\sqrt{LC})$ of the primary and secondary circuits at the carrier

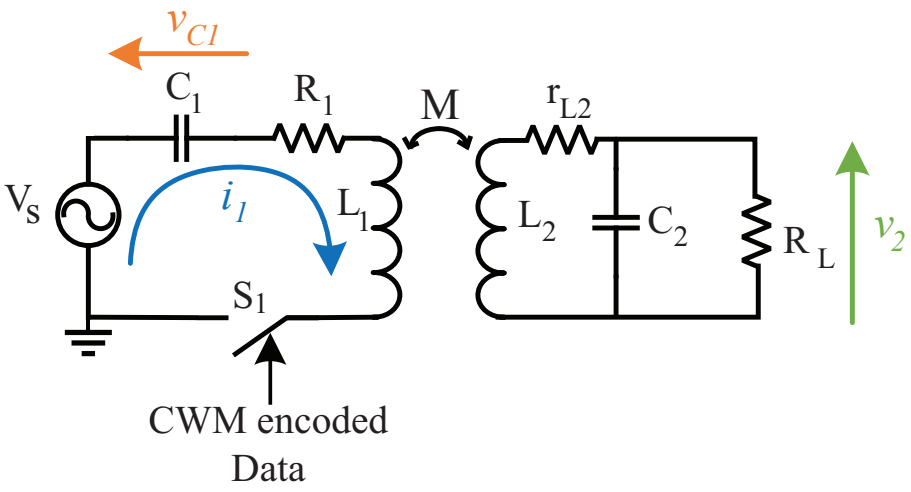

Figure 4.4 Simplified circuit of an inductive link with CWM modulation for wireless power and downlink data transfer system

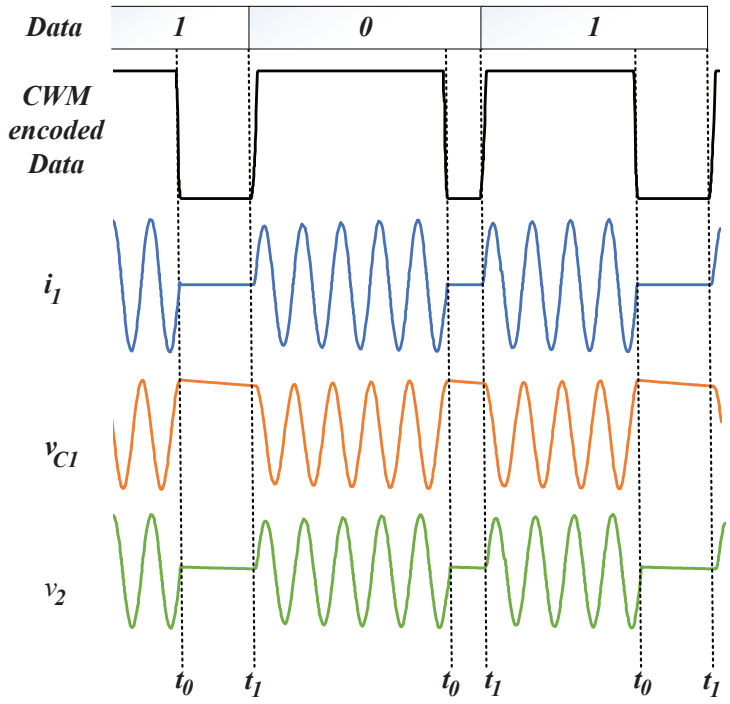

Figure 4.5 Simulated waveforms of CWM modulation scheme

frequency f_c. R_1 represents the total serial loss resistance on the primary side, including the loss resistance of the voltage source v_s and the internal series resistance of the primary coil. On the other side, r_{L2} is the series loss resistance in the secondary coil and R_L is the total equivalent load of the implant. The non-linear behaviour of the rectifier load is neglected in this analysis and R_L is considered as a DC load.

The switching of S_1 is synchronized with the zero-crossing of the current i_1 flowing into the primary coil. In other words, i_1 is instantaneously interrupted at its zero-crossing (t_0). In this manner, all the energy of the primary LC circuit is stored as voltage on the series capacitor C_1 and v_{C1} is at its extremum at the time instant t_0, as shown in Fig. 4.5. This principle of preserving the energy in an LC tank at switching time; to achieve high data rates with efficient power transfer over a single inductive link; is the same as the one adopted by the suspended-carrier modulation [97] and COOK [117] for forward and backward data communication, respectively. The energy preserving phenomenon was also validated by simulation in our previous paper [15].

As the OFF periods for CWM and QCWM are very short (one to four cycles), v_{C1} maintains almost this maximum voltage value until the next closing of the primary LC circuit at the time instant t_1. Virtually no energy is lost during the current interruption. Hence, the suspension and resumption of i_1 oscillation occurs without any transient responses, independently of the quality factor of the primary RLC circuit Q_1 ($= \omega L_1/R_1$, where ω is the angular operating frequency ($= 2\pi f_c$)).

At resonance, the voltage across the secondary coil v_2 and i_1 are in phase [141] and theoretically the waveform of v_2 should be similar to i_1. However, the secondary capacitor and coil discharging and charging through the resistive load R_{eq}, during the primary current interruption, may induce some unwanted transient responses in v_2 [15]. This phenomenon will be analyzed in-depth in a future work.

For this paper, ideal modulated signals are generated using an arbitrary waveform generator and only the demodulators circuits will be developed.

4.4 CIRCUITS IMPLEMENTATION

Typically, the proposed CWM and QCWM schemes can be demodulated using an OOK demodulator (Fig. 4.1) followed by an integrator circuit as used in ASK-PW demodulators [156]. The integrator is used to generate sawtooth waveforms whose amplitudes are proportional to the ON widths of the modulated signal. Figure 4.6 shows the simulated waveforms in a typical front-end ASK-PW demodulation stages when an ideal CWM signal is used as input.

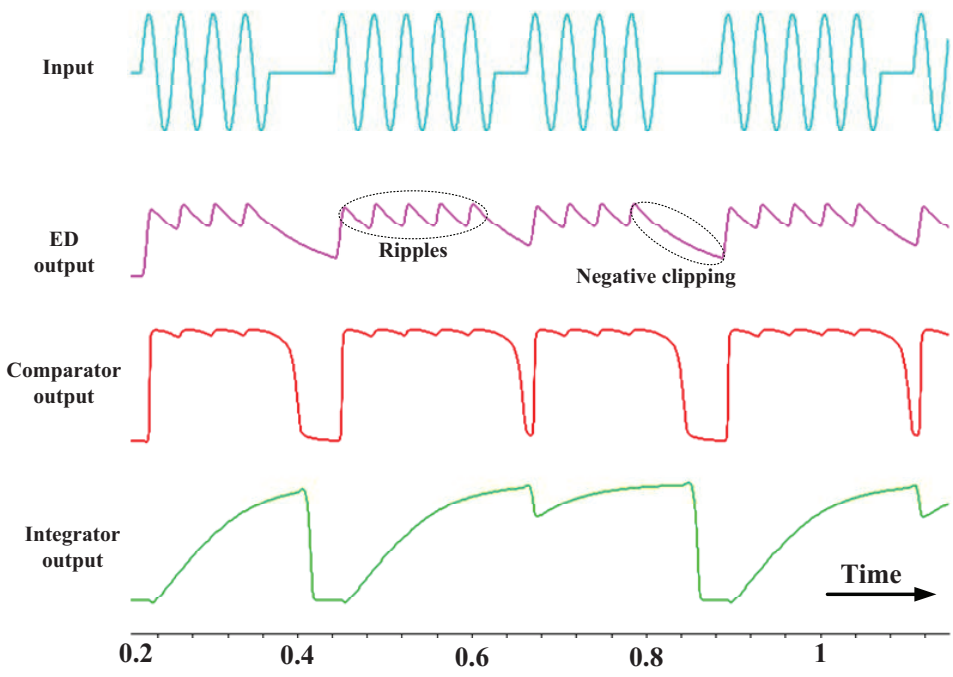

Figure 4.6 Simulated voltage waveforms (using Cadence) of the front-end ASK-PWM demodulator using the CWM modulation scheme

Even with an optimal time constant τ, the envelope detector (ED) output voltage has high ripples and negative peak clipping. Under practical situations, this signal will be degraded to some extent due to the presence of noise and amplitude disturbances [79].

To avoid conventional ED limitations, a proposed solution consisting of a dedicated module, called a Pulse Width to Sawtooth Peak (PW-to-SP) converter, is proposed. This module produces a waveform similar to that generated by an ASK-PW front-end demodulator, but it allows a high-speed demodulation and simpler implementation.

4.4.1 Pulse Width to Sawtooth Peak Converter

The circuit diagram of the proposed PW-to-SP converter is shown in Fig. 4.7. It consists of a constant current source generating a fixed current of 2.7 μA (using a resistor and a PMOS current mirror), and a complementary pair of p-type and n-type MOSFETs that switch alternately in order to charge or discharge the capacitor C_{out} ($= 200\ fF$). To improve the linearity of the generated sawtooth signal, C_{out} is integrated by a linear metal-insulator-metal (MIM) capacitor. The charging occurs when the input signal has an amplitude lower than the gate threshold voltage, while the discharging happens in the opposite case.

The PW-to-SP converter output signal *Out* has peak amplitudes that depend mainly on the

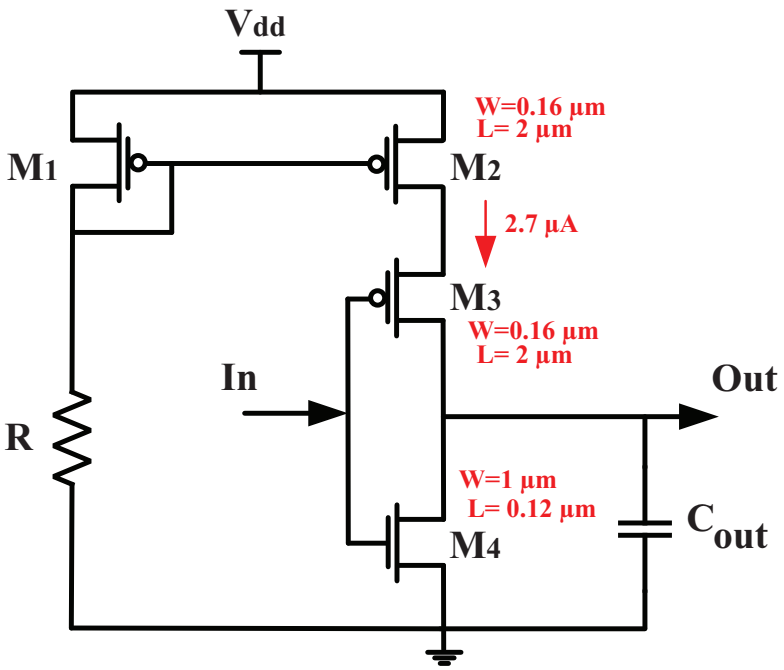

Figure 4.7 Circuit diagram of the proposed PW-to-SP converter

amount of charges stored into the output capacitance during OFF widths. The voltage across the output capacitor may be expressed as:

$$Out = \begin{cases} V_i(1 - e^{-t/\tau_C}) \text{ during the charging phase} \\ V_i e^{-t/\tau_D} \text{ during the discharging phase} \end{cases} \tag{4.2}$$

where V_i is the initial voltage across the capacitor i.e. at t=0. τ_C and τ_D are the time constants for charging and discharging C_{out}, respectively.

$$\tau_C = (R_{DS_2} + R_{DS_3})C_{out} \tag{4.3}$$

$$\tau_D = R_{DS_4}C_{out} \tag{4.4}$$

where R_{DS_2}, R_{DS_3} and R_{DS_4} are the ON-state resistances of M_2, M_3 and M_4 respectively. The aspect ratio (W/L) of these transistors have been designed in a way to increase sufficiently τ_C while reducing τ_D as much as possible, as shown in Fig. 4.7.

Sensitivity to n and f_c

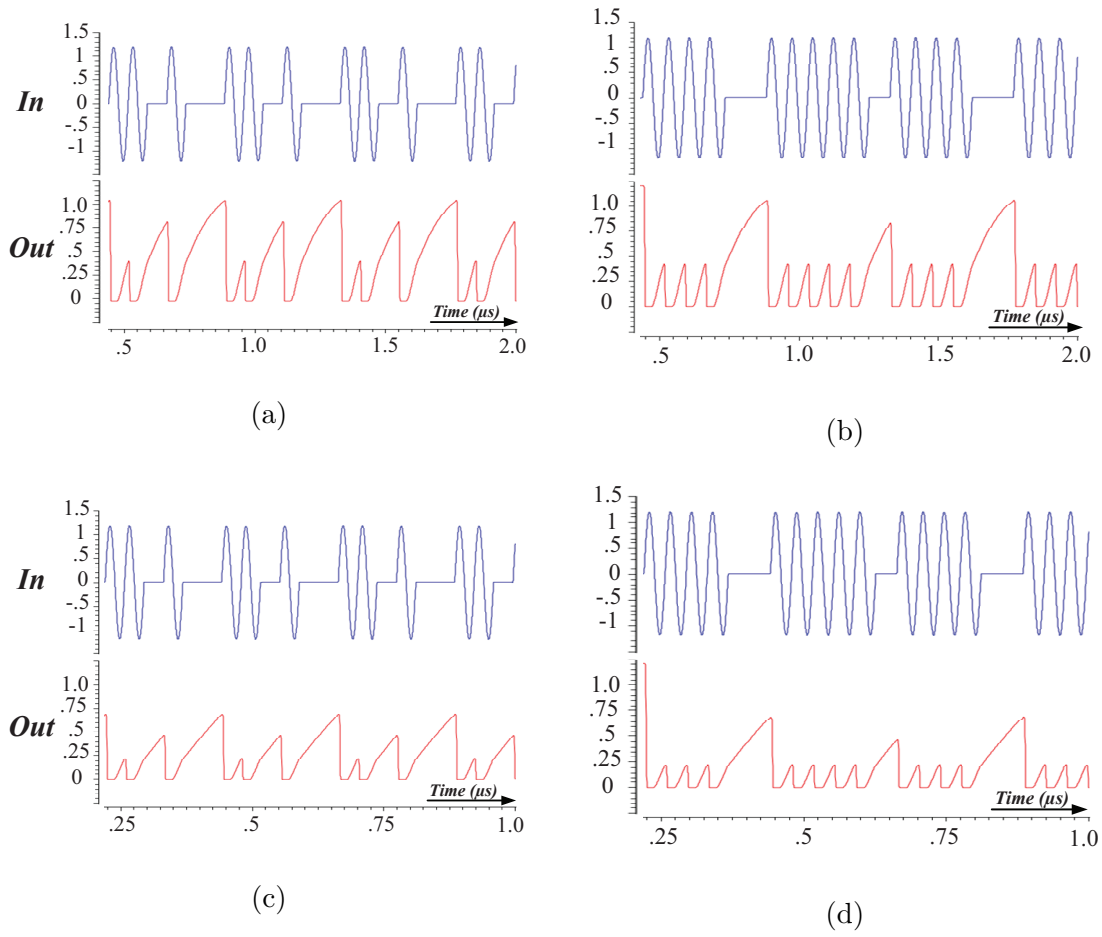

Figure 4.8 Simulated input and output signals of the PW-to-SP converter at f_c=13.56 MHz for (a) n=3 and (b) n=6, and at 27.12 MHz for (c) n=3 and (d) n=6

Figure 4.8 shows the simulated input and output signals of the PW-to-SP converter at two carrier frequencies for two different n. At a specific f_c, as the OFF-widths of the CWM signal are the same for all n from 3 to infinity, the sawtooth peak amplitudes would also be the same for all corresponding data rates. On the other hand, these peak amplitudes vary with f_c. However, the output signal keeps its sawtooth shape for a wide frequency range and the proposed PW-to-SP converter circuit is designed to operate at an f_c range from 10 MHz to 31 MHz as will be experimentally validated in Section 4.5.

Sensitivity to the input amplitude

In a typical inductive link application, the amplitude of the incoming modulated signal may vary due to noise amplitude as well as coupling or load variations. Therefore, the sensitivity of

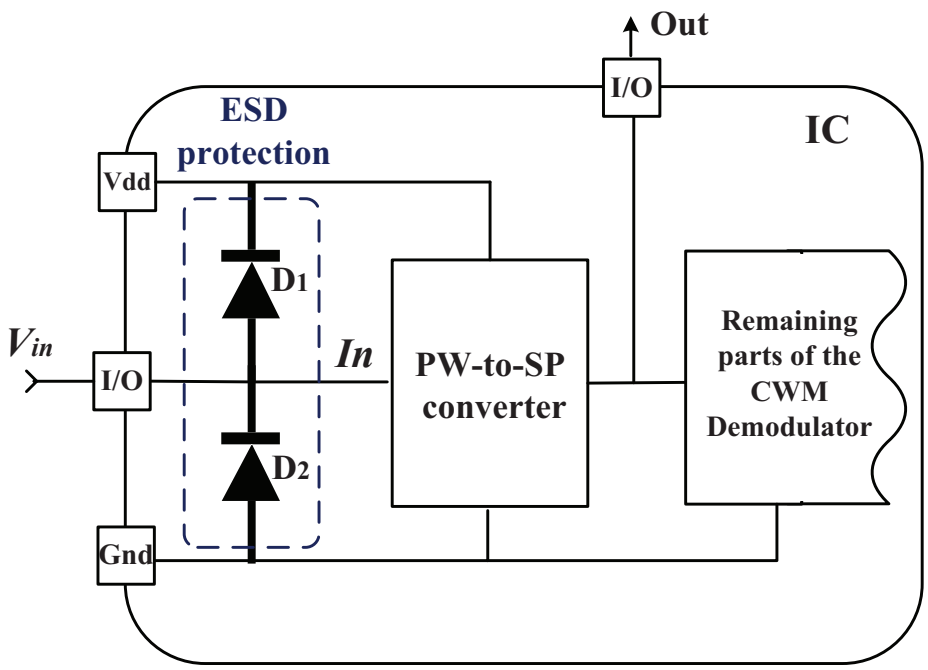

Figure 4.9 Typical double-diode ESD protection circuit. It ensure that the PW-to-SP converter input voltage never exceeds a certain level

the PW-to-SP converter to input voltage amplitude variations is studied using a parametric analysis simulation. For a more realistic simulation, the ESD (Electro Static Discharge) protection circuit placed between the input/output pad and the PW-to-SP converter is also taken into consideration. A typical double-diode network is used to protect the IC from positive and negative overvoltages as shown in Fig. 4.9. At positive over voltage conditions, D_1 become forward-biased (D_1 conducts) and the input voltage will be clamped to $V_{dd}+V_{D_1} = 1.2V + 0.9V = 2.1V$, where V_{D_1} is the voltage drop across D_1. The 0.9V may appear high for the turn on voltage of a Si diode but it is obtained by circuit simulation of the foundry cell with its associated parameters using Cadence-Spectre. Thus, In can never exceed $2.1V$ during the positive half cycle as shown in Fig. 4.10a. During negative overvoltage conditions, D_2 is forward-biased and In will be clamped to $-V_{D_2} = -0.9V$. Figure 4.10b shows the simulation results of the output signal of the PW-to-SP converter for different amplitude levels of V_{in} when applied to the I/O pad (taken from the foundry cell library).

When the amplitude of the input signal is below the threshold voltage of M4 (V_{th}= 430 mV), M4 could not provide a discharge path for C_{out} (Fig. 4.7). Therefore, the voltage across the capacitor will accumulate as shown in Fig. 4.10b. As long as V_{in} is sufficiently larger than V_{th}, the PW-to-SP converter provides almost the same peak levels. ESD protection is designed to withstand very high voltage surges up to few KVs. Accordingly, as the signal recovered

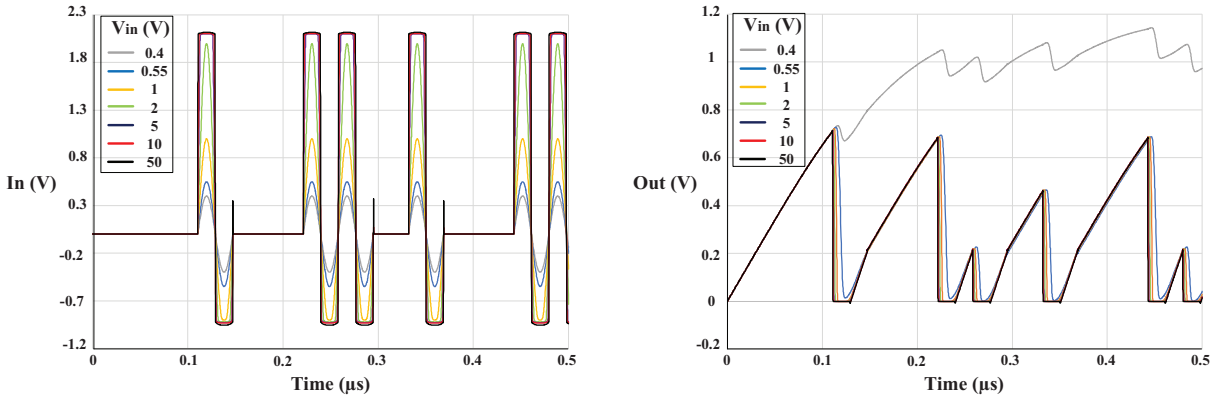

(a) (b)

Figure 4.10 Simulated (a) input, and (b) output signals of the PW-to-SP converter for different amplitude peak to peak values of V_{in} at f_c=27.12 MHz and n=3.

in the secondary coil v_2 does not exceed a few tens of volts, the proposed design associated with the ESD protection provides a high immunity against amplitude variations.

Also, the simulated results confirmed that the proposed PW-to-SP converter achieves an ultra low power consumption of 4.8 µW and occupies a small silicon area of 486 μm^2.

4.4.2 CWM Demodulator

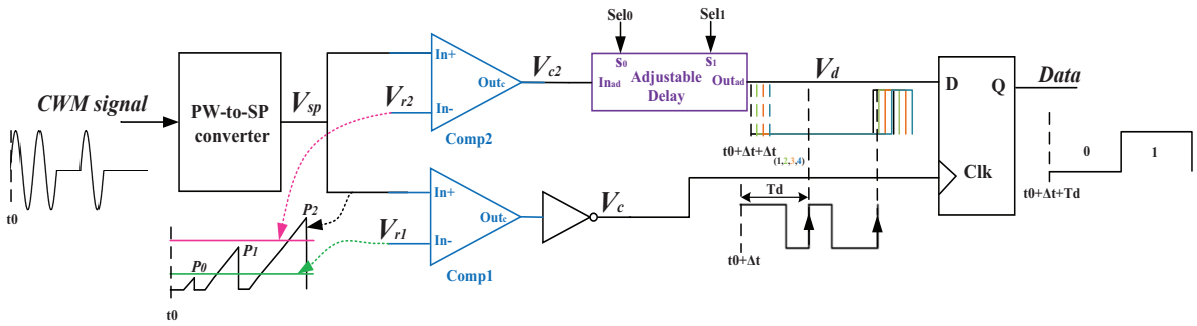

Figure 4.11 Block diagram and associated waveforms of the proposed CWM demodulator

The proposed PW-to-SP converter is the main and the first block of the CWM demodulator. Its analog output voltage V_{sp} is translated into two digital bit-streams by level detectors using two comparators and two voltage reference levels. The first bit-stream V_c, used for syn-

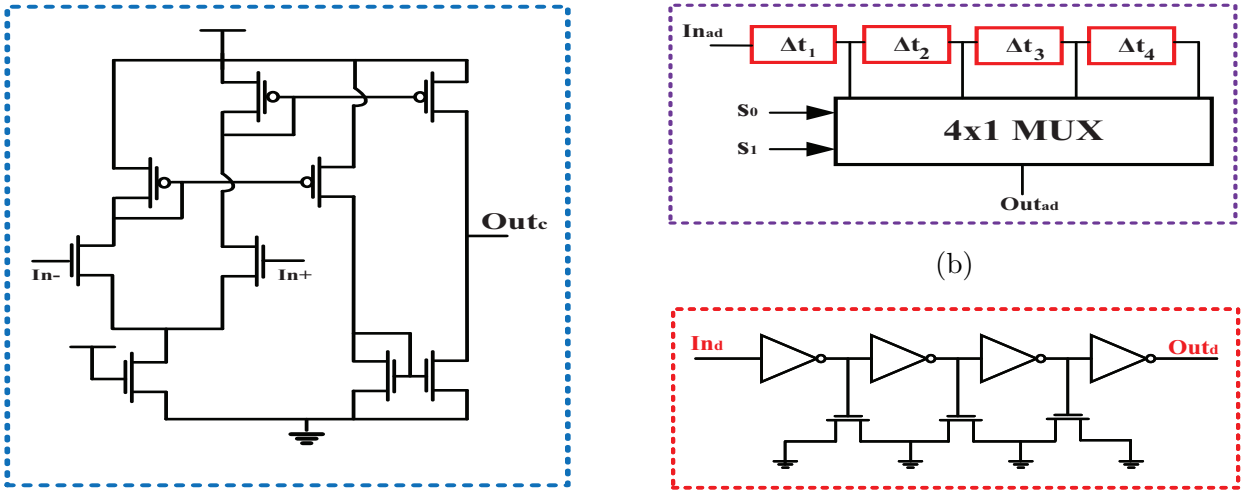

(a) (b) (c)

Figure 4.12 Schematics of the (a) comparator, (b) block diagram of the adjustable delay, and (c) the delay circuit.

chronization purposes, corresponds to the envelope of the modulated signal. It is generated from the comparison between V_{sp} and the voltage level V_{r1} followed by a digital inversion. As shown in Fig. 4.11, V_{r1} should be lower than the two sawtooth peaks (P_1 and P_2) but higher than P_0. On the other hand, the second bit-stream V_{c2} is recovered from the comparison between V_{sp} and another voltage level V_{r2} situated between P_1 and P_2 in order to distinguish between data bits '1' and '0'. The circuit diagram of the comparator is shown in Fig. 4.12a. In this version of our proposed demodulator, the voltage levels are applied from outside the chip and are adjusted according to the carrier frequency used.

Fig. 4.13 shows the ranges of V_{r1} and V_{r2} for different carrier frequencies where the proposed demodulator is functional. While decreasing the carrier frequency, the gaps between the peaks P_0, P_1 and P_2 increase and the operating range of the voltage references widens. However, this is not the case for 10 MHz compared to 13.56 MHz because at 10 MHz, the duration of t_{OFF_1} is too long, so that the peak P_2 saturates at the supply voltage 1.2 V and the gap between it and P_1 is reduced.

Afterwards, an adjustable delay, shown in Fig. 4.12b, is used to synchronize the V_{c2} bit-stream with the rising-edge of the delayed V_c. It integrates four delay elements and one 4:1 multiplexer (MUX) to select the appropriate delay for synchronization. The delay circuit is constructed using a number of inverter stages loaded by capacitors implemented by NMOS transistors, as shown in Fig. 4.12c.

Depending on the state of the selection signals (Sel_0 and Sel_1), the resulting delay can be

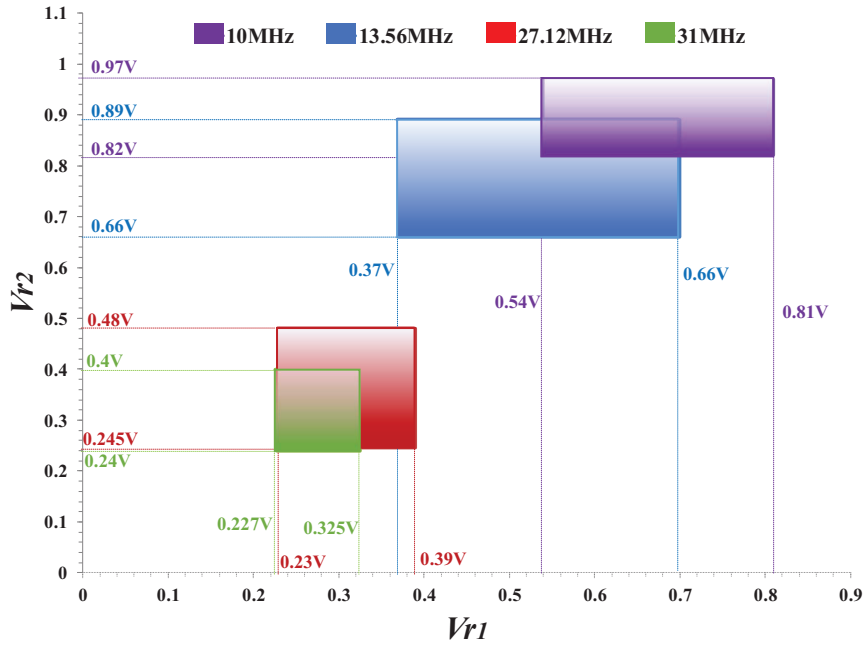

Figure 4.13 Ranges of V_{r1} and V_{r2} for different carrier frequencies at which the proposed system is functional.

$\sum_{i=1}^{m} \Delta t_i$, where $m \in \{1, 2, 3, 4\}$. This adjustment mechanism was implemented only to have more control for calibration after chip fabrication. In the experimental results reported in the next section, we used only one delay element (Δt_1= 10 ns).

4.4.3 QCWM Demodulator

Figure 4.14 shows the block diagram of the QCWM demodulator operating at 27.12 MHz carrier frequency. Like the CWM demodulator, it is based on the proposed PW-to-SP converter. However, the sawtooth signal V_{Qsp} is applied to four comparators (instead of two in CWM demodulator) to be compared with four different voltage references. The comparator Comp1 followed by an inverter are used to retrieve the envelope of the modulated signal V_{QCWM}, and applied to the sequential logic circuit as a clock signal. The three other comparators act as a two-bit flash for simultaneous analogue-to-digital conversion (ADC) producing 4 output states, as shown in Table 4.2. Digital outputs resulting from the comparison of the analogue signal with three voltage levels are then encoded into 2 bits using a 3-to-2 logic encoder. According to the truth table (Table 4.2), only one XNOR gate and two AND gates are used to produce outputs D_0 and D_1, where $D_0 = I_1$ AND I_2 and $D_1 = I_0$ AND (I_1 XNOR I_2).

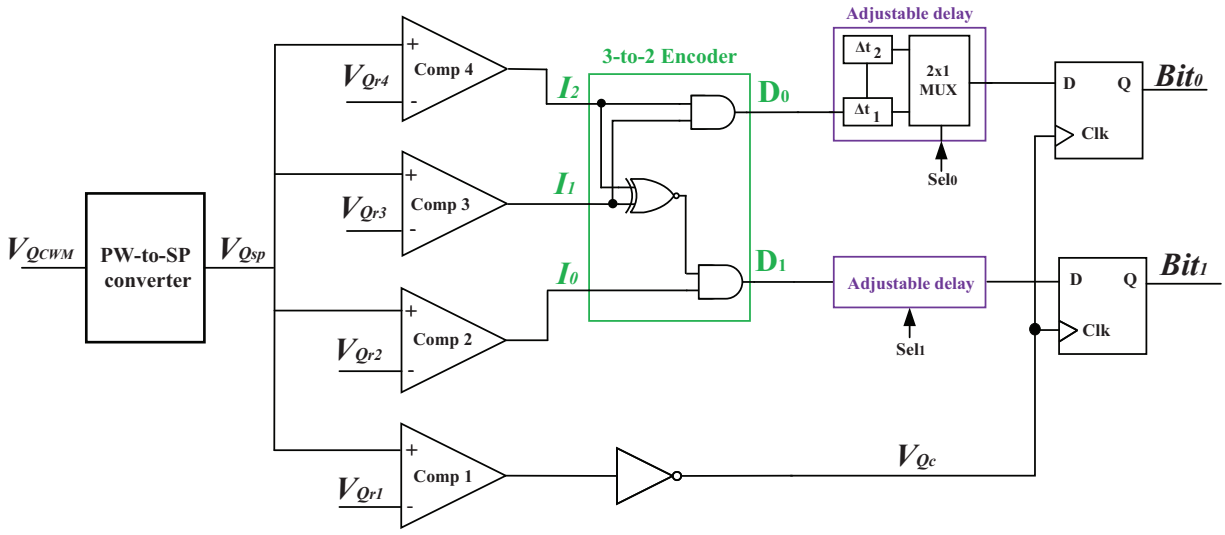

Figure 4.14 Block diagram of the QCWM demodulator

Conforming to the same principle of CWM demodulator, delay cells and D flip-flop elements are used for synchronization and data recovery purposes.

Table 4.2 Truth table of the encoder

State	I_0	I_1	I_2	D_0	D_1
$V_{Q_{sp}}>V_{Q_{r2}}$,$V_{Q_{r3}}$ and $V_{Q_{r4}}$	1	1	1	1	1
$V_{Q_{sp}}>V_{Q_{r2}}$ and $V_{Q_{r3}}$	1	1	0	1	0
$V_{Q_{sp}}>V_{Q_{r2}}$	1	0	0	0	1
$V_{Q_{sp}}<V_{Q_{r2}}$	0	0	0	0	0

Compared to a CWM demodulator, two comparators, one encoder, and one flip-flop element have been added in order to provide a 10.84 Mbit/s data rate (1.8 Mbit/s higher than that provided by CWM) at 27.12 MHz. The selection of the best modulation scheme between CWM and QCWM depends on the application requirements.

4.5 Experimental Results

Standalone CWM and QCWM demodulators were fabricated and tested to prove the concept. Figure 4.15 shows the chip micrograph and the layout view of the fabricated demodulators in 0.13-μm CMOS process. CWM and QCWM demodulators occupy small active areas of 2137,5 μm^2 and 3256 μm^2, respectively.

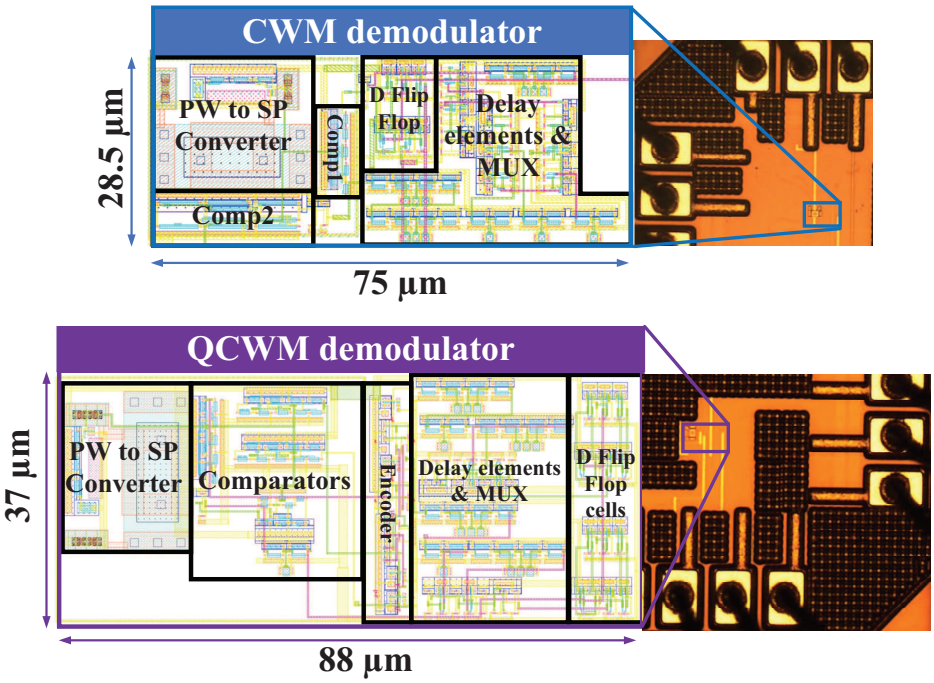

Figure 4.15 Chip micrograph and layout view of the proposed CWM and QCWM demodulators

In order to experimentally validate the functionality of our CWM demodulator with a wide frequency range, a Keysight Benchlink waveform builder software and 33622A Function/Arbitrary Waveform Generator were adopted to produce the modulated signals. Also, power supplies are used to power the demodulators and to generate the different reference voltages.

Figure 4.16 shows the measured voltage waveforms for repeated '0'-'1' pattern sequence using a CWM signal with four combinations of f_c and n. The applied CWM signals have been perfectly demodulated, however the reference voltage levels V_{r1} and V_{r2} had to be adjusted according to the used carrier frequency f_c (Fig. 4.13). Hence, practically, for a given application, V_{r1} and V_{r2} should be fixed from the beginning according to the application frequency.

Also, in order to confirm the genericity of our proposed CWM demodulator, the functionality of this demodulator under different f_c versus n is experimented as shown in Fig. 4.17 using a shmoo plot. The Pass/Fail criteria is defined by the reliability of the output data displayed on the oscilloscope during 40 ms.

The functionality of the proposed CWM demodulator is validated for a frequency band limited by a lower frequency of 10 MHz and an upper frequency of 31 MHz. Beyond these

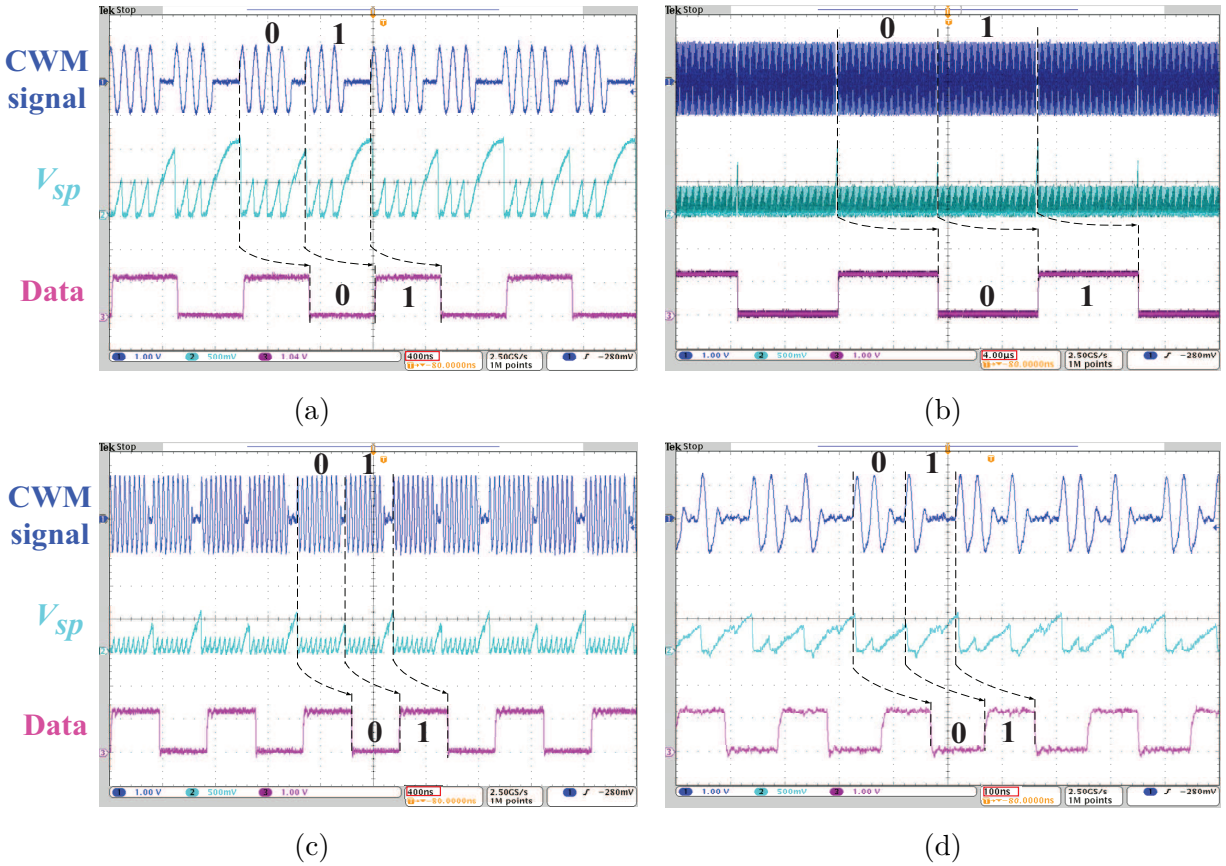

Figure 4.16 Measurement waveforms results of the proposed CWM demodulator for (a) f_c=10 MHz at n=5, (b) f_c=13.65 MHz at n=100, (c) f_c=27.12 MHz at n=10, and (d) f_c=31 MHz at n=3.

values, the distinction between the two sawtooth peak amplitudes (P_1 and P_2) becomes harder and output errors appear.

Figure 4.18 plots the measured power consumption of the CWM demodulator at different carrier frequencies and data rates. For a specific carrier frequency, the power consumption increases with data rates due to the increase of the energy dissipation in comparators since the mean energy of their non-inverting inputs signals (V_{sp}) increases with data rates. For the same reason, the power consumption increases when decreasing the carrier frequency. At lower frequencies, the sawtooth peaks P_1 and P_2 are high, which also requires higher voltage reference levels to be introduced on inverting inputs of the comparators. However, switching losses in PW-to-SP converter are increasingly significant at higher frequencies. This explains for example why the power consumption at 27.12 MHz, 30 MHz and 31 MHz, are close to each other.

f_c (MHz) \ n	100	10	5	4	3
9			Fail		
10					
13.56					
27.12			Pass		
31					
32			Fail		

Figure 4.17 Shmoo plot for carrier frequencies f_c versus the number of carrier cycles per data bit cycle n.

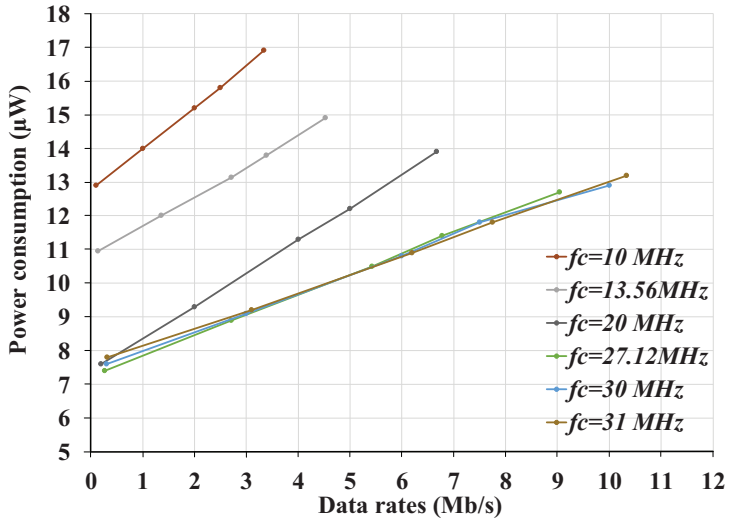

Figure 4.18 Measured power consumption versus data rates for different carrier frequencies.

The functionality of our proposed QCWM demodulator is also confirmed by experimental measurements using the same setup. In this test-bench, voltage references are applied from outside the chip, generated using resistive voltage dividers and a 1.2 V supply. Figure 4.19 shows the measurement results of the QCWM demodulator for repeated '11'-'10'-'01'-'00' pattern sequence of QCWM modulated signal. This demodulator achieves an ultra-low power of 35.5 μW at a data rate of 10.848 Mb/s corresponding to 3.27 pJ/bit.

Table 4.3 summarizes the measured performances of the QCWM demodulator and of the generic-CWM demodulator operating within the lower and upper f_c limits for $n = 3$. The table presents also competitive state-of-the-art demodulators used in inductive forward data transmission. Modulation methods reported in this table are divided into two groups. The first group includes methods intended for simultaneous power transfer over the same inductive

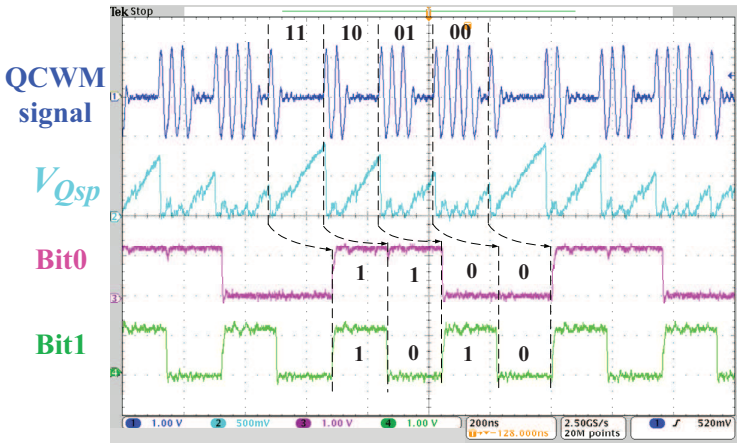

Figure 4.19 Measured waveforms of the proposed QCWM demodulator. The output digital bit-streams are delayed by $\Delta t + T_d$, as is the case for the CWM modulation.

link (indicated with 'Yes') and the second group includes methods optimized only for data transmission ('No').

For accurate comparison, we used figures of merit defined in [142] (FOM^1), and [137] (FOM^2).

$$FOM^1 = \frac{Data\ rate\ (Mb/s)}{Power(\mu W) \times area\ (\mu m^2)} \tag{4.5}$$

$$FOM^2 = \frac{Data\ rate(Mb/s) \times (Process)^2\ (\mu m^2)}{f_c(MHz) \times Power(\mu W) \times area(\mu m^2)} \tag{4.6}$$

Table 4.3 shows the superior performance of the proposed data demodulation techniques which achieve the lowest energy efficiency (E/b) and highest FOMs[1]. Also, our demodulators have high FOMs[2]. In addition, compared to the best published demodulators, the proposed CWM circuit operates at a wide range of carrier frequency, and data rates. Even at a carrier frequency as low as 10 MHz, the proposed system provides a very good energy efficiency of 5 pj/bit. The ultra-low power consumption of the reported circuit confirms that the CWM and QCWM techniques are applicable for low power battery-fed IMDs. Moreover, due to its genericity, the proposed CWM demodulator is convenient for a wide range of applications.

4.6 Conclusion

CWM and QCWM schemes allowing high data rates to carrier frequency ratio over a single inductive link for both power and data transfer were reported in this paper. These proposed modulation techniques maintain the advantages of ASK/FSK/PSK modulations. They allow

Table 4.3 Measured performance of the proposed demodulators and comparison with previous works

Simultaneous powering	**No**			**Yes**					
Reference	[142][a]	[137][b]	[89][b]	[138][b]	[101][a]	[143][a]	[99][a]	**This work[a]**	
Modulation scheme	ASK	ASK	PHM	DFSK	QCPSK	ASK	ASK	**QCWM**	**CWM**
Technology (μm)	0.18	0.18	0.35	1.5	0.18	0.18	0.35	**0.13**	
f_c (MHz)	13.56	5	66.6	5-10	4	13.56	6	**27.12**	**31**
Data rate (Mbit/s)	6.78	0.5	20	2.5	0.8	2	1	**10.85**	**10.3**
Power consumption (μW)	348.7	17	250	380	59	35	200	**35.5**	**13.2**
Silicon area ($10^3 \mu m^2$)	80	0.92	60	4840	5	3	2.05	**3.25**	**2.137**
E/b (pJ/bit)	51.44	34	12.5	152	73.75	17.5	200	**3.27**	**1.28**
FOM[1] $\times 10^{-2}$	0.02	3.2	0.13	0.13 $\times 10^{-3}$	0.27	1.9	0.24	**9.39**	**37.3**
FOM[2] $\times 10^{-2}$	0.06	20.7	0.25	–	2.2	4.55	$\cong 0$	**5.8**	**20.3**

[a] A signal generator is adopted to produce the modulated signal.
[b] A transmitter is used to produce the modulated signal.

low power consumption and simple implementation of the ASK modulation, while allowing high data rates and high immunity against amplitude disturbances ensured by PSK and FSK modulations. In addition, the genericity of the CWM demodulator was confirmed by operating under a wide range of data rates. Generic-CWM and QCWM demodulators fabricated in a 0.13-μm CMOS were implemented and tested. Measurements confirmed that the generic-CWM demodulator can operate at frequencies ranging from 10 MHz to 31 MHz, while offering an ultra-low power consumption. Moreover, comparisons with related works shows that our demodulators have the best energy efficiency for downlink data transfer over an inductive link supporting both power and data transfer.

Acknowledgments

The authors would like to thank CMC Microsystems for providing access to design tools and chip fabrication technologies.

CHAPTER 5 ARTICLE 3: GENERIC WIRELESS POWER TRANSFER AND DATA COMMUNICATION SYSTEM BASED ON A NOVEL MODULATION TECHNIQUE

(The submitted paper is reproduced here)

Generic Wireless Power Transfer and Data Communication System Based on a Novel Modulation Technique

Aref Trigui[1], Mohamed Ali [1,2], Sami Hached[1], Jean-Pierre David[1], Ahmed Chiheb Ammari [3], Yvon Savaria [1], and Mohamad Sawan[1,4,5]

[1] Department of Electrical Engineering, Polytechnique Montreal (QC), Canada

[2]Microelectronics Department, Electronics Research Institute, Cairo, Egypt

[3] Department of Electrical and Computer Engineering, College of Engineering, Sultan Qaboos University, Muscat, Sultanate of Oman

[4] School of Engineering, Westlake University, Hangzhou 310024, China

[5] Institute of Advanced Study, Westlake Institute for Advanced Study, Hangzhou 310024, China

Submitted to: IEEE Transaction On Circuits and Systems—I: regular papers

5.1 Abstract

This paper presents a wireless power and downlink data transfer system for medical implants operating over a single 10 MHz inductive link. The system is based on a Carrier Width Modulation (CWM) scheme for high-speed communication and efficient power delivery using a novel modulator circuit design. The modulation is produced by synchronized opening of a primary LC tank for one or two cycles according to the transmitted data. Unlike conventional modulation techniques, the data rate of the proposed CWM modulation is not limited by the quality factors of the primary and secondary coils. The functionality of the new modulation method is proven using a hybrid implementation comprising a custom-integrated demodulator circuit and board-level discrete components. The proposed Wireless Power and Data Transfer

(WPDT) system is also capable of operating under a wide range of data rates. It allows a maximum data rate of 3.33 Mb/s for a maximum power delivery of 6.1 mW at 1 cm coils separation distance. The system can recover more power, reaching 55 mW at 100 kb/s. Due to the system genericity, an operator can select the best compromise between power and data rates in accordance to application or current need, without reconfiguring the receiver. Another advantage of this modulation technique is the simple implementation and the ultra-low power consumption of the CWM demodulator despite its high-speed demodulation.

Keywords - Carrier Width Modulation, Downlink data transmission, Inductive Link, Simultaneous wireless power and data transfer.

5.2 Introduction

The use of inductive links for wireless transfer of power and data has grown dramatically over the last decade. Smartphones, home appliances, electrical cars, drones, and Internet-of-Things are some of the many applications employing this very convenient powering solution [157]. Wireless power and data transfer are also used in advanced technologies and systems. For instance, the medical sector relies heavily on such simultaneous transfer as it is easy to implement and may allow efficient and safe wireless power transfer with no significant risk of tissue heating if exposure limits (for the magnetic field strength) are respected [158]. Since the transmitter and receiver coils are in proximity to each other, the link is less sensitive to interference and external noise.

Unfortunately, despite its widespread use and its benefits, the implementation of a transcutaneous data and power transmission system remains a challenging task. This is due to two main challenges. First, efficient power transfer and high data rates communication are conflicting goals. In fact, transmission bandwidth needs to be widened for high data rates, but narrowed for efficient power delivery. Second, achieving high speed demodulation normally implies increasing power consumption and area of a silicon implementation.

A popular approach to address the first challenge is to use multiple dedicated inductive links for power and data telemetry, so that each link could be optimized independently [14]. However, this approach requires complex multi-coil structures, which results in bulky Implantable Medical Devices (IMDs) in addition to undesirable crosstalk. In order to increase the communication range and data rates, a far-field RF link can be used for data-transfer links [159]. Nevertheless, this approach increases the amount of energy dissipated as heat in the implantable part.

On the other hand, a single pair of coils used for both data and power transfer simultane-

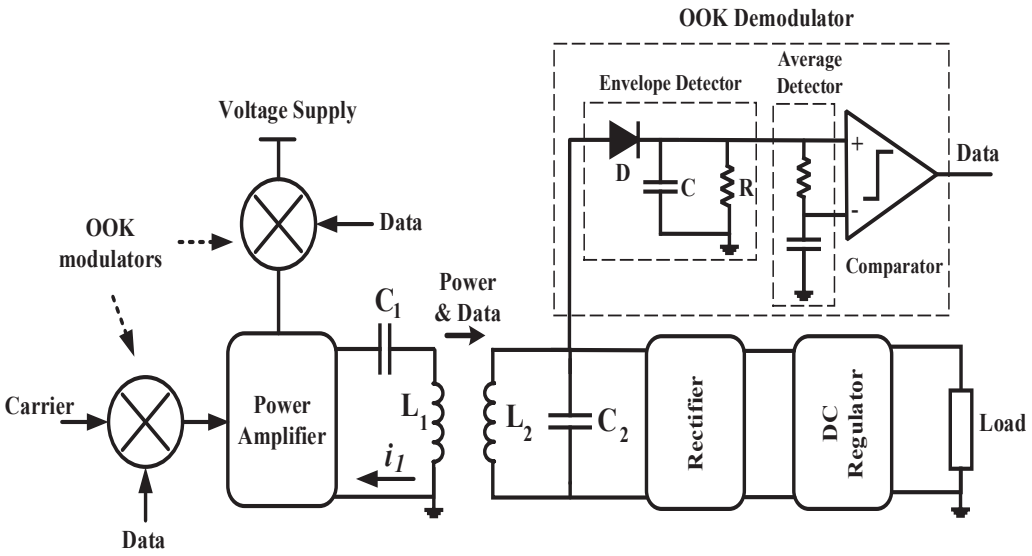

(a)

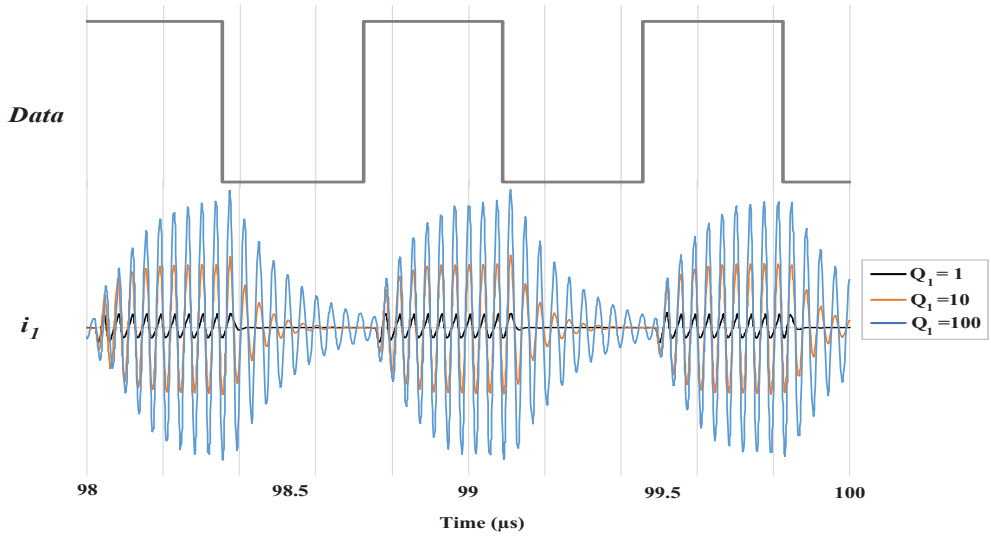

(b)

Figure 5.1 (a) Typical block diagram of data and power transmission via an inductive link using OOK modulation; and (b) The modulated OOK signal i_1 for various values of Q_1.

ously has obvious benefits. Mainly, the use of a single-frequency approach reduces design complexity, size, and cost. However, ensuring simultaneous high Power Transfer Efficiency (PTE) and high data rates over a single inductive link remains challenging. Such a challenge can be solved using appropriate modulation schemes for backward and forward data communications.

Although Load Shift Keying (LSK) is the most popular technique for backward telemetry (uplink communication), thanks to its low energy consumption and circuit complexity [100, 160, 161], a compromise between the inductive link PTE and data rate is unavoidable.

Recently, this challenge has been obviated using a novel passive modulation technique, called Cyclic On-Off Keying (COOK) [111]. This method was able to guarantee high data rates at low power consumption, without compromising the PTE. The main difference with LSK is the timing and duration of the switching. Using COOK, the LC secondary circuit is shorted only during a single cycle when the voltage across the secondary coil is zero and the current is at its maximum.

Regarding the forward communication, several techniques have been proposed. Some notable proponents are Frequency Shift Keying (FSK), Phase Shift Keying (PSK), and Amplitude Shift Keying (ASK) modulation techniques [152]. PSK, FSK and their derivatives, may offer high data rates and good power delivery, since their carriers have constant amplitude. However, they suffer from high-implementation complexity and high power consumption [153]. ASK is the most frequently used approach due to its easy implementation and the low power consumption of its demodulation circuit. However, the ASK scheme is less robust against disturbances such as interference and coupling variations that affect the carrier amplitude. For better immunity against disturbences, ASK with 100% amplitude modulation index; called OOK; can be used [4]. By contrast, this reduces the maximum amount of transferred power by around 50%.

Considered as the simplest and the least power-hungry modulation techniques [162], special attention will be given to OOK, and a detailed analysis of its limitations will be provided in this paper to explicitly introduce our proposed solution.

Figure 5.1a shows a typical block diagram of an inductive power and data transfer system using OOK modulation. At the transmitter part, data can be simply modulated by mixing the data bitstream with the carrier signal [74] or the DC supply voltage [75]. The resulting signal drives a class E Power Amplifier (PA) in order to amplify the current i_1 crossing the external coil L_1. This generates a magnetic field in L_1 surroundings. At the receiver side, the AC magnetic energy is recovered by the secondary coil (L_2), then rectified and regulated to convert the AC power to a regulated DC voltage to supply the IMD. A typical configuration

of an OOK demodulator consists of a voltage mode envelope detector, an average detector to produce the average voltage of the extracted envelope, and a voltage comparator to compare the envelope with its average value and recover the baseband data.

Despite its low design complexity and reduced power consumption, the data rate of OOK modulation, as it is the case for ASK modulation, is generally low for two main reasons :

1. The limited speed of the demodulator circuit due to the use of an envelope detector (ED) as explicitly explained in [82].

2. The maximal achievable data rate is limited by the quality factors of the transmitter and receiver coils due to the inversely proportional relationship between the Q factors and the bandwidth BW; as given by (5.1).

$$BW = \frac{f_c}{Q} \tag{5.1}$$

where f_c is the carrier frequency.

In fact, high Q factors increase the transient time, and thus limit the data rate [76]. To better understand the impact of the quality factor on the data rate, a time-domain simulation of the primary coil current i_1, using OOK modulation at a data rate equivalent to $f_c/10$, is performed for different quality factors of the primary coil Q_1, as shown in Fig. 5.1a. Obviously, the amplitude of i_1 and consequently the generated magnetic field strength increase at high Q factor. Therefore, a tank LC circuit exchanges voltage and current between the capacitor and the inductor just like a pendulum exchanges kinetic and potential energies. In an ideal tank circuit with no energy dissipation (infinite value of the quality factor), the free-running oscillation of the LC circuit would continue indefinitely, just as a frictionless pendulum would continue to oscillate indefinitely at its resonant frequency. Therefore, i_1 oscillations at high Q factors would take a longer time to die away after On-Off transition of the data signal, as shown in Fig. 5.1b. This figure clearly shows that a resonating tank with higher Q factor, which contributes to high PTE, responds slower to signal variations and reduces the maximal data rate.

Our work aims at tackling both limitations and to perform a high speed downlink communication and an appropiate power delivery over a single inductive link. In this paper, we propose a complete system of wireless power and downlink data transfer, based on a new modulation scheme called Carrier Width Modulation (CWM). Moreover, the proposed Wireless Power and Data Transfer (WPDT) system is generic. It operates under a wide range of data rates, without any adjustment or reconfiguration in the implantable side, using a dedicated ultra-low power and small silicon area demodulator circuit.

In our previous publications [15, 80–82], only the demodulator chip prototype was developed

and validated using an ideal modulated signal produced by an arbitrary waveform generator. In this paper, a complete prototype system for power and data transfer is implemented to validate our new modulation technique.

The following sections of this manuscript are organized as follows: Section 5.3 presents the proposed modulation scheme and evaluates its performance on an inductive link by simulation. Section 5.4 provides implementation details of the proposed WPDT system with more emphasis on the transmitter design. Section 5.5 validates the functionality of the proposed system and reports experimental results and performance comparison with state-of-the-art WPDT systems. Finally, concluding remarks are given in Section 4.6.

5.3 Proposed Modulation Schemes

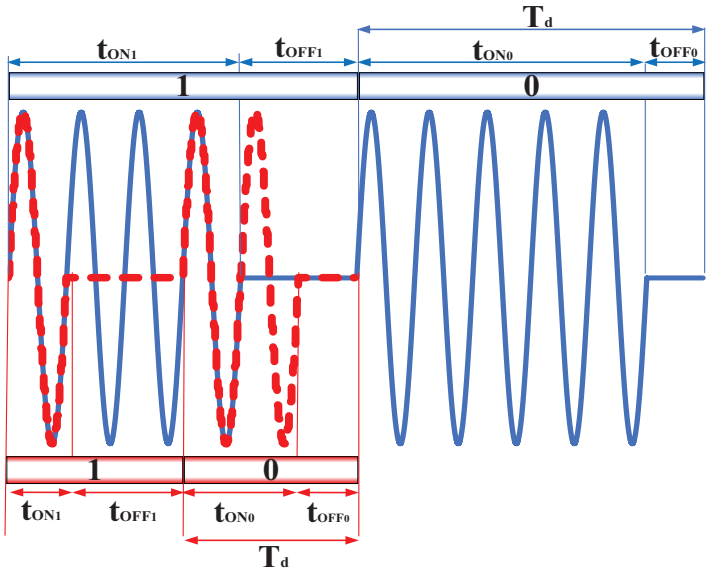

Figure 5.2 Proposed CWM scheme for n= 3 (red dashed line), and n= 6 (blue line).

To achieve a generic high-performance powering and data communication system, a new modulation scheme called Carrier Width Modulation (CWM) has been proposed by our team and was already described in previous papers [15, 80–82].

In summary, the CWM waveform is defined by the data bit cycle T_d, the carrier cycle T_c, and the On and Off width for either "1" and "0" data bits, t_{ON_1}, t_{OFF_1}, t_{ON_0} and t_{OFF_0}, as shown in Fig. 5.2. In order to limit as much as posssible the interruption of power transmission, OFF widths t_{OFF_1} and t_{OFF_0} of this proposed scheme are fixed to two cycles and one cycle, respectively. In order to maintain a data independent transmission rate for a given n, On widths t_{ON_1} and t_{ON_0} are designed to occupy (n-2) T_c and (n-1) T_c, where n is the number of

carrier cycles per data bit period T_d that can be any integer number greater than 3. Two data encoding examples of the proposed CWM scheme are shown in Fig. 5.2 for n=3 (red dashed line) and n=6 (blue line). Using CWM modulation, the data rates and the powering index (pi), which is a metric reflecting the amount of power transfer during communication [163], can be expressed according to n as

$$Data\ rate = \frac{1}{T_d} = \frac{f_c}{n} \tag{5.2}$$

$$pi = 0.5\frac{t_{ON_1} + t_{ON_0}}{T_d} = 0.5(2 - \frac{3}{n}) \tag{5.3}$$

The powering index equation is exact if an equal number of '1' and '0' bits are received. Figure 5.3 shows graphic representations of equations (5.2) and (5.3) for values of n ranging

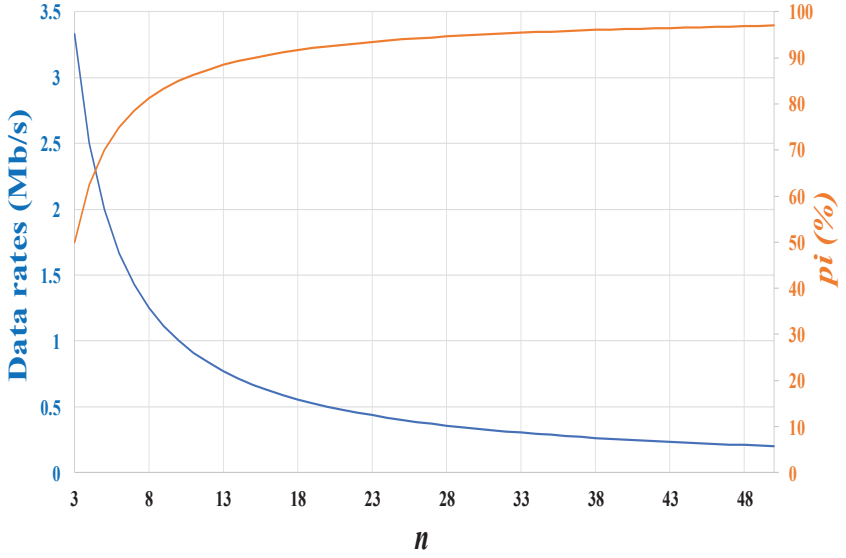

Figure 5.3 Data rates and powering index calculations pi for different values of n at 10 MHz.

from 3 to 50, at 10 MHz carrier frequency. The choice of carrier frequency will be discussed later in this paper. As shown in this figure, a maximal achievable data rate of 3.33 Mbit/s and minimal pi of 50% are obtained for $n = 3$. On the other hand, pi approaches 100% for a large value of n at the expense of lower data rate. Therefore, depending on the application requirements, the value of n can be selected to offer an optimal trade-off between the data rate and the pi.

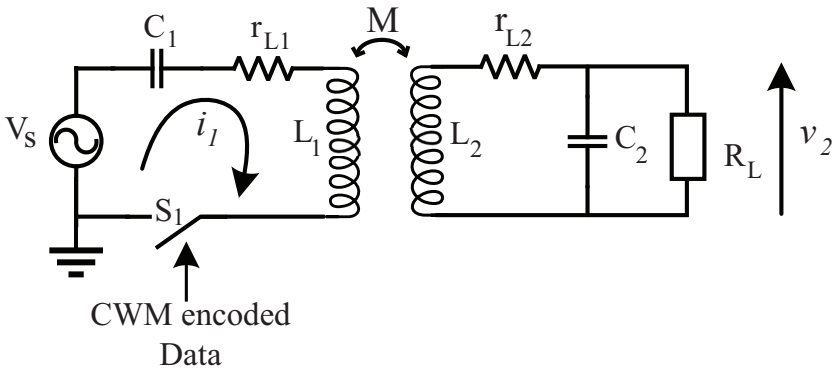

Figure 5.4 Simplified circuit of an inductive link with CWM modulation for wireless power and downlink data transfer system.

5.3.1 Operation Principle

Figure 5.4 shows a simplified circuit model of an inductive link using CWM modulation. L_1, r_{L1}, L_2 and r_{L2} are the self-inductances and the series loss resistance of the primary and secondary coils, respectively. These coils are magnetically coupled through the mutual inductance M, where $M{=}k\sqrt{L_1L_2}$ and k is the coupling factor between the two coils, which strongly depends on the separation distance and angle between the coils. C_1 and C_2 are capacitors used to tune the resonant frequency f_r $(= 1/2\pi\sqrt{LC})$ of the primary and secondary circuits at the carrier frequency f_c. v_s is the voltage source that drives the primary coil, and R_L is the total equivalent load of the implant (when the non linear load behavior of the rectifier is neglected).

Data modulation is carried out by opening and closing the primary LC circuit by switching Off and On the modulation switch S_1.

Unlike the previously discussed OOK modulation, the LC tank is instantaneously opened at the zero-crossing of the current i_1 flowing into the primary coil. At this time, all the energy of the primary LC circuit is stored as a voltage at its peak value on the series capacitor C_1. C_1 maintains almost all the energy for one or two cycles until the next closing of the LC circuit.

Figure 5.5 shows the simulated waveforms of the normalized primary current i_1 and voltage across the load v_2 for different values of R_L using high Q factor coils. At resonance, this topology ensures a zero-phase difference between i_1 and v_2, and validates the phase analysis studied in [141].

Furthermore, two interesting phenomena can be noticed:

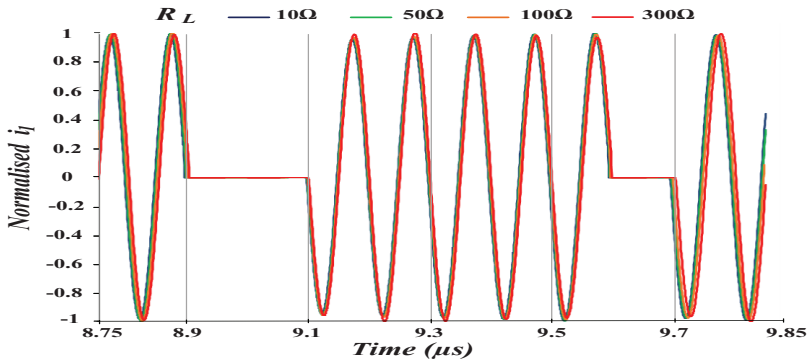

(a)

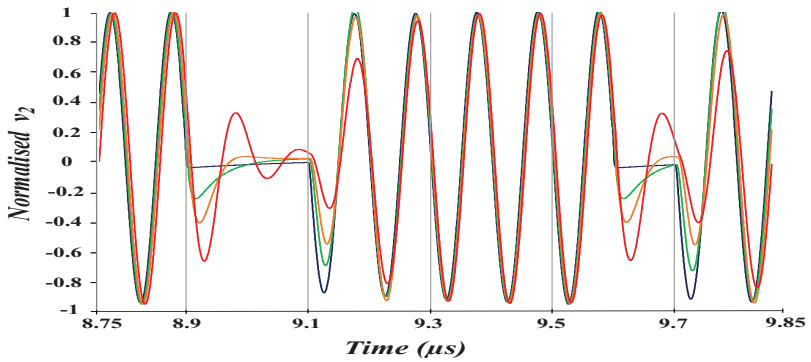

(b)

Figure 5.5 Normalized waveforms observed with CWM modulation operation of (a) i_1; and (b) v_2 for varous R_L values. Parameters used to obtain these responses are f_c = 10 MHz, n = 6, L_1 = 5.27 µH, r_{L1} = 1Ω, L_2 = 3.4 µH, r_{L2} = 263 mΩ resulting in Q_1 = 331 and Q_2 = 812, and k = 0.16. Values of C_1 and C_2 were chosen for 10 MHz resonance on both side.

1. A CWM synchronized circuit opening at zero-crossing of the current i_1 of a high Q primary resonating LC tank does not lead to the ringing effect as seen when employing an OOK modulation (Fig. 5.1b). During Off periods, the LC tank responds very fast and no oscillation occur. Therefore, unlike most of the other data modulation techniques, our proposed modulation method does not compromise data rates at the high Q of the primary coil aiming at high power transfer.

2. By contrast, a ringing effect occurs in v_2, when i_1 is interrupted, as shown in Fig. 5.5b. In fact, the energy stored in the capacitor and the coil of the secondary circuit circulates back and forth between the electric and magnetic fields and results in unwanted oscillations in v_2 during Off periods. It can be noticed that the ringing increases with R_L and it decays with time, but it does not vanish during Off periods for high R_L. However, for low R_L (i.e. $R_L <$ 50), only one-half cycle is needed to damp the oscillation. As R_L tends to 0 Ω, the half cycle

transient voltage tends to disappear. On the other hand, a very weak R_L can considerably decreases the voltage across L_2 in an impractical way. Therefore, a resonant secondary tank is not appropriate to get a modulated signal free of unwanted oscillations for a large and practical load range.

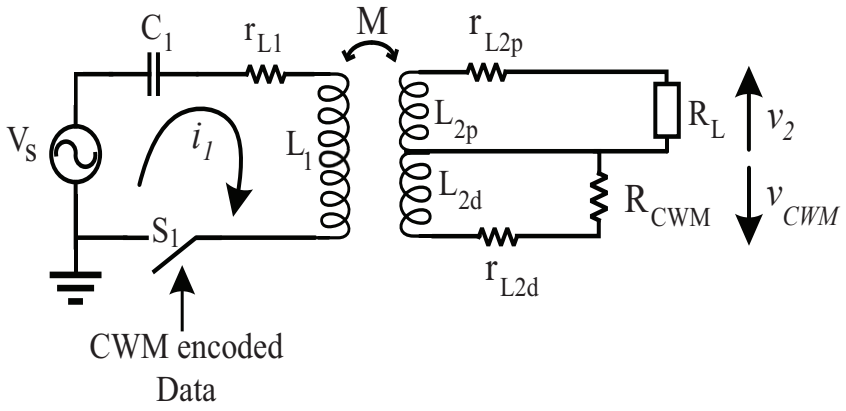

Figure 5.6 Simplified circuit of the proposed non-resonant inductive link using a tapped secondary coil. r_{L2_p} and r_{L2_d} are the series loss resistance of the two sub-coils L_{2p} and L_{2d}, respectively.

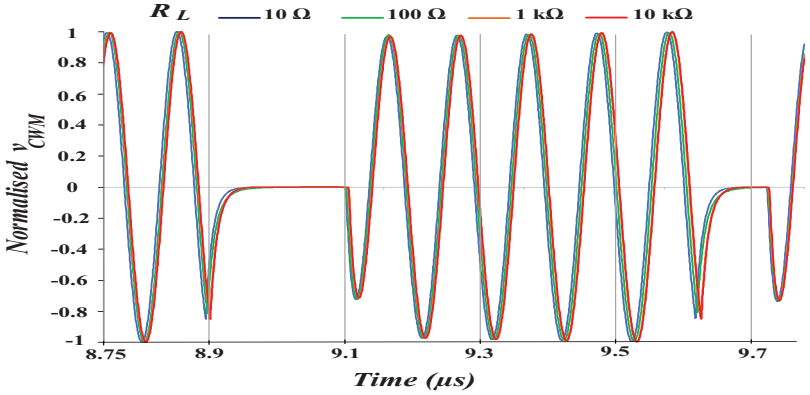

Figure 5.7 Normalized v_{CWM} signal according to R_L variation. The parameters are f_c= 10 MHz, n= 6, L_1= 5.27 µH, r_{L1}= 1Ω, L_{2p}= 2.4 µH, r_{L2p}= 138 mΩ, L_{2d}= 1 µH, r_{L2d}= 125 mΩ resulting in Q_{2p}= 1092 and Q_{2d}= 502, R_{CWM}= 70 Ω, and k= 0.16.

To overcome this issue, a non-resonant secondary circuit with no capacitor is proposed. However, in practice, parasitic capacitances such as the internal capacitance of the secondary coil and the junction capacitance of the diode (used for rectification) can induce a ringing effect. That is why a tapped coil configuration was used as shown in Fig. 5.6. In fact, the secondary coil was split into two sub-coils L_{2p} and L_{2d}, which are respectively dedicated to

power and data recovery. In order to damp any potential oscillations during Off periods, a low value resistance R_{CWM} is connected to L_{2d}. The normalized primary current waveform with this approach is the same as in Fig. 5.5a. However, since the secondary circuit is operating out of resonance, the primary current and the secondary voltage v_2 are out of phase. The advantage of this approach is that the v_{CWM} waveform; which represents a damped and an inverted image of v_2; is not affected by the load value as shown in Fig. 5.7. This advantage is obtained at the expense of the power transfer efficiency, since part of the recovered energy is absorbed by R_{CWM}. Hence, R_{CWM} value should be carefully chosen to ensure a good compromise between damping and power consumption.

5.3.2 Power Transfer Efficiency

PTE is defined as the ratio of the power dissipated in the total load resistance R_L to the power generated from the voltage source v_s.

$$PTE = 100 \times \frac{P_L}{P_s} \tag{5.4}$$

Simulation analysis of PTE according to the variations in k, Q_1, Q_2 and R_L are shown in Fig. 5.8a, 5.8b,5.8c, and 5.8d, respectively, for different values of n (3, 6 and 100). Since the powering index pi increases with n, it makes sense that a higher n increases PTE, as shown in all the reported results.

Figure 5.8a shows that PTE increases almost linearly with a high slope according to the coupling factor k. The primary and secondary quality factors of coils Q_1 and Q_2 also contribute to the increase of PTE, as shown in Fig. 5.8b and Fig. 5.8c. However, it is noticeable that the slope is larger at quality factors below 100. Hence, quality factors greater than 100 are recommended for higher PTE.

Figure 5.8d shows that PTE depends as well on R_L and a maximum PTE occurs at an optimal load condition. For a complete power recovery system, the PTE curve may change due to the non-linear behaviour of the rectifier and the DC regulator.

Even though our preferred solution is to use a non-resonant secondary, in order to characterise the impact of that design decision, we also simulated the case where the secondary would be resonant. The result of that possible design choice is also reported in Fig.5.8d. For this case, only R_L values that can ensure both power transfer and data communication have been considered (i.e. for low R_L). In this condition, the proposed non-resonant secondary circuit shows 33% less power efficiency in the worst case. On the other hand, our non-resonant circuit is much more robust to load variations while ensuring simultaneous power and data

transfer.

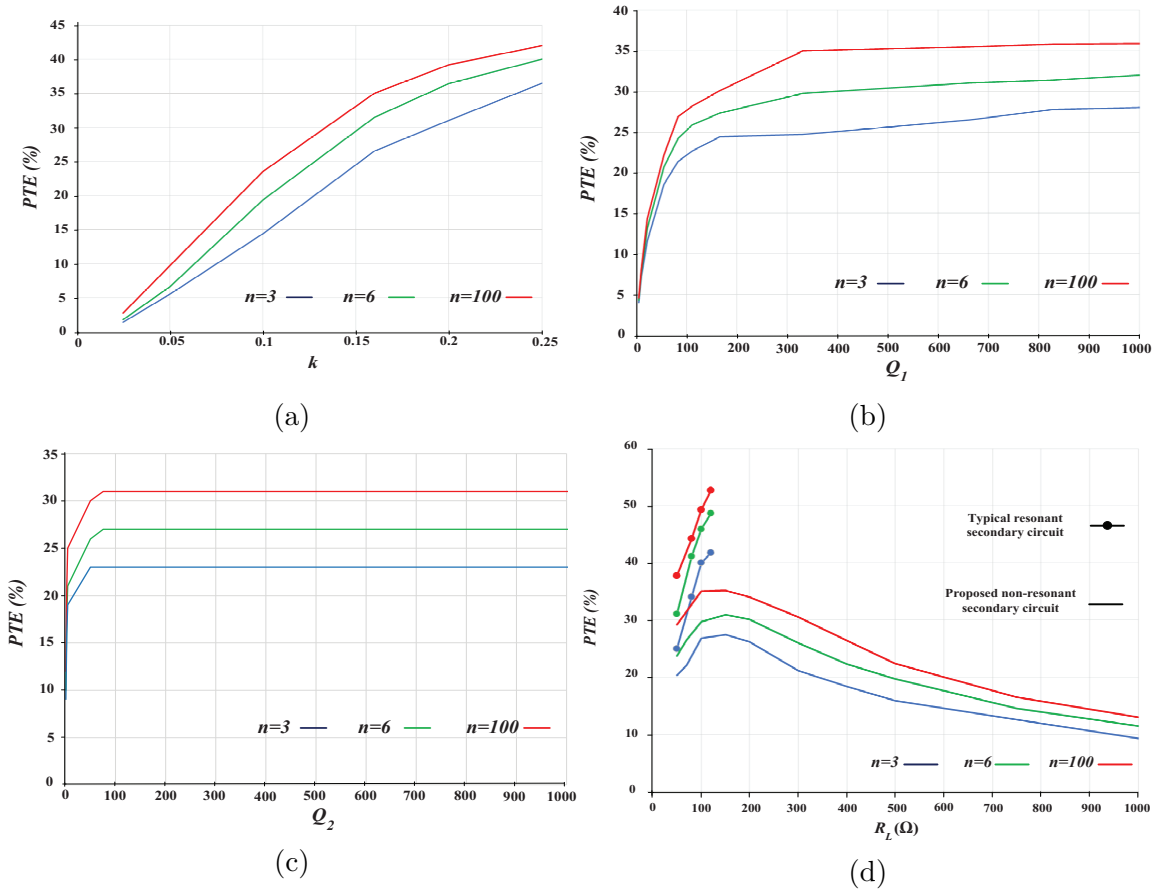

Figure 5.8 Simulated PTE as a function of (a) k, (b) Q_1,(c) Q_2 and (d) R_L, for different n.

5.4 SYSTEM IMPLEMENTATION

Figure 5.9 illustrates a simplified schematic of the proposed wireless power and data transfer system consisting of a transmitter (TX) and a receiver (RX). The transmitter can be divided into four main parts: the traditional inductive power transmission circuit based on a class E PA, the CWM modulation circuit, the current zero-crossing detector, and the signal processing unit. On the other side, the receiver includes power and data recovery circuits. All these system blocks will be discussed in the following subsections. Also, the challenges faced during experimentation and the proposed solutions will be presented.

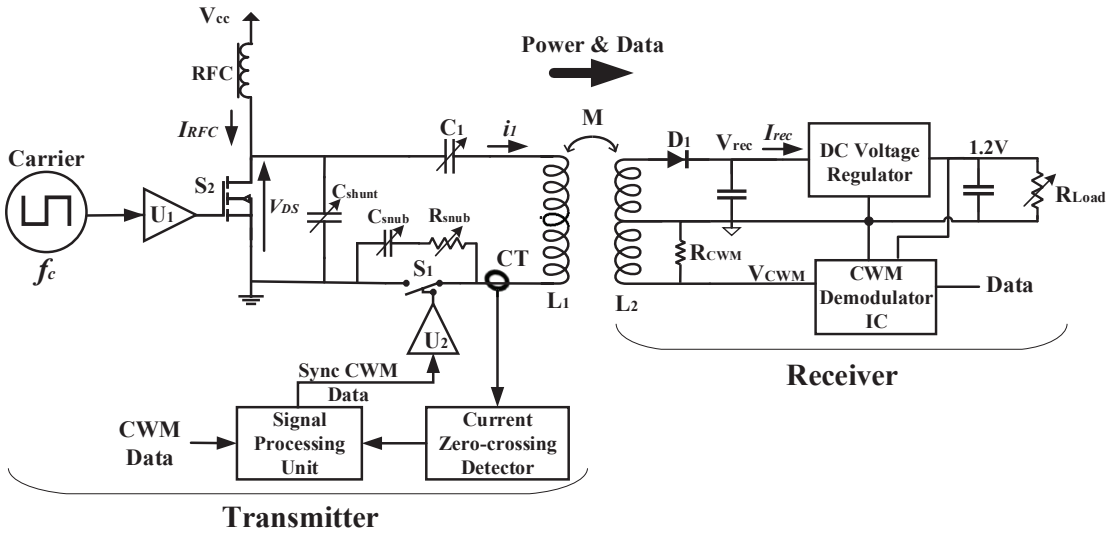

Figure 5.9 Block diagram of the implemented system for power and data transfer

5.4.1 Class E Power Amplifier

The class E PA consists of a transistor S_2, an RF choke RFC, a shunt capacitor C_{shunt} and an LC series tank matching network formed by a primary coil L_1 and a series capacitor C_1. The transistor S_2 acts as a switch (i.e. operating between triode and cut off regions) and it is turned On and Off periodically at the carrier frequency f_c. C_{shunt} that includes the intrinsic output capacitance of the transistor is mainly used as an alternative current pathway when the switch is off in order to reduce power dissipation in the transistor. The L_1-C_1 resonant circuit is tuned to the first harmonic of the carrier frequency and acts as a filter that allows only a clean sinusoidal current to pass across it.

When S_2 is off, it acts as an open circuit that allows I_{RFC} to charge up C_{shunt} and increase V_{DS}. The rising voltage will excite the series resonant LC tank circuit causing AC current to flow in L_1 at the operating frequency. Due to this resonant circuit, V_{DS} eventually drops before the transistor is switched on again. When S_2 is On, the transistor channel has a low-resistance and any charge stored on C_{shunt} will be discharged to the ground, so the voltage V_{DS} is pulled near zero and a large current flows through S_2.

In theory, if the transition times between the On and Off states and the Drain-Source On-resistance R_{DS}(on) are negligible, the efficiency of a class E PA is 100%. However, in practice, these parameters are not negligible and the amplifier's efficiency depends on the ability of the transistor to hold zero charge across its terminals while it is switching, and to perform On/Off switching transitions as fast as feasible. The time required to switch On a MOSFET

depends on the time it takes to inject the Gate-to-Source charge Q_{gs} and the Gate-to-Drain charge Q_{gd} into the gate.

Due to its ultra-low Q_{gs} and Q_{gd} parameters, the EPC2038 transistor, from Efficient Power Conversion Corporation's (EPC), was selected to build the prototype reported later. It is a Gallium nitride (GaN) power transistor that behaves similarly to a silicon (Si) transistor, but it has superior performance. Indeed, compared to conventional Si technologies, GaN transistors are much faster while having lower on-resistance, higher Drain-Source breakdown voltage, less parasitic capacitance and zero reverse recovery charge. Thus, they yield less conductance losses, switching losses and gate drive losses. Since their first introduction in 2010, GaN devices attracted attention in scientific communities over the past 10 years especially in high-frequency [164], high-power [165], and high-temperature [166] applications, due to their reliability, small size and cost effectiveness.

To drive the GaN transistor at high switching frequency, a gate driver circuit U_1 must be used to provide a high-current level during a very short duration. The ultra-fast gate driver UCC27611 from Texas Instruments has been employed. Its high output current and fast rise/fall time are adequate to efficiently drive the GaN transistor. Both EPC2038 and UCC27611 are tiny and have compact packages, thus mitigating the effects of parasitic inductances. In fact, when driving power devices at high frequency, a low inductance helps achieve high current and low gate ringing.

5.4.2 CWM modulation circuit

Due to their superior performance, EPC2038 and UCC27611 are also used to switch On and Off the LC primary circuit for CWM data modulation. However, special considerations must be taken when switching an inductive load. Switching Off the transistor at zero-crossing of i_1 allows theoretically to cancel the current in the primary coil. However, due to high speed switching, a small amount of transient current may flow into the coil. Moreover, when turning Off the switch S_1, the magnetic energy stored in the parasitic inductances may produce an excessive voltage across the power device that can be destructive. Parasitic inductances may come from the printed circuit board (PCB) routes [167], components leads [168], or by reflected reactance from the secondary circuit, especially at strong coupling [50, 151].

Parasitic inductances combined with existing capacitances form a resonant tank that may lead to transient oscillations of S_1 drain source voltage and primary current, right after the device switching Off, as shown by the blue waveforms in Fig. 5.10. Existing capacitances include the intrinsic output capacitance of S_1 and S_2, C_{shunt}, and the stray capacitance due to PCB layout and mounting. Note that L_1 and C_1 reactances are canceling each other since

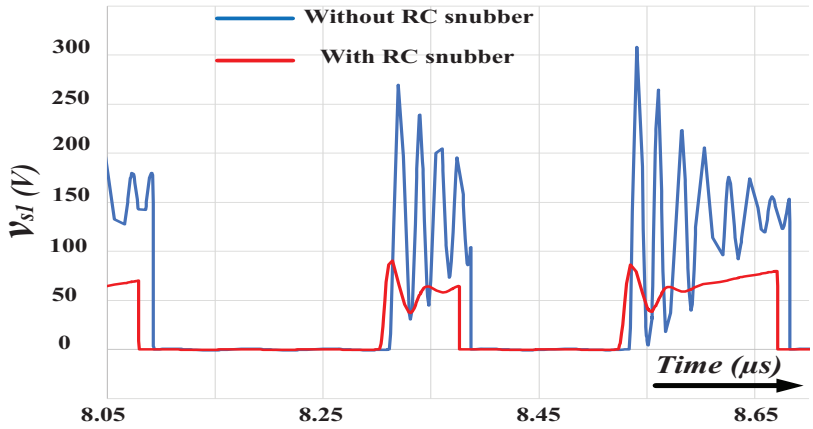

(a)

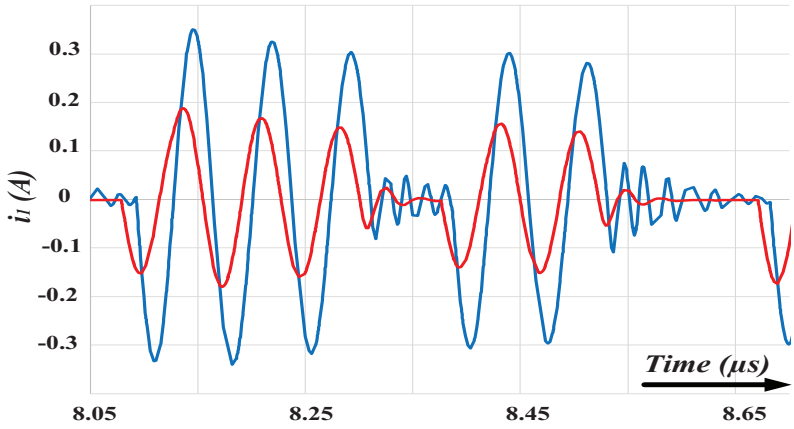

(b)

Figure 5.10 Switching S_1 Off transient performance with and without RC snubber when using a non-ideal switch.(a) S_1 drain-source voltage V_{s1}, and (b) primary coil current i_1

the LC tank is set at resonance.

In order to significantly reduce the observed parasitic oscillations, an energy-absorbing circuit called RC snubber is placed across the switch S_1, as shown in Fig. 5.9. It reduces the transient oscillation by providing an alternate path for the current flowing through the parasitic inductances, therefore damping the subsequent current and voltage oscillations, as shown by the red waveforms in Fig. 5.10.

Adjustable R_{snub} and C_{snub} were used and a fine-tuning of these parameters was performed using trial and error experiments to damp and reduce as much as possible the ringing effect. The fine-tuning of C_{shunt} was also useful to damp the ringing. This empirical method remains the most commonly used approach for designing damping components [169, 170].

At the end, the damping of the voltage and current parasitic oscillations is obtained at the cost of power dissipation in the resistor R_{snub}, estimated as [171]:

$$P_{diss} = C_{snub} V_{pk}^2 f_s \tag{5.5}$$

where V_{pk} is the reduced peak amplitude across S_1 and f_s is the switching frequency.

Aiming at reducing the power dissipation in the resistor R_{snub} together with other undesirable behaviors; including overshoots, EMI, and oscillations in the gate drive voltage (which may turn the device On and Off accidentally) a relatively low switching frequency should be selected. Therefore, 10 MHz carrier frequency has been adopted, since it is the lowest frequency in the operating range of our proposed generic-CWM demodulator [82].

5.4.3 Current zero-crossing Detector

A toroidal current transformer (CT) is used to sense the zero-crossing of the primary coil current i_1. When the AC current i_1 flows through the CT primary winding, a magnetic field is produced in the toroid core, which induces a proportional AC current i_2 in the CT secondary winding. A resistive load, usually defined as the "burden resistor", is connected to the secondary winding in order to produce a proportional voltage signal. In an ideal current transformer, i_1 and i_2 are in antiphase and their intensity relationship is given by

$$i_2 = \frac{1}{N_2} i_1 \tag{5.6}$$

However, in reality, a part of i_1 is consumed by the core and the relation between i_1 and i_2 will be :

$$i_2 = \frac{1}{N_2} i_1 - i_e \tag{5.7}$$

where i_e is the excitation current absorbed by the core, which is able to induce a phase shift between i_1 and i_2. This phase shift error may increase due to external magnetic fields or stray inductances and capacitances generated by the ferromagnetic core, the burden resistor and PCB traces. In order to reduce as much as possible the excitation current and the subsequent phase shift error, low loss CT core with low reluctance should be used. A ring type core is selected to take advantage of its very small reluctance and leakage reactance. Also, it is very important to keep the burden resistance low to reduce the influence of the excitation current i_e on i_2 and to avoid a severe saturation of the core. However, this decreases the voltage across R_b. The selection of the number of turns in the secondary N_2 and the burden

resistance R_b was made according to a tradeoff between having a low excitation current and a sufficiently high V_b voltage.

5.4.4 Signal processing unit

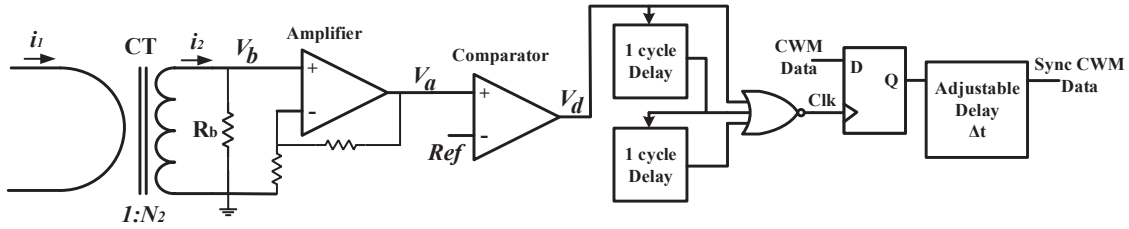

Figure 5.11 Circuit diagram for the current zero-crossing detection and CWM synchronized data generation

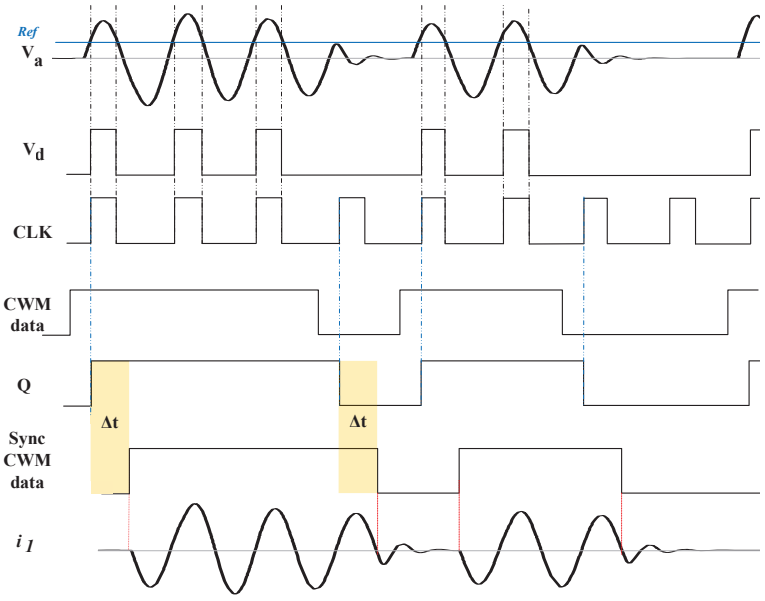

Figure 5.12 Timing diagram of CWM data synchronization

Figure 5.11 shows the schematic of the signal processing unit aiming to synchronize the S_1 switching with the i_1 signal zero crossing. First, a high-speed voltage amplifier with a gain of 10 and a unity-gain bandwidth of 200 MHz is used to amplify V_b. This amplifier also operates as a low-pass filter with a cutoff frequency of 20 MHz. Then, the amplified voltage V_a is digitized by comparing it with a reference set to a voltage slightly higher than the associated undesirable noise ripples of V_a, as shown in Fig. 5.12. The digital signal V_d is then used as a clock signal synchronized with the zero-crossing timing. However, the LC tank opening for

data transmission leads to blanked sinewaves. In order to produce a regular clock signal, two full-period delay lines and an NOR gate were used to establish a time-shift circuit, as shown in Fig. 5.11. This time-shift circuit is implemented using two DS1023 configurable timing elements, from Maxim integrated and the 3-input NOR gate SN74LVC1G27, from Texas Instruments. The resulting output signal CLK is afterward introduced to a D Flip-Flop module to synchronize the CWM-encoded data. Finally, another delay element is added to compensate the total propagation delay Δt produced by upstream components and generate a CWM-encoded data synchronized with the i_1 zero-crossing.

5.4.5 Power and data recovery

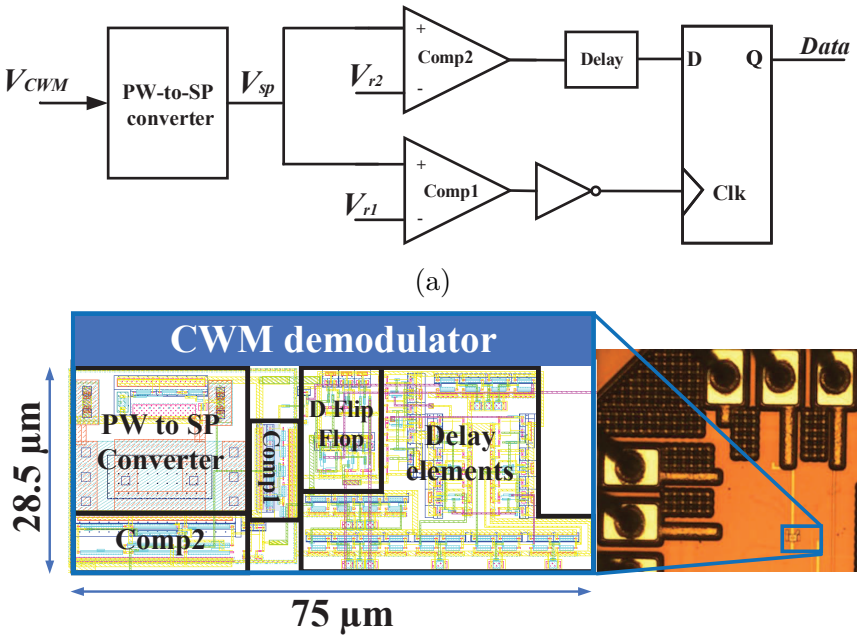

Figure 5.13 (a) Block diagram of the proposed CWM demodulator, and (b) Chip micrograph

Inductively transmitted power and data are recovered using the previously reported non-resonant secondary circuit. A common power-recovery stage was built using a half-wave rectifier followed by low-dropout (LDO) voltage regulator. The latter generates 1.2 V DC voltage in order to supply the resistive load R_{Load} and the CWM demodulator chip. For data recovery, a 70 Ω resistor R_{CWM} is placed in parallel with L_{2d} to damp unwanted oscillations in V_{CWM} (Fig. 5.9). This modulated signal is then introduced to our proposed generic-CWM demodulator which was the topic of our previous papers [15, 82].

In essence, the demodulator is based on a pulsewidth to sawtooth peak converter designed to

convert the Off periods to a sawtooth signal, for which the peak value depends only on the Off duration. As shown in Fig. 5.13a, only two additional comparators and a digital block (including delay cells, an inverter and a D flip-flop) are then used for synchronization and data recovery. The voltage references V_{r1} and V_{r2} are implemented using external resistive dividers. Compared with state-of-the-art demodulators used for inductive forward data transmission, the proposed demodulator offers a distinctive performance in terms of high speed, low-energy efficiency as demonstrated in [15, 82]. Moreover, the chip micrograph of our demodulator occupies a small silicon area as shown in Fig. 5.13b.

5.5 Experimental Results

Figure 5.14 shows the experimental test bench. The proposed WPDT system was mounted on two PCBs (one for the transmitter and one for the receiver). The transmitter prototype was implemented using Commercial Off-The-Shelf (COTS) components on a PCB area of $113 \times 77\ mm^2$. It is powered by one DC power supply and three DC-DC converters. To experimentally validate the functionality of our proposed WPDT system for a wide data rates range, a Keysight Benchlink waveform builder software and a 33622A Function/ Arbitrary Waveform Generator were used to produce CWM-encoded data for different n.

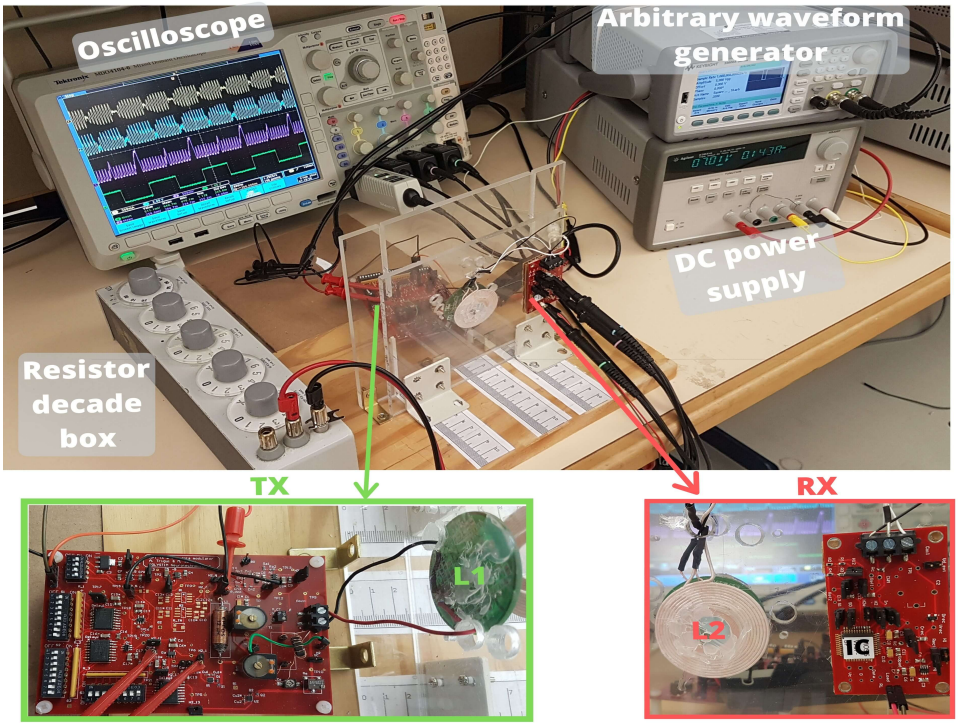

Figure 5.14 Photographs of the experimental setup.

Table 5.1 Parameters of the inductive link

Carrier frequency	10 MHz
Primary coil	3-turn spiral coil printed on PCB
	43 mm diameter, 1 mm trace width
L_1	0.7 μH
r_{L1}	273 $m\Omega$
Q_1	161
Secondary sub-coil	8-turn spiral coil litz wire,
for power recovery	43 mm diameter, 1 mm wire thickness
L_{2p}	2.4 μH
r_{L2p}	138 $m\Omega$
Q_{2p}	1092
Secondary sub-coil	8-turn spiral coil Litz wire,
for data recovery	23 mm diameter, 0.5 mm wire thickness
L_{2d}	1 μH
r_{L2d}	125 $m\Omega$
Q_{2d}	502

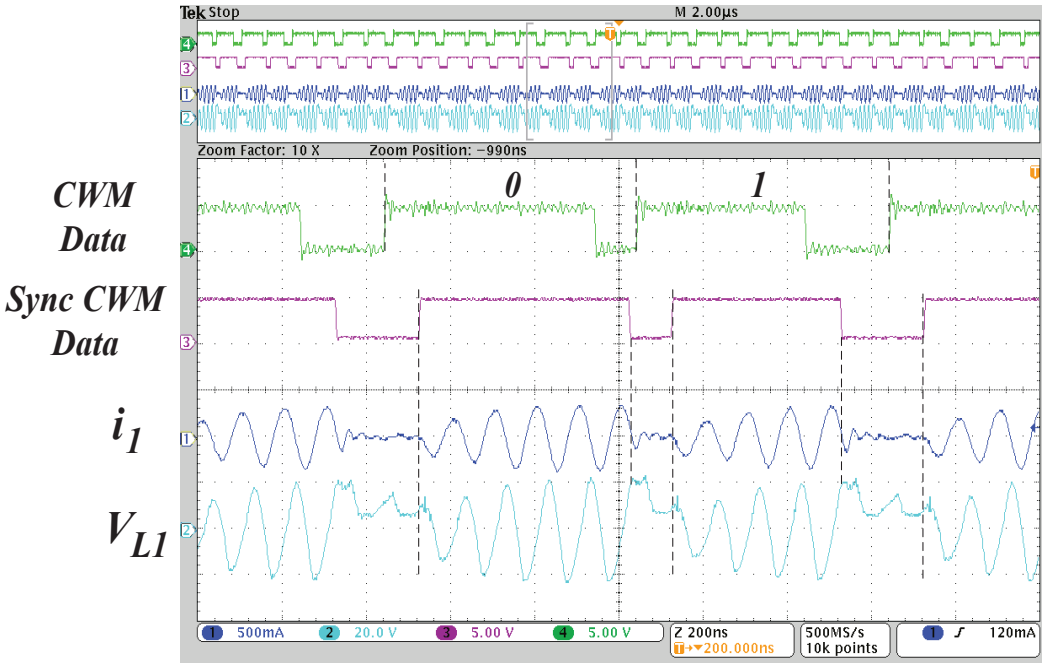

Figure 5.15 Measured waveforms for CWM data modulation in the transmitter with n=6.

The receiver prototype is based on a demodulator IC; fabricated with 0.13 μm CMOS technology; as well as COTS components for the remaining parts. The CWM demodulator IC occupies an ultra-small silicon area of 75 $\times$ 28.5 μm^2 and the receiver PCB has an area of 65 $\times$ 37 mm^2. A resistor decade box was employed as a secondary load R_L to study the impact of load variation on the system performance. Voltage and current waveforms were recorded using a digital oscilloscope (MDO4104-6 from Tektronix). A multimeter was used to measure the DC output current of the rectifier (not shown in Fig 5.14). All measurement graphs presented in this section were taken when both power and data transfer were secured.

In this experimental setup, the chosen geometries and parameters of the primary and secondary coils are shown in Table 5.1. For efficient power transfer, the primary and secondary coils Q factors were chosen higher than 100. However, a much higher primary Q factor may affect the system functionality. In fact, Q_1 is limited by the coil inductance that should be relatively low in order to make the tuning of C_1 less critical and more accurate to reach a resonance state [172].

Figure 5.15 shows the measured CWM-encoded data before and after synchronization performed by the current zero-crossing detector and the signal processing unit. It shows that our proposed CWM modulator allows an accurate switching timing of the primary LC tank. As can be noticed in this screenshot, the LC tank opening is performed at zero-crossing of i_1. This corresponds to a switching when the primary coil voltage V_{L1} is at an extremum and all the energy of the primary LC circuit is stored on C_1.

Figures 5.16a and 5.16b show the measured primary current and secondary voltage waveforms during data transmission. It can be seen that despite the high Q factors of coils and the ringing effect due to S_1 switching and to stray capacitances in the secondary circuit, our proposed WPDT system was able to produce modulated signals (i_1 and V_{CWM}) with highly damped oscillations during Off periods. This allowed our demodulator circuit to perfectly demodulate the received signal V_{CWM} using the proposed CWM demodulator IC.

Figure 5.16a shows the measured waveforms for a repeated data bit stream of "010011" at a data rate of 1.66 Mb/s. However, Fig. 5.16b shows the measured waveforms when a reapeted pattern sequence of "01" is sent at maximal data rates of 3.33 Mb/s. These screenshot captures validate that the data transmission is robust for recurring pattern in the bit stream as well as for high data rates.

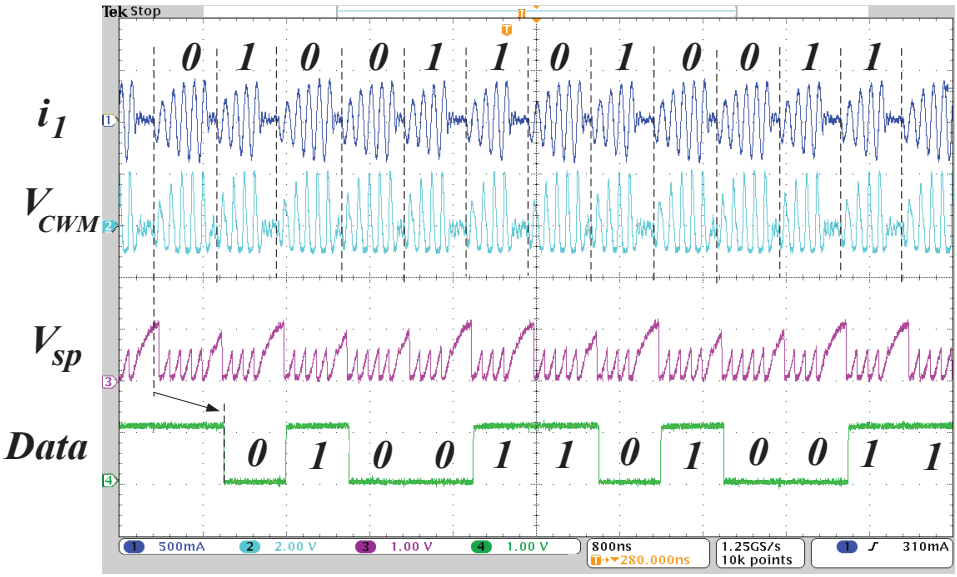

(a)

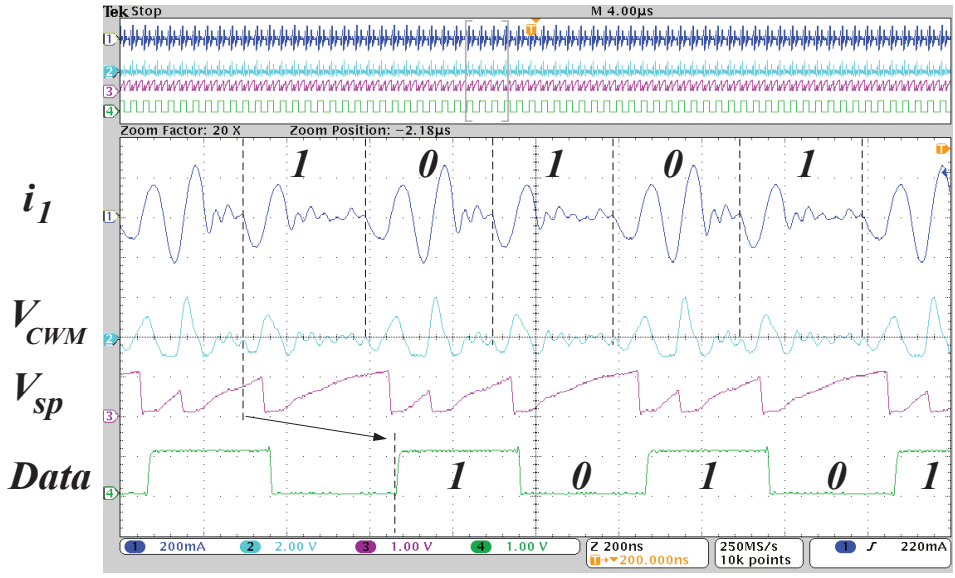

(b)

Figure 5.16 Measured waveforms for data transmission and reception for (a) n=6 with a repeating "010011" bit sequence, (b) n=3 with repeating "01" pattern sequence. The output digital bit-streams are delayed by $\Delta t + T_d$ [15].

Figure 5.17a illustrates the effect of the load (R_L) variation on recovered power P_{DL} at axial distance d_a between primary and secondary coil of 1 cm for different data rates with P_{DL}=V_{rec}×I_{rec} where V_{rec} and I_{rec} are the output voltage and current of the rectifier, respectively. We notice that for each carrier cycle per bit n (data rate), there is an optimum load that maximizes the power delivery. Note that this optimum is found very close to the edge of the region beyond which communication stops working.

Figure 5.17b shows the maximal achievable recovered power $P_{DL_{max}}$ as a function of data rates at d_a=1 cm. As expected, $P_{DL_{max}}$ increases with n. However, the best tradeoff is represented by a Figure of Merit value (FoM) defined as FoM = Data rates×$P_{DL_{max}}$. The best FoM (49.23) is reached at 1.66 Mb/s ($n = 6$).

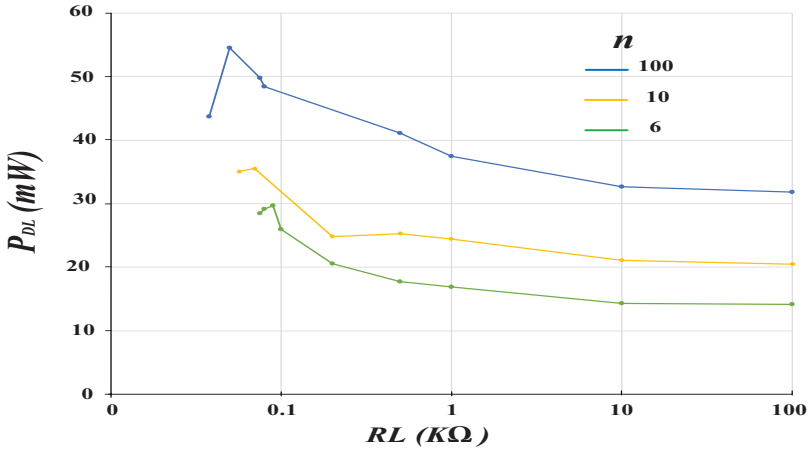

(a)

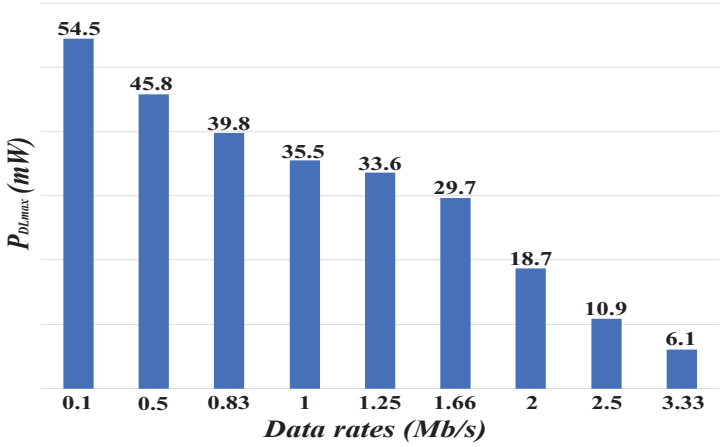

(b)

Figure 5.17 Measured recovered power at 1 cm axial distance: (a) P_{DL} as a function of R_L; (b) Maximum P_{DL} as a function of data rates.

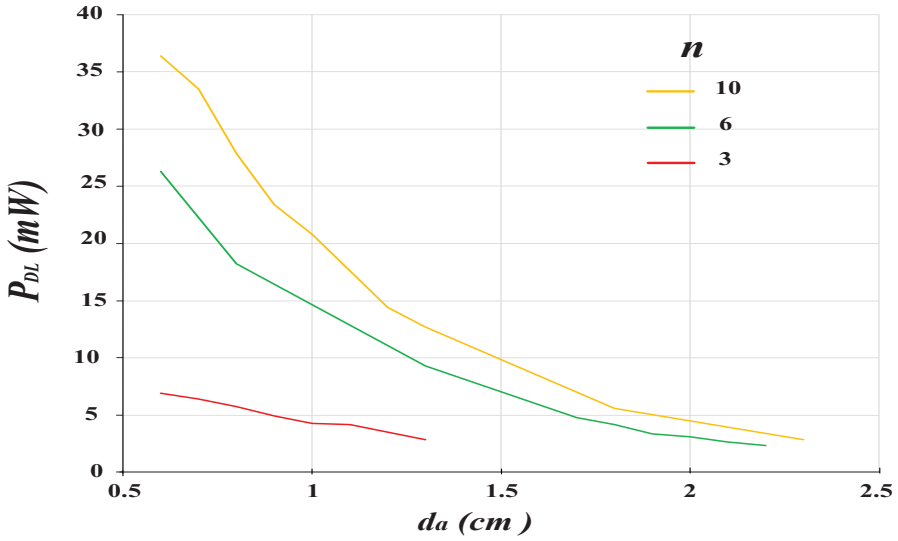

Figure 5.18 P_{DL} as a function of axial distance between coils at R_L=1 $K\Omega$.

Figure 5.18 shows the effect of axial distance d_a variation on recovered power P_{DL} for different data rates with R_L=1 $k\Omega$. We can notice that P_{DL} decreases as coil separation grows. This P_{DL} reduction is due to the reduction in mutual inductance which is inversely proportional to d_a. Also, as expected, the distance range decreases while decreasing n, since at higher d_a, not enough power can be recovered to supply the receiver. At stronger coupling ($d_a \leq 0.6$ cm), the modulation process will be disturbed due to the high reflected reactance from the secondary circuit, as mentioned in Section 5.4.2

Table 5.2 compares the proposed CWM-based WPDT system (for n = 6) with state-of-the-art WPDT systems based on ASK modulation. As expected, conventional ASK systems have relatively low data rates. Our system excels in data rates while ensuring a relatively high recovered power P_{DL}. It provides a FoM approximately 5 times higher than the closest ASK competitor [173]. Furthermore, our demodulator IC consumes only 17 μW at highest data rates (3.33 Mb/s) which results in 5.1 pJ/bit energy consumption. [82]. These excellent performances are added to the genericity of our system that makes it convenient for a wide range of applications.

5.6 Conclusion

This paper presented a new modulation scheme for both wireless power and data delivery for medical implants over a single inductive link. The prototypes implementation was detailed and experimental measurements were performed. Unlike conventional WPDT systems op-

Table 5.2 Performance comparison of inductive power and downlink data transfer systems

Reference	TBioCAS'15 [74]*	BMEL'13 [75]	JSSC'17 [173]*	JSSC'19 [174]	**This work**
Modulation scheme	ASK	PWM ASK	PWM OOK	ASK	**CWM**
f_c (MHz)	10	5	6.78	13.56	**10**
Data rate (Mbit/s)	0.1	0.168	0.02	0.15	**1.66**
Min Carrier Cycle per bit	100	29.76	339	90.4	**3**
Maximum P_{DL} (mW)	10	13	520	9.2	**29.66**
Data Rx power consumption (μW)	NA	NA	NA	132	**14.6**
RX energy efficiency (pJ/bit)	NA	NA	NA	880	**8.79**
FoM	1	2.18	10.4	1.38	**49.23**

* The system offers a bidirectional communication.

erating at high-Q coils, the proposed system based on CWM modulation allows high-speed communication while ensuring a convenient power delivery to the biomedical implant. This performance is achieved by overcoming two main limitations, one related to the conflicting Q factor requirements for high-power delivery and high data rates and the other is related to the limited speed of conventional demodulator circuits. Moreover, our CWM-based system is generic and can achieve a wide range of data rates for a maximum of 1/3 of the carrier frequency. Comparisons with related works show that our WPDT system offers the best tradeoff between data rates and delivered power over a single inductive link using an ultra-low power and generic CWM demodulator.

Acknowledgments

The authors would like to thank CMC Microsystems for providing access to design and implementation tools.

CHAPTER 6 GENERAL DISCUSSION

The motivation of this thesis was to improve the performance of wireless power and data transfer systems for IMDs in all respects, including the size and the ease of implementation, the data communication reliability and speed, the power transfer efficiency, and the power consumption of the implantable device, while aiming at getting a flexible and generic system that can cover a wide range of IMD applications.

This goal is very ambitious and while advancing in the investigation and in the literature review, we realize the great complexity of the task. Several reasons make this task a priori impossible. Among these reasons, fundamental problems of physics such as the inversely proportional relation of the Q factor with the bandwidth or the ringing phenomenon due to high-Q LC circuit. Circuit limitations of conventional blocks such as the envelope detector, or technological limitations, such as CMOS analog switch speed limit at high drain current have also made our goal harder to achieve. All these limitations have been addressed in a methodical ways and we have successfully proposed a more efficient power and data transfer system compared to state-of-the-art systems.

We adopted early on the inductive link among several wireless technologies such as RF, capacitive, ultrasonic, and optical links, mainly due to its ability to provide both power and bidirectional data transmission with appropriate reliability, safety, cost, and simplicity of implementation. Besides, the inductive link was the most popular technique in commercially available IMDs either for recharging internal batteries or for directly providing power to the IMD.

Then, between choosing a configuration of multiple dedicated links for power and for data or a single inductive link approach optimized for the two functions, we chose the most difficult approach, in order to achieve a less cumbersome implementation and to seek for potential benefits on human safety and comfort. In fact, the use of a single inductive link instead of multiple links for wireless power and data transfer reduces the size of the implant and alleviate design constraints on biological and physical aspects. It also reduces human exposure to electromagnetic fields and disturbances that can affect the functionality of the implant due to electromagnetic interference.

The following step was to select the appropriate modulation technique for downlink communication. A comprehensive survey of existing modulation techniques was carried out. Investigating the advantages and disadvantages of these techniques, the choice was made on ASK modulation more specifically on OOK modulation coded in PWM due to its lower

power consumption and design complexity, since it does not need complex synchronization circuitry for data recovery. However, this modulation is based on amplitude variation of the carrier, so any amplitude disturbances due to noise, interference, or coupling variation may affect considerably the communication reliability. Hence, we had the idea of using a similar modulation scheme but whose demodulation process would be based on the carrier width instead of the amplitude. Therefore, we initially proposed Quad-level Carrier Width Modulation (QCWM) that consist of sending two bits per symbol by using four combinations of duty ratio. Aiming toward high data rates communication, we choose the ISM high carrier frequency 27.12 MHz that belongs to the widely used frequency range in transcutaneous wireless transmission (3kHz to 30MHz). This frequency range allows the electromagnetic field to penetrate the skin over a short distance, without heating the surrounding biological tissues. A QCWM demodulator was proposed, designed using a 0.13 µm CMOS process and validated by simulation. The novelty of this demodulator is the use of an original pulse width to sawtooth waveform (PW-to-SP) converter. This simple to implement converter allowed the whole QCWM demodulator to achieve an ultra-low power consumption of 35.5 µW at 10.85 Mbps data rate.

Based on PW-to-SP converter, another new CWM modulation scheme with carefully chosen ON/OFF duration was proposed to reach a generic high-performance data communication system. The proposed CWM demodulator was initially designed to operate at 27.12 MHz then customized to operate at a frequency range between 10 and 31 MHz, while offering an ultra-low power consumption. This generic demodulator offers a data-rate-to-frequency ratio of 1/3 and dissipate, in worst conditions, 16.9 µW.

In addition to the implementation of the demodulator, our efforts also focused on the development of the modulator and the complete power and data transfer system. This was the most difficult task, since no similar work aimed at simultaneous high power transfer efficiency and high data rates on a single inductive link was carried out, with the exception of suspended carrier modulation patented in 1997. However, there is little information on the design and performance of its proposed modulation circuit. Also, this work has never been developed or reproduced by other research groups for more than 20 years, which leaves several question marks about its feasisilbility and practicality.

To the best of our knowledge, we are the only research group that reused this work. Despite the lack of technical information, we managed to achieve a subsystem transmitting power and high-speed data using a high-Q resonator. The design of the modulator required a lot of simulation work using OrCAD Pspice Designer A/D software; which was not reported in this thesis. The use of a high carrier frequency and simulation convergence failure have com-

plicated the development of this solution. Hence, to reduce the complexity of the simulation, ideal components were used at the beginning, which was a good starting point towards a real design.

High frequency switching of an inductive load with the presence of intrinsic parasitic elements leads to undesirable behaviors, such as transient oscillations in the modulated signal, overshoots, EMI, and oscillations in the gate drive voltage (which may turn the switch On and Off accidentally). In order to reduce these undesirable behaviors, we migrated to a new transistor technology which is Gallium Nitride (GaN) technology. GaN devices are inherently gaining popularity in the market due to its high switching speed and very low parasitic elements. One of the reasons that greatly reduces parasitic elements of GaN devices is their ultra-small and compact package (0.9 mm $\times$ 0.9 mm, BGA), which makes soldering of these transistors very challenging. Fortunately, hot air BGA rework station was at our disposal.

Despite the use of GaN devices, the undesirable behaviors were not totally eliminated, so we reduced the carrier frequency to 10 MHz and we placed a damping circuit (RC snubber) in parallel with the GaN switch. The difficulty of implementing this circuit lies in the fact that it is based on an empirical study.

After several improvements and prototyping, we managed to implement a reliable high-Q transmitter for powering and high-speed modulation. In the receiver side, we were unable to use a secondary resonant circuit for a wide range of load. In fact, the energy stored in the secondary resonator circulates back and forth between the electric and magnetic fields and results in unwanted oscillations, which can be damped only by using very low resistance load values. To overcome this issue, a non-resonant secondary circuit with no capacitors was used. However, in practice, parasitic capacitances such as the internal capacitance of the secondary coil and the junction capacitance of the diode (used for rectification) can induce the unwanted oscillations. That is why a tapped coil configuration that split the secondary coil into two sub-coils dedicated to power and data recovery was used. In addition, a low value resistance was connected to the data sub-coil in order to damp any potential oscillations during Off periods. This configuration ensured powering data communication for a large load range. Although a non-resonant secondary circuit was used, power transfer was ensured with an adequate delivered power due to the use of high-Q coils and a resonant circuit on the transmitter side.

Another important element, which must be considered during the tests is the probe measurement. The use of a long ground wire probe introduces unwanted inductance into the probe measurement path and results in overshoot and ringing associated with the rising and falling edges of the signals. Therefore, for accurate measurement results, a scope probe with a short

ground clip was mandatory. This general discussion shows that beyond the original concepts and theory proposed to explain the system operation, there are many practical issues that can spoil the expected performance.

CHAPTER 7 CONCLUSION

7.1 Summary of Works

In this thesis, we presented our research work aimed at implementing a novel wireless power and downlink data transfer system over a single inductive link, able to overcome the limitations of existing WPDT systems. First, we assessed the limitations of the conventional ASK modulation since it is the most commonly used approach due to its easy implementation and low power consumption of its demodulation circuit compared to other methods. The weakness of this approach can be summarized as follows: 1. the high sensitivity to noise and all kinds of disturbances that may affect the carrier amplitude and 2. the limited data rates due to the conflicting requirements of the coils Q factors that should be high to achieve efficient power transfer and low to achieve high bandwidth as well as 3. the limited speed of the conventional ASK demodulators.

These limitations were solved one by one, in order to propose a sophisticated WPDT system that ensures a high data rate downlink communication with efficient power transfer, while maintaining a low power consumption and a small and simple implementation of the implantable device. Another objective which has been added is to implement a generic system operating under a wide range of data rates. So, the operator can select the best compromise between power and data rates in accordance to application or current needs, without reconfiguring the receiver.

In total, we have achieved four main contributions. **First**, we proposed novel modulation techniques based on the carrier width called Carrier Width Modulation (CWM) and Quad-level CWM. They are characterized by their short Off-widths and modulation timing. In fact, they are performed at a specific time which is the zero-crossing of the primary coil current. Using this technique, efficient PTE and high-modulation bandwidth could be secured at the same time. Also, since the carrier is time modulated, the modulated signal showed a high robustness against amplitude disturbances. **Secondly**, we implemented high speed and ultra-low power demodulators ICs using 0.13 μm CMOS technology. They consume, in worst conditions, 16.9 and 35.5 μW and reach data rates of 1/3 and 2/5 of the carrier frequency, respectively. These very competitive performances are due to the use of an original PW-to-SP converter instead of the widely used envelope detector. **Thirdly**, we designed the CWM demodulator to be generic while operating over a wide range of frequencies (from 10 to 31 MHz) and many data rates under any selected frequency selected from the operating range. **Lastly**, we implemented a 10 MHz high-Q transmitter that generates signals modulated at

high rates, despite the use of high-Q coils. This proposed transmitter is the first of its kind that operates at high frequency and that meets all design and implementation challenges, especially when operating at a high frequency of 10 MHz. In combination with the proposed CWM demodulator, simultaneous 3.33 Mb/s data rates and 6.1 mW recovered power are achieved at 1 cm separation distance between the coils. Due to our WPDT system genericity, the system may also transfer more than 55 mW, at the expense of reduced data rates.

According to the state-of-the-art modulation techniques, our proposed WPDT system is the best technique if there is a need to maximize the data rate for downlink communication, when a single inductive link is used for both power and data transmission and when simplicity and ultra-low power consumption receiver are required.

7.2 Recommendations for future work

Based on research presented in this thesis, we propose some recommendations and ideas for future work to address some limitations of our proposed system, to enhance its performance, or to further improve performances. These recommendations are divided according to the location where improvements can be made.

In the transmitter:

1) As this is the first time that a synchronized opening of the resonant LC transmitter circuit has been made, our main objective was to validate its functionality without paying much attention to the performance of the modulator. Hence, the CWM modulator was implemented using available COTS products. As future work, an integrated and custom modulation circuit might be implemented. This might reduce modulation errors since accurate delay elements can be designed with much reduced values of parasitic elements that limit performances. It is also expected that a modulator IC would allow reducing power consumption and physical dimensions.

2) We realized in this project that a high carrier frequency leads to high sensitivity to parasitic elements, low BER, and high switching power dissipation. Such limitations could be avoided in the future if a similar WPDT system is designed to operate at lower carrier frequency (i.e. at 6.78 MHz ISM band). This would certainly decrease the data transfer rate. However, it could improve the transmitter power efficiency and the BER. This is an interesting avenue for future research.

3) As a QCWM demodulator is already fabricated and tested, it remains to design and implement a high-Q transmitted based on QCWM scheme. Compared to the CWM

transmitter, a QCWM transmitter will have a different encoding algorithm and a new signal processing unit since it contains four distinct Off periods instead of two. This WPDT system will offer a higher data rate than that offered by CWM-based WPDT system.

In the inductive link:

1) Although high-Q coils were used to increase the power transfer efficiency of the inductive link, the following recommendations should allow improving the PTE:

    a) Explore other coil geometries, e.g. the best shape, dimensions, number of turns, resistance loss, and Q factor of the two coils. The optimal coil geometries can be found using closed-form equations in MATLAB in combination with HFSS or COMSOL Multiphysics software.

    b) Implement a custom integrated voltage rectifier and voltage regulator in order to increase the power efficiency of the inductive link, since it is a function of the input impedance of the rectifier. Also, a fully-integrated power recovery stage may decrease the power dissipation in the receiver and allow miniaturizing the IMD.

2) As already mentioned, the sensitivity of the inductive link to the relative position of Tx and Rx is among the main challenges of this technology. In fact, at strong coupling (i.e. short distance) between coils, the reflected impedance to the primary circuit becomes large, so it alters its resonant frequency. Thus, this decreases the PTE significantly, and it disturbs the CWM modulation process in the transmitter. To overcome this issue, an adaptive system trying to compensate this alteration can be envisaged.

In the receiver:

1) In the actual design, the peak amplitude of the output sawtooth signal depends strongly on the supply voltage, so any variation of this DC voltage can disturb the communication. The robustness against the supply voltage variations defined by the Power Supply Rejection Ratio (PSRR) can be improved by adding an additional circuit, such as current mirrors, to our PW-to-SP converter.

2) A more generic CWM demodulator can be implemented by adding two adjustable voltage reference circuits. The voltage references can be set automatically by sending a request to the receiver to readjust the voltage reference levels according to the carrier

frequency used. However, this probably requires the use of a microcontroller in the receiver.

3) Achieving the maximum power transfer and the highest data rates was our main objective when we started this PhD project. Although we managed to get very high data rates, we were unable to increse the PTE as much as desired. The maximum PTE can be achieved when the secondary circuit is also resonating at the same frequency as the carrier and the primary resonant circuit. However, this was not possible because the presence of capacitors in the secondary circuit that led to a ringing effect that limits the data transmission rate. Performing a resonant secondary circuit that offers better power transfer and does not limit the data rates can be an interesting and original research direction.

4) For a complete remote power and data transfer system, an uplink communication system may be added to our system. In the same vein, we recommend implementing a synchronized shorting of the secondary LC circuit in order to preserve the energy in the secondary tank without compromising the power efficiency as in the recently proposed COOK modulation. Since this kind of modulation technique, whether in downlink or uplink data transmission, is newly investigated, it can be a good niche for further research.

Another idea that can be envisaged is to realize a WPDT system that automatically adjusts transmission speed and the delivered amount of power according to the IMD needs. In fact, there are implants that require, at some point, more power than data or vice versa. Self adjusting IMD systems may lead to better WPDT systems.

Finally, in order to test the reliability of the proposed data communication system, a bit-error testing and a jitter analysis should be conducted. An FPGA-based tester may be used to compare the transmitted and the received data. Unfortunately, constraints beyond our control prevented us from carrying out these tests before submitting this thesis.

PUBLICATIONS

We list here all the publications made by the author in connection with the work of this thesis. Some of these publications are also listed in the Bibliography section in the order they are called in the thesis.

Peer-reviewed journal papers:

[I] A. Trigui, M. Ali, S. Hached, A. C. Ammari, Y. Savaria and M. Sawan, "Generic Wireless Power Transfer and Data Communication System Based on a Novel Modulation Technique ," in IEEE Transactions on Circuits and Systems I, vol. X, pp. XXX XXX, 2020. (Submitted)

[II] A. Trigui, M. Ali, A. C. Ammari, Y. Savaria and M. Sawan, "Energy Efficient Generic Demodulator for High Data Transmission Rate Over an Inductive Link for Implantable Devices," in IEEE Access, vol. 7, pp. 159379-159389, 2019.

[III] A. Trigui, S. Hached, A. C. Ammari, Y. Savaria and M. Sawan, "Maximizing Data Transmission Rate for Implantable Devices Over a Single Inductive Link: Methodological Review," in IEEE Reviews in Biomedical Engineering, vol. 12, pp. 72-87, 2019.

[IV] A. Trigui, M. Ali, A. C. Ammari, Y. Savaria and M. Sawan, "A 1.5-pJ/bit, 9.04-Mbit/s Carrier-Width Demodulator for Data Transmission Over an Inductive Link Supporting Power and Data Transfer," in IEEE Transactions on Circuits and Systems II: Express Briefs, vol. 65, no. 10, pp. 1420-1424, Oct. 2018.

Peer-reviewed conference papers:

[V] A. Trigui, M. Ali, A. C. Ammari, Y. Savaria and M. Sawan, "A 14.5 μW generic Carrier Width demodulator for telemetry-based Medical Devices," 2017 15th IEEE International New Circuits and Systems Conference (NEWCAS), Strasbourg, 2017, pp. 369-372.

[VI] A. Trigui, M. Ali, A. C. Ammari, Y. Savaria and M. Sawan, "Quad-Level Carrier Width Modulation demodulator for micro-implants," 2016 14th IEEE International New Circuits and Systems Conference (NEWCAS), Vancouver, BC, 2016, pp. 1-4.

REFERENCES

[1] W. Liu *et al.*, "Semiconductor-based implantable microsystems," *Handbook of Neuroprosthetic Methods*, vol. 6, pp. 127–161, 2003.

[2] M. Rasouli and L. S. J. Phee, "Energy sources and their development for application in medical devices," *Expert Rev. Med. Devices*, vol. 7, no. 5, pp. 693–709, 2010.

[3] H.-J. Yoo and C. van Hoof, *Bio-Medical CMOS ICs*. Springer, 2010.

[4] F. Mounaim and M. Sawan, "Toward a fully integrated neurostimulator with inductive power recovery front-end," *IEEE transactions on biomedical circuits and systems*, vol. 6, no. 4, pp. 309–318, 2012.

[5] X. Wei and J. Liu, "Power sources and electrical recharging strategies for implantable medical devices," *Front. Energy Power Eng. in China*, vol. 2, no. 1, pp. 1–13, 2008.

[6] M. R. Basar *et al.*, "Application of wireless power transmission systems in wireless capsule endoscopy: an overview," *Sensors*, vol. 14, no. 6, pp. 10 929–10 951, 2014.

[7] F.-G. Zeng *et al.*, "Cochlear implants: system design, integration, and evaluatin," *IEEE Rev. Biomed. Eng.*, vol. 1, pp. 115–142, 2008.

[8] J. D. Weiland, W. Liu, and M. S. Humayun, "Retinal prosthesis," *Annu. Rev. Biomed. Eng.*, vol. 7, pp. 361–401, 2005.

[9] M. Monge *et al.*, "A Fully Intraocular High-Density Self-Calibrating Epiretinal Prosthesis," *IEEE Trans. Biomed. Circuits Syst*, vol. 7, no. 6, pp. 747–760, 2013.

[10] N. Tran *et al.*, "A complete 256-electrode retinal prosthesis chip," *IEEE J. Solid-State Circuits*, vol. 49, no. 3, pp. 751–765, 2014.

[11] W. Liu *et al.*, "Electronic visual prosthesis," *Artif. organs*, vol. 27, no. 11, pp. 986–995, 2003.

[12] F. Goodarzy, E. S. Skafidas, and S. Gambini, "Feasibility of energy-autonomous wireless microsensors for biomedical applications: Powering and communication," *IEEE Rev. Biomed. Eng*, vol. 8, pp. 17–29, 2015.

[13] H.-M. Lee and M. Ghovanloo, "Energy management integrated circuits for wireless power transmission," in *Implantable Biomedical Microsystems*. Elsevier, 2015, pp. 87–111.

[14] G. Simard, M. Sawan, and D. Massicotte, "High-speed OQPSK and efficient power transfer through inductive link for biomedical implants," *IEEE Trans. on biomed. circuits and syst.*, vol. 4, no. 3, pp. 192–200, 2010.

[15] A. Trigui *et al.*, "A 1.5-pj/bit, 9.04-mbit/s carrier-width demodulator for data transmission over an inductive link supporting power and data transfer," *IEEE Trans. Circuits Syst. II: Exp. Briefs*, vol. 65, no. 10, pp. 1420–1424, 2018.

[16] A. B. Amar, A. B. Kouki, and H. Cao, "Power approaches for implantable medical devices," *Sensors*, vol. 15, no. 11, pp. 28 889–28 914, 2015.

[17] G. Ciuti, A. Menciassi, and P. Dario, "Capsule endoscopy: from current achievements to open challenges," *IEEE Rev. Biomed. Eng.*, vol. 4, pp. 59–72, 2011.

[18] C. Eder *et al.*, "A cmos smart temperature and humidity sensor with combined readout," *Sensors*, vol. 14, no. 9, pp. 17 192–17 211, 2014.

[19] M. S. Chae *et al.*, "A 128-channel 6 mw wireless neural recording ic with spike feature extraction and uwb transmitter," *IEEE Trans. Neural Conf. Rehabil. Eng.*, vol. 17, no. 4, pp. 312–321, 2009.

[20] R. A. Huggins, "Supercapacitors and electrochemical pulse sources," *Solid State Ionics*, vol. 134, no. 1-2, pp. 179–195, 2000.

[21] C. Portz, "Power e-mergency: Combining renewable energy with current battery technology for emergency medical professionals," *Seattle J. Envtl. L.*, vol. 6, p. 189, 2016.

[22] R. Latham, R. Linford, and W. Schlindwein, "Biomedical applications of batteries," *Solid State Ionics*, vol. 172, no. 1-4, pp. 7–11, 2004.

[23] G. Xiong *et al.*, "A review of graphene-based electrochemical microsupercapacitors," *Electroanalysis*, vol. 26, no. 1, pp. 30–51, 2014.

[24] R. Abdelhedi *et al.*, "Optimal power sharing between batteries and supercapacitors in electric vehicles," *in 7th Int. Conf. Sci. of Electron. Technol. Informat. Telecom. (SETIT)*, pp. 97–103, 2016.

[25] A. P. Hu *et al.*, "Wireless power supply for icp devices with hybrid supercapacitor and battery storage," *IEEE J. Emerg. Sel. Topics Power Electron.*, vol. 4, no. 1, pp. 273–279, 2016.

[26] S. K. Wolfson Jr *et al.*, "The bioautofuel cell: a device for pacemaker power from direct energy conversion consuming autogenous fuel," *ASAIO Journal*, vol. 14, no. 1, pp. 198–203, 1968.

[27] B. R. Lokesh and M. L. Cunningham, "Further studies on the formation of oxygen radicals by potassium superoxide in aqueous medium for biochemical investigations," *Toxicology letters*, vol. 34, no. 1, pp. 75–84, 1986.

[28] R. A. Bullen *et al.*, "Biofuel cells and their development," *Biosens. Bioelectron.*, vol. 21, no. 11, pp. 2015–2045, 2006.

[29] M. Osman, A. Shah, and F. Walsh, "Recent progress and continuing challenges in bio-fuel cells. part ii: Microbial," *Biosens. Bioelectron.*, vol. 26, no. 3, pp. 953–963, 2010.

[30] K. Javor, J.-N. Tisserant, and A. Stemmer, "Biofuel cell operating on activated thp-1 cells: A fuel and substrate study," *Biosens. Bioelectron.*, vol. 87, pp. 1–6, 2017.

[31] A. P. Chandrakasan, N. Verma, and D. C. Daly, "Ultralow-power electronics for biomedical applications," *Annual Rev. Biomed. Eng*, vol. 10, 2008.

[32] M. Ashraf and N. Masoumi, "A thermal energy harvesting power supply with an internal startup circuit for pacemakers," *IEEE Trans. Very Large Scale Integr. (VLSI) Syst.*, vol. 24, no. 1, pp. 26–37, 2016.

[33] A. Kim *et al.*, "New and Emerging Energy Sources for Implantable Wireless Microdevices," *IEEE Access*, vol. 3, pp. 89–98, 2015.

[34] K. Bazaka and M. V. Jacob, "Implantable devices: issues and challenges," *Electronics*, vol. 2, no. 1, pp. 1–34, 2013.

[35] D. C. Bock *et al.*, "Batteries used to power implantable biomedical devices," *Electrochimica acta*, vol. 84, pp. 155–164, 2012.

[36] Y.-H. Joung, "Development of implantable medical devices: from an engineering perspective," *Int. Neurourology J.*, vol. 17, no. 3, p. 98, 2013.

[37] K. Striebel *et al.*, *Lithium and Lithium-ion Batteries: Proceedings of the international symposium*. Electrochemical Society, 2004.

[38] L. Timmermann *et al.*, "A new rechargeable device for deep brain stimulation: a prospective patient satisfaction survey," *Eur. Neurol.*, vol. 69, no. 4, pp. 193–199, 2013.

[39] Q. Li and H. Ardebili, "Flexible thin-film battery based on solid-like ionic liquid-polymer electrolyte," *J. Power Sources*, vol. 303, pp. 17–21, 2016.

[40] K.-T. Lee *et al.*, "A low temperature increase transcutaneous battery charger for implantable medical devices," *J. Mechanics Med. Biol.*, vol. 16, no. 05, p. 1650069, 2016.

[41] *Contego 325 mAh Battery*, EaglePicher Medical Power, LLC, 3 2016. [Online]. Available: https://www.eaglepicher.com/sites/default/files/Contego%20325%20Mar%202016.pdf

[42] C. Liu *et al.*, "Design and safety considerations of an implantable rectenna for far-field wireless power transfer," *IEEE Tran. Antennas Propag.*, vol. 62, no. 11, pp. 5798–5806, 2014.

[43] X. Lu *et al.*, "Wireless charging technologies: Fundamentals, standards, and network applications," *IEEE Commun. Surveys Tuts.*, vol. 18, no. 2, pp. 1413–1452, 2016.

[44] K. Goto *et al.*, "An implantable power supply with an optically rechargeable lithium battery," *IEEE Trans. Biomed. Eng.*, vol. 48, no. 7, pp. 830–833, 2001.

[45] M. Mujeeb-U-Rahman *et al.*, "Optical power transfer and communication methods for wireless implantable sensing platforms," *J. Biomed. Optics*, vol. 20, no. 9, p. 095012, 2015.

[46] S. Ozeri and D. Shmilovitz, "Ultrasonic transcutaneous energy transfer for powering implanted devices," *Ultrasonics*, vol. 50, no. 6, pp. 556–566, 2010.

[47] M. Donohoe *et al.*, "Powering in-body nanosensors with ultrasounds," *IEEE Trans. Nanotechnol.*, vol. 15, no. 2, pp. 151–154, 2016.

[48] L. Radziemski and I. R. S. Makin, "In vivo demonstration of ultrasound power delivery to charge implanted medical devices via acute and survival porcine studies," *Ultrasonics*, vol. 64, pp. 1–9, 2016.

[49] M. A. Sharif and A. M. Sodagar, "Capacitive links for power and data telemetry to implantable biomedical microsystems," *Handbook of Biochips: Integr. Circuits Conf. Biol. Med.*, pp. 1–23, 2015.

[50] A. Trigui *et al.*, "Inductive power transfer system with self-calibrated primary resonant frequency," *IEEE Trans. Power Electron.*, vol. 30, no. 11, pp. 6078–6087, 2015.

[51] F. Inanlou, M. Kiani, and M. Ghovanloo, "A novel pulse-based modulation technique for wideband low power communication with neuroprosthetic devices," *in IEEE Annual Int. Conf. Eng. Med. Biol. Soc. (EMBC)*, pp. 5326–5329, 2010.

[52] M. Hasanuzzaman *et al.*, "Toward an Energy-Efficient High-Voltage Compliant Visual Intracortical Multichannel Stimulator," *IEEE Trans. VLSI Syst.*, vol. 26, no. 5, pp. 878–891, 2018.

[53] C. Sawma *et al.*, "Bidirectional Parallel Capacitive Data Links: Modeling and Experimental Results," *IEEE Access*, 2018.

[54] A. Hassan *et al.*, "Spatial carrier position modulation based multichannel capacitive link for bioelectronic implants," *in IEEE Biomed. Circuits Syst. Conf. (BioCAS)*, pp. 57–60, 2015.

[55] K. Van Schuylenbergh and R. Puers, *Inductive powering: basic theory and application to biomedical systems.* Springer Science & Business Media, 2009.

[56] N. Tesla, *My inventions: the autobiography of Nikola Tesla.* Simon and Schuster, 2013.

[57] S. S. Mohammed *et al.*, "Wireless power transmission–a next generation power transmission system," *Int. J. Comput. Appl.*, vol. 1, no. 13, pp. 100–103, 2010.

[58] K. Agarwal *et al.*, "Wireless power transfer strategies for implantable bioelectronics," *IEEE reviews in biomedical engineering*, vol. 10, pp. 136–161, 2017.

[59] S. Hached *et al.*, "A bluetooth-based low-energy qi-compliant battery charger for implantable medical devices," *in IEEE Int. Symp. Bioelectron. Bioinformatics*, pp. 1–4, 2014.

[60] T. C. Rao and K. Geetha, "Categories, standards and recent trends in wireless power transfer: A survey," *Indian J. Sci. Technol.*, vol. 9, no. 20, 2016.

[61] Y. Hu, M. Sawan, and M. N. El-Gamal, "An integrated power recovery module dedicated to implantable electronic devices," *Analog Integ. Circuits Signal Process.*, vol. 43, no. 2, pp. 171–181, 2005.

[62] P. Aqueveque *et al.*, *After Stroke Movement Impairments: A Review of Current Technologies for Rehabilitation.* InTech, 2017.

[63] S. Rizvi and K. Kumar, "A case for spinal cord stimulation therapy don't delay," *Pract. Pain Manag.*, vol. 13, pp. 48–61, 2013.

[64] M. Friedman *et al.*, "Targeted hypoglossal nerve stimulation for the treatment of obstructive sleep apnea: Six month results," *The Laryngoscope*, vol. 126, no. 11, pp. 2618–2623, 2016.

[65] I. Hochmair *et al.*, "Med-el cochlear implants: state of the art and a glimpse into the future," *Trends in amplification*, vol. 10, no. 4, pp. 201–219, 2006.

[66] A. M. Kuczapski and G. D. Andreescu, "Real-time interfacing for fault detection and auralization with med-el cochlear implant processors," *in IEEE 11th Int. Symp. Appl. Comput. Intell. Info. (SACI)*, pp. 191–196, 2016.

[67] Y. H.-L. Luo and L. da Cruz, "The argus® ii retinal prosthesis system," *Prog. Retin. Eye Res.*, vol. 50, pp. 89 – 107, 2016.

[68] A. Trigui *et al.*, "Prosthetic power supplies," *Wiley Encyclo. Electr. Electron. Eng.*, 2015.

[69] K. N. Bocan and E. Sejdi, "Adaptive transcutaneous power transfer to implantable devices: A state of the art review," *Sensors*, vol. 16, no. 3, p. 393, 2016.

[70] M. Zargham and P. G. Gulak, "Maximum achievable efficiency in near-field coupled power-transfer systems," *IEEE Trans. Biomed. Circuits Syst.*, vol. 6, no. 3, pp. 228–245, 2012.

[71] M. Kiani and M. Ghovanloo, "A figure-of-merit for designing high-performance inductive power transmission links," *IEEE Trans. Ind. Electron.*, vol. 60, no. 11, pp. 5292–5305, 2013.

[72] S. Mehri *et al.*, "Geometry optimization approaches of inductively coupled printed spiral coils for remote powering of implantable biomedical sensors," *J. Sensors*, vol. 2016, 2016.

[73] ——, "Minimizing printed spiral coil losses for inductive link wireless power transfer," *in IEEE Wireless Power Transfer Conf. (WPTC)*, pp. 1–4, 2016.

[74] Y.-P. Lin *et al.*, "A battery-less, implantable neuro-electronic interface for studying the mechanisms of deep brain stimulation in rat models," *IEEE Trans. on biomed. circuits and syst.*, vol. 10, no. 1, pp. 98–112, 2015.

[75] A. I. AL-Kalbani, M. R. Yuce, and J.-M. Redouté, "A study of reliable bio-telemetry, efficient powering and electromagnetic exposure in implantable neural systems," *Biomedical Engineering Letters*, vol. 3, no. 1, pp. 32–38, 2013.

[76] S. Mao *et al.*, "Simultaneous wireless power transfer and data communication using synchronous pulse-controlled load modulation," *Measurement*, vol. 109, pp. 316–325, 2017.

[77] S. N. Makarov, R. Ludwig, and S. J. Bitar, *Practical Electrical Engineering*. Springer, 2016.

[78] F. Yuan, "Design techniques for ask demodulators of passive wireless microsystems: a state-of-the-art review," *Analog Integrated Circuits and Signal Processing*, vol. 63, no. 1, pp. 33–45, 2010.

[79] A. Yakovlev, S. Kim, and A. Poon, "Implantable biomedical devices: Wireless powering and communication," *IEEE Communications Magazine*, vol. 50, no. 4, 2012.

[80] A. Trigui, M. Ali, A. C. Ammari, Y. Savaria, and M. Sawan, "Quad-Level Carrier Width Modulation Demodulator for Micro-implants," in *14th IEEE Int. New Circuits and Syst. Conf.*, 2016, pp. 1–4.

[81] A. Trigui *et al.*, "A 14.5 μw generic carrier width demodulator for telemetry-based medical devices," in *15th IEEE Int. New Circuits Syst. Conf.*, 2017, pp. 369–372.

[82] ——, "Energy efficient generic demodulator for high data transmission rate over an inductive link for implantable devices," *IEEE Access*, vol. 7, pp. 159 379–159 389, 2019.

[83] ——, "Generic wireless power transfer and data communication system based on a novel modulation technique," *IEEE Trans. Circuits Syst. I*, vol. 00, no. 00, pp. 0000–0000, 2020 (Submitted).

[84] L. Wentai *et al.*, "Implantable biomimetic microelectronic systems design," *IEEE Eng. Med. Biol. Mag.*, vol. 24, no. 5, pp. 66–74, 2005.

[85] S. A. Mirbozorgi *et al.*, "A single-chip full-duplex high speed transceiver for multi-site stimulating and recording neural implants," *IEEE Trans. Biomed. Circuits Syst.*, vol. 10, no. 3, pp. 643–653, 2016.

[86] C. Gong *et al.*, "A magnetic-balanced inductive link for the simultaneous uplink data and power telemetry," *Sensors*, vol. 17, no. 8, p. 1768, 2017.

[87] S. Atluri and M. Ghovanloo, "Design of a wideband power-efficient inductive wireless link for implantable biomedical devices using multiple carriers," *in 2nd Int. IEEE EMBS Conf. Neural Eng.*, pp. 533–537, 2005.

[88] M. Ghovanloo and S. Atluri, "A wide-band power-efficient inductive wireless link for implantable microelectronic devices using multiple carriers," *IEEE Trans. Circuits Syst. I: Reg. Papers*, vol. 54, no. 10, pp. 2211–2221, 2007.

[89] M. Kiani and M. Ghovanloo, "A 20-mb/s pulse harmonic modulation transceiver for wideband near-field data transmission," *IEEE Trans. Circuits Syst. II: Express Briefs*, vol. 60, no. 7, pp. 382–386, 2013.

[90] ——, "A 13.56-mbps pulse delay modulation based transceiver for simultaneous near-field data and power transmission," *IEEE Trans. Biomed. Circuits Syst.*, vol. 9, no. 1, pp. 1–11, 2015.

[91] Y. Hu and M. Sawan, "A fully integrated low-power BPSK demodulator for implantable medical devices," *IEEE Trans. Circuits Syst.*, vol. 52, no. 12, pp. 2552–2562, 2005.

[92] M. Sawan, H. Yamu, and J. Coulombe, "Wireless smart implants dedicated to multichannel monitoring and microstimulation," *IEEE Circuits Syst. Mag.*, vol. 5, no. 1, pp. 21–39, 2005.

[93] V. Garcerán-Hernández and E. A. Martínez-Rams, "Cochlear implant: Transcutaneous transmission link with ofdm," pp. 358–367, 2013.

[94] E. G. Kilinc, C. Dehollain, and F. Maloberti, "A low-power ppm demodulator for remotely powered batteryless implantable devices," *in Int. Midwest Sym. Circuits Syst. (MWSCAS)*, pp. 318–321, 2014.

[95] K. Ture *et al.*, "Remotely powered ppm demodulator by inductive coupling for rodent applications," *Analog Integr. Circuits Signal Process.*, vol. 88, no. 2, pp. 359–368, 2016.

[96] V. K. Khanna, "Wireless Communications and Powering of Implants," in *Implantable Medical Electronics*. Springer, 2016, pp. 185–207.

[97] P. R. Troyk *et al.*, "Suspended carrier modulation of high-q transmitters," dec " 9" 1997, US Patent 5,697,076.

[98] P. R. Troyk and M. Edgington, "Inductive links and drivers for remotely-powered telemetry systems," in *Antennas and Propagation Society International Symposium, 2000. IEEE*, vol. 1. IEEE, 2000, pp. 60–62.

[99] B. Park *et al.*, "An inductively coupled power and data link with self-referenced ask demodulator and wide-range ldo for bio-implantable devices," *J. Semicond. Technol. Sci.*, vol. 17, no. 1, pp. 120–128, 2017.

[100] S. Mandal and R. Sarpeshkar, "Power-efficient impedance-modulation wireless data links for biomedical implants," *IEEE Trans. on Biomed. Circuits and Syst.*, vol. 2, no. 4, pp. 301–315, 2008.

[101] C.-S. A. Gong *et al.*, "A miniaturized psk demodulation device for short-range wireless neural prosthetic systems," in *2nd IEEE Bioinformatics Biomed. Eng. Conf.*, 2008, pp. 1565–1568.

[102] C.-K. Liang *et al.*, "An implantable bi-directional wireless transmission system for transcutaneous biological signal recording," *Physiol. Meas.*, vol. 26, no. 1, p. 83, 2005.

[103] R. Puers and J. Thoné, *Short Distance Wireless Communications*. Boston, MA: Springer US, 2011, pp. 219–277.

[104] P. R. Troyk and S. F. Cogan, "Sensory neural prostheses," in *Neural Engineering*. Springer, 2005, pp. 1–48.

[105] P. Troyk *et al.*, "Development of bion/spl trade/technology for functional electrical stimulation: bidirectional telemetry," *in the 23rd Annual Int. Conf. Proc. IEEE Eng. Med. Biol. Soc.*, vol. 2, pp. 1317–1320, 2001.

[106] L. Yu, B. Kim, and E. Meng, "Chronically implanted pressure sensors: Challenges and state of the field," *Sensors*, vol. 14, no. 11, p. 20620, 2014.

[107] C. Sauer *et al.*, "Power harvesting and telemetry in CMOS for implanted devices," *IEEE Trans. Circuits Syst. I: Reg. Papers*, vol. 52, no. 12, pp. 2605–2613, 2005.

[108] M. Ghovanloo and G. Lazzi, "Transcutaneous magnetic coupling of power and data," *Wiley Encycl. Biom. Eng.*, 2006.

[109] G. Bawa and M. Ghovanloo, "Active high power conversion efficiency rectifier with built-in dual-mode back telemetry in standard cmos technology," *IEEE Trans. Biomed. Circuits Syst.*, vol. 2, no. 3, pp. 184–192, 2008.

[110] D. Jiang *et al.*, "An Integrated Passive Phase-Shift Keying Modulator for Biomedical Implants With Power Telemetry Over a Single Inductive Link," *IEEE Trans. on Biomed. Circuits and Syst.*, 2016.

[111] S. Ha *et al.*, "Energy Recycling Telemetry IC With Simultaneous 11.5 mW Power and 6.78 Mb/s Backward Data Delivery Over a Single 13.56 MHz Inductive Link," *IEEE J. of Solid-State Circuits*, vol. 51, no. 11, pp. 2664–2678, 2016.

[112] D. Cirmirakis *et al.*, "A fast passive phase shift keying modulator for inductively coupled implanted medical devices," pp. 301–304, 2012.

[113] G. Wang *et al.*, "Design and analysis of an adaptive transcutaneous power telemetry for biomedical implants," *IEEE Trans. Circuits Syst. I: Reg. Papers*, vol. 52, no. 10, pp. 2109–2117, 2005.

[114] Y. P. Lin *et al.*, "A battery-less, implantable neuro-electronic interface for studying the mechanisms of deep brain stimulation in rat models," *IEEE Trans. Biomed. Circuits Syst.*, vol. 10, no. 1, pp. 98–112, 2016.

[115] H.-M. Lee and M. Ghovanloo, "An integrated power-efficient active rectifier with offset-controlled high speed comparators for inductively powered applications," *IEEE Trans. Circuits Syst. I: Reg. Papers*, vol. 58, no. 8, pp. 1749–1760, 2011.

[116] H. Sohmyung *et al.*, "Energy-recycling integrated 6.78-mbps data 6.3-mw power telemetry over a single 13.56-mhz inductive link," pp. 1–2, 2014.

[117] H. Sohmyung and G. Cauwenberghs, "Wireless data and power transfer over an inductive telemetry link," Jan. 16 2018, US Patent 9,872,089.

[118] S. Mehri *et al.*, "Design Optimization of Multiple-Layer PSCs with Minimal Losses for Efficient and Robust Inductive Wireless Power Transfer," *IEEE Access*, vol. 6, pp. 31 924–31 934, 2018.

[119] C. Gong *et al.*, "An NFC on two-coil WPT link for implantable biomedical sensors under ultra-weak coupling," *Sensors*, vol. 17, no. 6, p. 1358, 2017.

[120] W. Xu, Z. Luo, and S. Sonkusale, "Fully digital bpsk demodulator and multilevel lsk back telemetry for biomedical implant transceivers," *IEEE Trans. Circuits Syst. II: Exp. Briefs*, vol. 56, no. 9, pp. 714–718, 2009.

[121] Y. Hu, J.-F. Gervais, and M. Sawan, "High power efficiency inductive link with full-duplex data communication," in *9th IEEE International Conference on Electronics, Circuits and Systems*, vol. 1, 2002, pp. 359–362.

[122] M. Catrysse, B. Hermans, and R. Puers, "An inductive power system with integrated bi-directional data-transmission," *Sensor. Actuat. A-Phys.*, vol. 115, no. 2-3, pp. 221–229, 2004.

[123] M. Cheng, *Medical device regulations: global overview and guiding principles*. World Health Organization, 2003.

[124] S. K. Gupta, "Medical Device Regulations: A Current Perspective." *J. Young Pharmacists*, vol. 8, no. 1, 2016.

[125] A.-F. Motte *et al.*, "Existing reporting guidelines for clinical trials are not completely relevant for implantable medical devices: a systematic review," *J. clin. epidemiol.*, 2017.

[126] Y.-J. Chen *et al.*, "A Comparative Study of Medical Device Regulations: US, Europe, Canada, and Taiwan," *Ther. Innov. & Regul. Sci.*, vol. 52, no. 1, pp. 62–69, 2018.

[127] C. M. Brendel, "Biocompatibility of polymer implants for medical applications," Ph.D. dissertation, University of Akron, 2009.

[128] V. K. Khanna, "Biomaterials for Implants," in *Implantable Medical Electronics*. Springer, 2016, pp. 153–166.

[129] M. Saini *et al.*, "Implant biomaterials: A comprehensive review," *World J. Clin. Cases: WJCC*, vol. 3, no. 1, p. 52, 2015.

[130] S. Hached *et al.*, "Novel, wirelessly controlled, and adaptive artificial urinary sphincter," *IEEE/ASME Trans. Mechatronics*, vol. 20, no. 6, pp. 3040–3052, 2015.

[131] H. M. Madjar, "Human radio frequency exposure limits: An update of reference levels in Europe, USA, Canada, China, Japan and Korea," in *IEEE International Symposium on Electromagnetic Compatibility-EMC EUROPE*, 2016, pp. 467–473.

[132] A. S. Poon, S. O'Driscoll, and T. H. Meng, "Optimal frequency for wireless power transmission into dispersive tissue," *IEEE Trans. Antennas Propag.*, vol. 58, no. 5, pp. 1739–1750, 2010.

[133] W. Kainz *et al.*, "Electromagnetic compatibility of electronic implants-review of the literature," *Wiener Klinische Wochenschrift*, vol. 113, no. 23/24, pp. 903–914, 2001.

[134] F. G. Shellock, "MRI safety and neuromodulation systems," in *Neuromodulation*. Elsevier, 2009, pp. 243–281.

[135] J. D. Weiland *et al.*, "Assessment of MRI issues for the Argus II retinal prosthesis," *Magnetic resonance imaging*, vol. 30, no. 3, pp. 382–389, 2012.

[136] M. L. Carlson *et al.*, "Magnetic resonance imaging with cochlear implant magnet in place: safety and imaging quality," *Otology & Neurotology*, vol. 36, no. 6, pp. 965–971, 2015.

[137] M. L. Navaii, M. Jalali, and H. Sadjedi, "A 34-pj/bit area-efficient ask demodulator based on switching-mode signal shaping," *IEEE Trans. Circuits Syst. II, Exp. Briefs*, vol. 64, no. 6, pp. 640–644, 2017.

[138] M. Ghovanloo and K. Najafi, "A wideband frequency-shift keying wireless link for inductively powered biomedical implants," *IEEE Transactions on Circuits and Systems I: Regular Papers*, vol. 51, no. 12, pp. 2374–2383, 2004.

[139] M. Kiani and M. Ghovanloo, "A 20-mb/s pulse harmonic modulation transceiver for wideband near-field data transmission," *IEEE Trans. Circuits Syst. II: Exp. Briefs*, vol. 60, no. 7, pp. 382–386, 2013.

[140] ——, *Centimeter-Range Inductive Radios*. Springer, 2015, pp. 313–341.

[141] L. Zhou, "Passive phase shift modulation for high-speed data transmission in implantable closed-loop neuroprostheses," Ph.D. dissertation, UCL (University College London), 2005.

[142] H. Lee *et al.*, "Differentiating ask demodulator for contactless smart cards supporting vhbr," *IEEE Trans. Circuits Syst. II, Exp. Briefs*, vol. 62, no. 7, pp. 641–645, 2015.

[143] N. Mousavi, M. Sharifkhani, and M. Jalali, "Ultra-low power current mode all-mos ask demodulator for radio frequency identification applications," *IET Circuits, Devices & Systems*, vol. 10, no. 2, pp. 130–134, 2016.

[144] A. Trigui *et al.*, "Maximizing data transmission rate for implantable devices over a single inductive link: Methodological review," *IEEE reviews in biomedical engineering*, vol. 12, pp. 72–87, 2018.

[145] H.-J. Kim *et al.*, "Review of near-field wireless power and communication for biomedical applications," *IEEE Access*, vol. 5, pp. 21 264–21 285, 2017.

[146] A. Tantin *et al.*, "Implantable mics-based wireless solution for bladder pressure monitoring," in *IEEE Biomedical Circuits and Systems Conference (BioCAS)*, 2017, pp. 572–575.

[147] M. Hasanuzzaman *et al.*, "Toward an energy-efficient high-voltage compliant visual intracortical multichannel stimulator," *IEEE Transactions on Very Large Scale Integration (VLSI) Systems*, vol. 26, no. 5, pp. 878–891, 2018.

[148] L. Radziemski and I. R. S. Makin, "In vivo demonstration of ultrasound power delivery to charge implanted medical devices via acute and survival porcine studies," *Ultrasonics*, vol. 64, pp. 1–9, 2016.

[149] M. Mujeeb-U-Rahman *et al.*, "Optical power transfer and communication methods for wireless implantable sensing platforms," *Journal of biomedical optics*, vol. 20, no. 9, p. 095012, 2015.

[150] S. Hached *et al.*, "A bluetooth-based low-energy qi-compliant battery charger for implantable medical devices," in *IEEE International Symposium on Bioelectronics and Bioinformatics (ISBB)*, 2014, pp. 1–4.

[151] A. Trigui *et al.*, "Prosthetic power supplies," *Wiley Encyclopedia of Electrical and Electronics Engineering*, 2015.

[152] M. Sawan, Y. Hu, and J. Coulombe, "Wireless smart implants dedicated to multichannel monitoring and microstimulation," *IEEE Circuits and systems magazine*, vol. 5, no. 1, pp. 21–39, 2005.

[153] Y. Hu and M. Sawan, "A fully integrated low-power BPSK demodulator for implantable medical devices," *IEEE Trans. on Circuits and Syst.*, vol. 52, no. 12, pp. 2552–2562, 2005.

[154] E. G. Kilinc, C. Dehollain, and F. Maloberti, *Remote powering and Data Communication for implanted biomedical systems*. Springer, 2015, vol. 131.

[155] M. A. Hannan *et al.*, "Automatic frequency controller for power amplifiers used in bio-implanted applications: Issues and challenges," *Sensors*, vol. 14, no. 12, pp. 23 843–23 870, 2014.

[156] A. Yakovlev, J. H. Jang, and D. Pivonka, "An 11 μw sub-pj/bit reconfigurable transceiver for mm-sized wireless implants," *IEEE transactions on biomedical circuits and systems*, vol. 10, no. 1, pp. 175–185, 2016.

[157] Y. Lu and W.-H. Ki, *CMOS integrated circuit design for wireless power transfer*. Springer, 2018.

[158] A. Trigui *et al.*, "Maximizing data transmission rate for implantable devices over a single inductive link: Methodological review," *IEEE reviews in biomedical engineering*, vol. 12, pp. 72–87, 2018.

[159] S. A. Mirbozorgi *et al.*, "A single-chip full-duplex high speed transceiver for multi-site stimulating and recording neural implants," *IEEE transactions on biomedical circuits and systems*, vol. 10, no. 3, pp. 643–653, 2016.

[160] Y.-P. Lin *et al.*, "A battery-less, implantable neuro-electronic interface for studying the mechanisms of deep brain stimulation in rat models," *IEEE transactions on biomedical circuits and systems*, vol. 10, no. 1, pp. 98–112, 2016.

[161] C. Huang, T. Kawajiri, and H. Ishikuro, "A 13.56-mhz wireless power transfer system with enhanced load-transient response and efficiency by fully integrated wireless constant-idle-time control for biomedical implants," *IEEE Journal of Solid-State Circuits*, vol. 53, no. 2, pp. 538–551, 2018.

[162] S. A. Rackley, *Wireless networking technology: From principles to successful implementation*. Elsevier, 2011.

[163] E. G. Kilinc, C. Dehollain, and F. Maloberti, *Remote powering and Data Communication for implanted biomedical systems*. Springer, 2016.

[164] P. Fay, D. Jena, and P. Maki, "High-frequency gan electronic devices," 2019.

[165] L. Jiang and D. Costinett, "A high-efficiency gan-based single-stage 6.78 mhz transmitter for wireless power transfer applications," *IEEE Trans. on power electronics*, vol. 34, no. 8, pp. 7677–7692, 2018.

[166] A. Hassan *et al.*, "A gan-based wireless monitoring system for high-temperature applications," *Sensors*, vol. 19, no. 8, p. 1785, 2019.

[167] H. Sayed, A. Zurfi, and J. Zhang, "Effects of pcb power layouts design on switching transient performance of sic mosfets," *Analog Integrated Circuits and Signal Processing*, vol. 99, no. 1, pp. 81–93, 2019.

[168] H. C. Dymond and B. H. Stark, "Investigation of a parasitic-inductance reduction technique for through-hole packaged power devices," in *2018 IEEE Energy Conversion Congress and Exposition (ECCE)*. IEEE, 2018, pp. 1964–1968.

[169] T. Liu *et al.*, "Modeling and analysis of sic mosfet switching oscillations," *IEEE Journal of Emerging and Selected Topics in Power Electronics*, vol. 4, no. 3, pp. 747–756, 2016.

[170] Z. Zeng and X. Li, "Comparative study on multiple degrees of freedom of gate drivers for transient behavior regulation of sic mosfet," *IEEE Trans. on power electronics*, vol. 33, no. 10, pp. 8754–8763, 2017.

[171] R. Severns and E. Reduce, "Design of snubbers for power circuits," *International Rectifier Corporation*, 2006.

[172] Y. Lee, "Rfid coil design," *Microchip Technol. Inc. Appl. Note*, 1998.

[173] N. Desai *et al.*, "An actively detuned wireless power receiver with public key cryptographic authentication and dynamic power allocation," *IEEE Journal of Solid-State Circuits*, vol. 53, no. 1, pp. 236–246, 2017.

[174] D. Ye *et al.*, "A wireless power and data transfer receiver achieving 75.4% effective power conversion efficiency and supporting 0.1% modulation depth for ask demodulation," *IEEE Journal of Solid-State Circuits*, 2019.

[175] J. Brown and S. Salmons, "Percutaneous switching of an implantable muscle stimulator via an optical link," *J. Biomed. Eng.*, vol. 3, no. 3, pp. 206–208, 1981.

[176] E. K. Lee, "An inside body power and bidirectional data transfer ic module pair," *IEEE J. Solid-State Circuits*, vol. 46, no. 8, pp. 1820–1831, 2011.

[177] B. B. Owens, *Batteries for implantable biomedical devices*. Springer Science & Business Media, 2012.

[178] C. F. Holmes, "The role of electrochemical power sources in modern health care," *Interface-Pennington-*, vol. 8, pp. 32–34, 1999.

[179] N. Ahuja *et al.*, "Wireless power for implantable devices: a technical review," *Wireless Computing in Medicine: From Nano to Cloud with Ethical and Legal Implications*, p. 187, 2016.

[180] T. P. Crompton, *Battery reference book*. Newnes, 2000.

[181] V. S. Mallela, V. Ilankumaran, and N. S. Rao, "Trends in cardiac pacemaker batteries," *Indian Pacing and Electrophysiology J.*, vol. 4, no. 4, p. 201, 2004.

[182] R. X. Stroobandt, S. S. Barold, and A. F. Sinnaeve, *Implantable cardioverter-defibrillators step by step: an illustrated guide*. John Wiley & Sons, 2011.

[183] W. H. Ko and J. Hynecek, "Implant evaluation of a nuclear power source-betacel battery," *IEEE Trans. Biomed. Eng.*, no. 3, pp. 238–241, 1974.

[184] F. Hein and R. Thull, *Engineering in Medicine: Volume 1: Advances in Pacemaker Technology*. Springer Science and Business Media, 2012.

[185] M. R. Palacin, "Recent advances in rechargeable battery materials: a chemist's perspective," *Chem. Soc. Rev.*, vol. 38, no. 9, pp. 2565–2575, 2009.

[186] R. E. Fischell, "The development of implantable medical devices at the applied physics laboratory," *Johns Hopkins APL Technical Digest*, vol. 13, no. 1, pp. 233–243, 1992.

[187] W. B. Fye, "Machines in our hearts: The cardiac pacemaker, the implantable defibrillator, and american health care," *Jama: The Journal of the American Med. Assoc.*, vol. 287, no. 13, pp. 1730–1731, 2002.

[188] M. Sawan *et al.*, "Wireless recording systems: From noninvasive eeg-nirs to invasive eeg devices," *IEEE Trans. Biomed. Circuits Syst.*, vol. 7, no. 2, pp. 186–195, 2013.

[189] C. Sawma, M. Sawan, and A. Kassem, "Capacitive data links intended for implantable medical devices: A survey," in *2015 International Conference on Advances in Biomedical Engineering (ICABME)*. IEEE, 2015, pp. 266–269.

[190] M. Hasanuzzaman *et al.*, "Capacitive-data links, energy-efficient and high-voltage compliant visual intracortical microstimulation system," in *2013 IEEE International Symposium on Circuits and Systems (ISCAS2013)*. IEEE, 2013, pp. 646–649.

[191] A. Hassan *et al.*, "Spatial carrier position modulation based multichannel capacitive link for bioelectronic implants," in *2015 IEEE Biomedical Circuits and Systems Conference (BioCAS)*. IEEE, 2015, pp. 1–4.

[192] B. Lenaerts and R. Puers, *Omnidirectional inductive powering for biomedical implants*. Springer, 2009.

APPENDIX A OTHER METHODS OF POWER AND DATA TRANSFER FOR IMDS

In this appendix, more information about existing power sources and wireless data transfer links are presented.

Conducting wires and cables are nowadays standard mediums for transmitting electrical energy. This is due to their capacity for relaying a flow of energy in a precise and efficient manner [175,176]. However, wires are inappropriate for powering IMDs. They restrict patient mobility. They can cause infections, tissue damage, and may corrode due to patient motion. Alternative solutions consist in using an internal battery integrated in the implantable device. It is also possible to employ external power sources to wirelessly power IMDs. Moreover, both battery and wireless power alternatives can be adopted when the IMD internal battery is rechargeable and consequently avoid battery replacement surgery.

Nowadays, only batteries and inductive links are used for powering commercial IMDs. In this Annexe, single use and rechargeable batteries meant for IMDs are reviewed. Bio batteries and specific supercapacitor power sources adding complementary features are then presented.

A.1 Batteries

To prevent affecting the normal activity of the patient, IMD battery sources should be light and compact while providing maximal autonomy. Minimizing size and weight of batteries are among the main design challenges. There are two main types of implantable batteries: (1) primary or single-use batteries (currently found in commercial pacemakers and deeply implanted stimulators) and (2) secondary or rechargeable batteries (used for example in neurostimulators) [34–36].

A.1.1 Primary (Single-Use) Batteries

The most commonly used "single-use" energy storage unit is the electrochemical battery. Such battery cell produces electrical energy by direct transformation of chemical energy. The first successful implant using an electrochemical cell was made in 1960 [177]. A nickel-cadmium battery (Ni-Cd) has been incorporated into a pacemaker to treat bradycardia. Later, a zinc/mercuric oxide (Zn/HgO) battery was developed and successfully implanted into a patient by the Greatbatch-Chardack team [178, 179]. Afterward, the invention of lithium-based power cells in the late 60s led to an attractive alternative to the first electrochemical

cells. With their high energy density (three times the energy of the Zn/HgO battery) Lithium batteries are still, to date, the most used type of batteries [180].

The lithium/iodine-polyvinylpyridine (PVP) cell was the first lithium-based battery implanted into a pacemaker. Over several decades, it has proved its safety and reliability for clinical use. Therefore, with their high power density (milliampere range), low self-discharge rate and longevity; Lithium/Manganese Dioxide (Li–MnO2), Lithium/Carbon monofluoride (Li/CFx), lithium/thionyl chloride and other varieties of lithium batteries were used to power neurostimulators, drug delivery systems, and pacemakers with additional functionalities [181].

Implantable Cardioverter Defibrillators (ICDs) pacing at fast rates require high power rate batteries. These batteries must be capable of delivering high current pulses of 2–3A to rapidly charge the capacitors of the device that subsequently shocks the heart to stop ventricular fibrillation [22,182]. Lithium/silver vanadium oxide (Li/SVO) and Lithium/Manganese Dioxide batteries are commonly used in most today's ICDs due to their high-power capabilities. These single-use lithium-based batteries establish advanced powering solutions, however, they require replacement surgery when depleted.

In the 1970s, another type of battery has been introduced in the IMD industry to extend the service lifetime. It is the nuclear battery [183]. Some manufacturers of IMDs, including Medtronic, have introduced nuclear models (such as Laurens-Alcatel model 9000) in their product lines [178, 184]. These devices have given patients the opportunity to have a lasting pacemaker. Nuclear batteries have been proved safe and effective. Their output power is stable and immune to external factors such as temperature, pressure and electromagnetic fields. However, nuclear batteries are costly as their internal materials particularly the radionuclide are very difficult to extract and use.

A.1.2 Secondary (Rechargeable) Batteries

The rechargeable battery is an electrochemical generator that can be "revived" when depleted. In rechargeable batteries, energy is generated by a chemical reaction between an electrolyte and two metallic electrodes [185]. When there is not enough reactive material in the electrodes, the battery is low and must be recharged. To do so, a DC-voltage is applied to the battery. This reverses the direction of the chemical process and replenishes the starting reactants thus allowing the battery to be used several times for many discharge/charging cycles. However, these cycles cannot be done indefinitely. After several charge/discharge cycles, the battery needs to be replaced.

The first rechargeable implantable pacemaker used a new kind of Ni-Cad battery [186]. The

later pacemaker was commercialized by Pacesetter Systems Inc (became then a division of St. Jude Medical) in 1973. This rechargeable pacemaker has not been a sale success. Pacemakers integrating single-use lithium batteries were also introduced to the market. They were smaller and offered longer service life without requiring the battery recharging equipment [186, 187]. Targeting higher energy capabilities and other improvements, such as smaller size and longer lifetime, rechargeable lithium-ion cells have emerged with great promises of compactness, safety, reliability and durability for many applications [37]. Therefore, some commercial IMDs, such as Medtronic neurostimulators (ex. The ACTIVA RC Neurostimulator for deep brain stimulation) were equipped with a lithium-ion rechargeable cell [38]. Currently, the use of lithium-ion rechargeable battery is intended for several IMDs under development such as neurostimulators to cure epilepsy and Parkinson's diseases, cochlear implants, Left Ventricular Assist Devices (LVADs) and artificial hearts. The Lithium-ion battery is not complicated to manufacture. However it requires elaborated tests to ensure safety. Actually, these secondary batteries should be well sealed and monitored all the time to prevent overheat and damage. Lithium-ion batteries are commonly recharged via an inductive link.

A.1.3 Other types of embedded power sources

Supercapacitors

Although, batteries are the primary choice for IMDs on-board powering, there are some specific applications that do require special power sources. In fact, some IMDs need to have a tiny volume or extreme high-power density. Supercapacitors, also named ultracapacitors provide these features. They are of smaller sizes and have higher-power densities compared to electrochemical batteries. They can generate short pulses of relatively high power [20]. They have faster charging rates (several milliseconds to seconds vs. several hours for batteries), longer lifespan (up to 1 million charge/discharge cycles vs. hundreds to thousands of cycles), larger operating temperature ranges and they are not subject to overcharge, which makes them safer [23].

Also known as electric double-layer capacitors (EDLC), a supercapacitor consists of two disjoined electrodes (separated by an ion-permeable membrane) immersed into an electrolyte that carries positive and negative ions. The energy can be stored in EDLCs by applying two storage principles: 1) Electrostatic storage, which is an accumulation of ions on the electrode/electrolyte interfaces; and 2) electrochemical storage (faradic pseudo-capacitance) which is a chemical reaction in which an exchange of electrons occurs at the surface or at the near-surface of the electrodes. Compared to conventional electrolytic capacitors, supercapacitors have a much higher capacitance (50 times greater) and a relatively smaller size [22].

However, the use of supercapacitors in IMDs is still limited due to its low energy density (5% of lithium batteries), fast self-discharge rate and low cell voltage (limited to 2.5V or 2.75V). The rapid technological progress in the field of miniaturized portable electronic devices led to the fabrication of on-chip micro-scale supercapacitors. These micro-supercapacitors provide ultra-fast charge/discharge rates and higher specific energy than conventional supercapacitors (2 times greater). Special attention has been given to the structures, the dimensions and the materials of the micro-supercapacitor elements to improve their performances. However, several challenges need to be addressed to increase the capacitance value and the energy storage performances [23].

There is also a trend supporting the combination of the supercapacitor with the lithium-ion battery resulting in a hybrid energy storage system. These hybrid elements offer the advantages of both the supercapacitor (fast-charge rate, high-power density), and the rechargeable battery (high-energy density). However, the latter combination adds size and complexity [21, 24, 25].

Bio-Fuel Cells

Another power source alternative to standard battery sources is the bio batteries for IMDs. In the 1970s, many studies were carried on the enzyme-based biofuel cells (using glucose or lactate as fuel and oxygen as oxidizer) in order to build new batteries for IMDs [26,27]. These biological molecules are present in physiological fluids such as blood. In addition, the body pH, temperature and pressure are adequate for efficient power generation [28,29]. Since 1984, many improvements were made on these biofuel cells [28] as they proved quite advantageous for IMDs. However, most biofuel cells proposed to date are unable to meet all the IMDs requirements. This is due to their short lifespan and low ability to generate sufficient power values (microwatt level) [30].

A.1.4 Wireless Data Communication for IMDs

The wireless communication for implanted medical devices is mandatory, and must be safe and reliable. Also, low-power solutions are required with high-data rate communication. There are principally two groups of wireless communication methods divided according to the operating field regions: the far field zone and the near-field zone [55, 103].

Far-field communication technologies

In this far-field region, the electric field vectors E and the magnetic fields vectors H are orthogonal to each other and to the propagation direction. Therefore, the measurement of one of the components (electrical or magnetic) is sufficient to know all the characteristics of the radiation. We can consider that we are in a far-field zone when

$$R \ > \ 2D^2 \ / \ \lambda \tag{A.1}$$

where R, D and λ are respectively the distance between the two antennas, the largest dimension of the antenna and the wavelength of the signal. The "far-field group" is divided in two categories according to the type of wave: the electromagnetic wave and the acoustic wave.

The electromagnetic wave can be mainly generated by two ways.

- When far-field antennas are used at each end of a link, a radio frequency (RF) communication link is established [188]. An AC current flowing through a transmitter antenna generates an electromagnetic field that propagates through space and tissues. It is then captured by the receiver antenna. The communication operating range using RF link is significantly higher than the carrier wavelength λ ($=\frac{c}{f}$ with c the speed of light and f the frequency of the carrier). Although, wireless RF links allows relatively long-range and high-speed data communication, they suffer from high power consumption, interference problems and safety concerns. This is due to their excessive in-tissue absorption and reflection at tissue boundaries that increase with the operating frequency [140].

- When light emitting, and photosensitive devices are respectively used at the transmitter and the receiver, an optical communication link is established. The absorption of light by soft tissue depends on the skin and blood optical behavior (absorption, scattering and reflectance). Due to the high absorption factor of human tissue, the optical link works best for IMDs located under the skin. The near-infrared light is the most widely used for IMD wireless communication because this kind of light can easily penetrate biological tissues. The advantages of using the optical wave (which is also a form of electromagnetic radiation) are mainly its high level of immunity against electromagnetic interference (EMI) and its extremely high data rates. However, Safety levels must be respected as radiation of relatively high intensity can cause tissue damage [45].

- The ultrasound link is also based on wave propagation. It uses the acoustic wave which is a vibration that propagates through physical mediums (fluids, solids, gases or liquids). This wave has a frequency greater than the audible range (20 Hz-17 kHz). To set up a wireless communication link, an ultrasound transducer can be used to convert electrical signals into

ultrasound waves. A piezoelectric receiver implanted in the human body can be used to receive and convert the ultrasound mechanical energy into electrical charge. Ultrasound has the advantage of deep penetration in tissue ability. However, an acoustic wave that propagates between different acoustic impedance's mediums may experience acoustic wave reflection (echo) [55].

Near-field communication technologies

The second wireless communication method operates in the near-field zone. In this region, the relationship between E and H fields is hard to predict [55]. Each one of these components may suddenly overcome the other. In this zone, there is no coupling by electromagnetic radiation. Instead, there is an electrical coupling that is similar to an electrical current flowing through a conductive or dielectric medium, such as for a capacitive link, or a magnetic coupling that is implemented by an inductive link. The near-field group gathers therefore two types of short-range links: the capacitive link and the inductive link defined as follows:

The capacitive link consists of two aligned parallel plates, one on the inner side of the skin and the other on the external side [189]. Due to its conductivity, the skin acts as a lossy dielectric. An AC voltage applied to the transmitter electrode plate generates an electric field that passes through the skin to the receiver electrode plate. Capacitive link is highly immune against electromagnetic interference (EMI) since the field lines are well confined between the two plates. Due to its high pass nature, the data rate is not limited by the channel capacity. Signals carrying a wide range of harmonics, like square waves, can be transmitted easily [189–191]. Wider plates improve the communication range and the bandwidth but also increase the tissue temperature, the patient discomfort, and pick up more background noise. In addition, a good electrical contact with the body (whether at emission or at reception) is needed to reduce the voltage drop caused by the air gap between the external electrode and the skin [192]. The capacitive link technique can be used for both power and data transmission, but it is often used for the data transfer because of its low ability to produce high enough energy.

The magnetic or inductive coupling is actually the most widely used method for through-tissue data communication [14]. The operating principle was described in Chapter 1. Challenges faced by the data communication based inductive link (particularly when the link is simultaneously used for power transfer) and the solutions proposed to tackle these challenges are discussed in the next chapters.

APPENDIX B INDUCTIVE LINK FUNDAMENTALS

This appendix presents a theoretical study of the basics of inductive links while focusing on the proposed circuit model for wireless power transfer. In this appendix, small italic letters represent time-domain variables, bold letters represent phasors and capital italic letters represent real numbers or RMS values.

B.1 Mutually coupled coils

The core of an inductive link is the magnetically coupled coils, which can be modeled with two coupled inductors, as shown in Fig. B.1. The corresponding circuit equations are given by

$$(r_{L1} + j\omega L_1)\,\mathbf{I_1} + j\omega\ M\mathbf{I_2} = \mathbf{V_s} \tag{B.1}$$

$$j\omega\ M\mathbf{I_1} + (r_{L2} + R_L + j\omega L_2)\,\mathbf{I_2} = 0 \tag{B.2}$$

where r_{L1} and r_{L2} are the resistance of the primary and secondary coils, respectively; L_1 and L_2 are the self-inductances of the primary and secondary coils, respectively; M is the mutual inductance between two coils; R_L is the equivalent load resistance.

When AC current flows i_1 through the primary coil, a magnetic flux is created in its vicinity. This flux is picked-up by the secondary coil and therefore converted to an AC voltage across it. i_1 produces also a loss of $r_{L1}\ I_1^2$ in the primary coil and induces a voltage with the RMS value of $\omega M I_1$ in the secondary coil. This induced voltage is applied on the secondary side

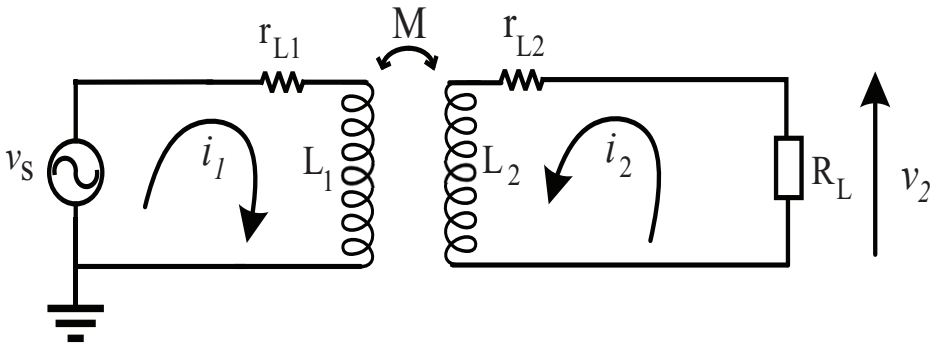

Figure B.1 The coupled coils.

impedance r_{L2}+R_L+$j\ \omega\ L_2$. The induced current I_2 will be limited by the reactance of the secondary coil. In fact, the current i_2 flowing through L_2 would cause an extra magnetic field that opposes the original flux changes, i.e. to the cause that gave birth to it (Lenz's law). Thereby, i_2 induces in the same way, a voltage with the RMS value of $\omega M I_2$ in the primary coil.

To express the coupling between two coils, there is another variable apart from the mutual inductance M. It is the coupling factor k whose value is between 0 and 1.

$$M = k\sqrt{L_1 L_2} \tag{B.3}$$

This factor strongly depends on the geometry of the coils (size and shape), their relative position (distance and angle) and the property of their materials. So giving it analytical expression wisely is not an easy task. However, Roz and Fuentes estimated it by the following equation :

$$k = \frac{ra_{L1}^2 ra_{L2}^2 cos\theta}{\sqrt{ra_{L1} ra_{L2}}(\sqrt{d_a^2 + ra_{L1}^2})^3} \tag{B.4}$$

ra_{L1} and ra_{L2} are the respective radii of the primary and secondary coil; d_a and θ are respectively the axial distance and the angle between the coils. However, equation B.4 only applies if $ra_{L2} \leq ra_{L1}$.

The secondary current phasor $\mathbf{I_2}$ can be derived from B.2 as:

$$\mathbf{I_2} = \frac{-j\omega M \mathbf{I_1}}{r_{L2} + R_L + j\omega L_2} \tag{B.5}$$

If the reactance of the secondary side impedance could be compensated, for example, by connecting a capacitor $1/\left(\omega C_2\right)$ in series with the secondary coil and canceling out the reactance, i.e.,

$$\omega\ L_2 - \frac{1}{\omega C_2} = 0 \tag{B.6}$$

then a larger current and a higher power can be transferred to the load. With the same input current in the primary coil, the output power is increased and thereby, the power transfer efficiency is improved. In the primary side, $j\omega\ L_1$ should be also compensated by using capacitors to minimize the required Volt-Amps (VA) rating of the system, i.e., a lower input voltage is required to generate the same input primary coil current. Therefore, primary

compensation also improves the power transfer capability of a WPT system.

One of the basic operation principles of magnetic resonance WPT is to compensate both the primary and secondary reactance's and thus, we have resonance in both the primary and secondary sides. This forms a basic magnetic resonance WPT system.

However, in order to reduce ringing effect as discussed in Chapter 5 and ensure CWM data communication, we were forced not to place a capacitor in the secondary circuit.

The circuit model of our proposed WPT system is given by Fig. B.2 and the following equations

$$(r_{L1} + jX_1)\,\mathbf{I_1} + j\omega\ M\mathbf{I_2} = \mathbf{V_s} \tag{B.7}$$

$$j\omega\ M\mathbf{I_1} + (r_{L2} + R_L + j\omega L_2)\,\mathbf{I_2} = 0 \tag{B.8}$$

where $X_1 = \omega\ L_1 - \frac{1}{\omega C_1}$

B.2 Reflected Impedance

From(B.8), we get

$$\mathbf{I_2} = \frac{-\boldsymbol{j}\omega M\mathbf{I_1}}{r_{L2} + R_L + j\omega L_2} \tag{B.9}$$

By substituting (B.9) into (B.7), we get the input impedance of the system as

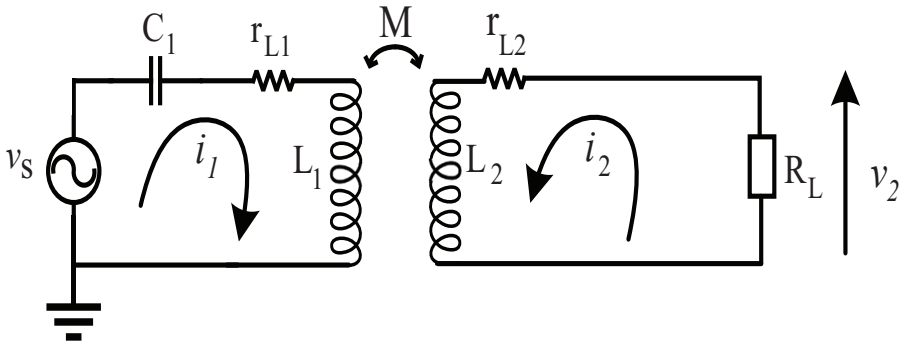

Figure B.2 The proposed inductive link for wireless power transfer.

$$\mathbf{Z_{in}} = \frac{\boldsymbol{V_s}}{\mathbf{I_1}} = r_{L1} + jX_1 + \frac{\omega^2 M^2}{r_{L2} + R_L + j\omega L_2} \tag{B.10}$$

The first term, $(r_{L1} + jX_1)$, is the impedance of the primary circuit. The second term is the reflected impedance, seen by the power source due to the current in the receiving coil. So the reflected impedance is given by

$$\mathbf{Z_r} = \frac{\omega^2 M^2}{r_{L2} + R_L + j\omega L_2} \tag{B.11}$$

If the system operates at the resonant frequency of the secondary tank, the reflected impedance has only the resistive part and it will not bring any reactance in the primary circuit. However, this is not the case for our secondary tank which operates out of resonance.

B.3 Induced Voltages, Currents and Gains

It is assumed that the resonant frequency of the primary tank is equal to the operating frequency of the system. Therefore, X_1 is zero. The induced voltage and current in the secondary side can be derived, respectively, as

$$\mathbf{V_{2_{induced}}} = j\omega\ M\mathbf{I_1} \tag{B.12}$$

If the parasitic resistance in the secondary side is neglected, (B.12) becomes

$$\mathbf{I_2} = \left(\frac{-j\omega M\left(r_{L2} + R_L\right)}{\left(r_{L2} + R_L\right)^2 + \omega^2 {L_2}^2} - \frac{\omega^2 M L_2}{\left(r_{L2} + R_L\right)^2 + \omega^2 {L_2}^2} \right) \mathbf{I_1} \tag{B.13}$$

Therefore, the phase angle between the primary and secondary currents is.

$$\theta \equiv \arctan\left(\frac{r_{L2} + R_L}{\omega L_2}\right) \tag{B.14}$$

And the current gain is derived as

$$\frac{I_2}{I_1} = \frac{\omega M}{\sqrt{\left(r_{L2} + R_L\right)^2 + \left(\omega L_2\right)^{\mathbf{2}}}} \tag{B.15}$$

If the parasitic resistance in the secondary side is neglected, (2.13) becomes

$$\frac{I_2}{I_1} = \frac{\omega M}{\sqrt{{R_L}^2 + (\omega L_2)^{\mathbf{2}}}} \tag{B.16}$$

We can notice that the current gain increases by decreasing the equivalent load R_L and the secondary coil inductance L_2.

Also, if the parasitic resistance is neglected, the load voltage become

$$\mathbf{V_L} = j\omega \mathbf{I_1} \left(M + L_2\right) \tag{B.17}$$

and the source voltage will be equal to the induced voltage, i.e.,

$$\mathbf{V}_{\boldsymbol{1_{induced}}} = \mathbf{V_S} = j\omega \ M\mathbf{I_2} \tag{B.18}$$

From (B.17), (B.18), and (B.16), the voltage gain can be obtained as

$$\frac{V_L}{V_S} = \frac{\sqrt{\left(r_{L2} + R_L\right)^2 + \left(\omega L_2\right)^2}}{\omega M}(1 + \frac{L_2}{M}) \tag{B.19}$$

If the parasitic resistance in the secondary side is neglected,

$$\frac{V_L}{V_S} = \frac{\sqrt{R_L^2 + \left(\omega L_2\right)^2}}{\omega M}(1 + \frac{L_2}{M}) \tag{B.20}$$

Hence, in contrary to the current gain, we can see that increasing R_L and L_2 may increase the voltage gain.

B.4 Power Transfer Efficiency

Because inductive WPT is based on the near-field coupling, the radiation loss is negligible and all the losses of the coupled coils will be on the parasitic resistances, i.e., r_{L1} and r_{L2}. Therefore, the efficiency of the system in Fig. B.2 can be expressed as

$$\eta = \frac{\boldsymbol{total\ output\ power}}{\boldsymbol{total\ input\ power}} = \frac{R_L I_2^2}{r_{L1} I_1^2 + \left(r_{L2} + R_L\right) I_2^2} = \frac{R_L}{r_{L1}\left(\frac{I_1}{I_2}\right)^2 + \left(r_{L2} + R_L\right)} \tag{B.21}$$

Substituting (B.16)in (B.21), we obtain

$$\eta = \frac{(\omega M)^2 \ R_L}{r_{L1}\left((r_{L2}+R_L)^2+(\omega L_2)^2\right)+(\omega M)^2(r_{L2}+R_L)} \tag{B.22}$$

If we neglect r_{L2}

$$\eta = \frac{(\omega M)^2}{r_{L1}\left(R_L+\frac{(\omega L_2)^2}{R_L}\right)+(\omega M)^2} \tag{B.23}$$

Since $\frac{\omega^2 M^2}{r_{L1}r_{L2}} = k^2 Q_1 Q_2$, η become

$$\eta = \frac{k^2 Q_1 Q_2}{\left(\frac{R_L}{r_{L2}}+\frac{(\omega L_2)^2}{r_{L2}R_L}\right)+k^2 Q_1 Q_2} \tag{B.24}$$

This further simplifies to:

$$\eta = \frac{1}{1+\frac{R_L}{k^2 Q_1 Q_2 r_{L2}}+\frac{r_{L2}}{k^2 Q_1 R_L}} \tag{B.25}$$

This equation proves that η increases when

$$\frac{R_L}{k^2 Q_1 Q_2 r_{L2}}+\frac{r_{L2}}{k^2 Q_1 R_L} \to 0 \tag{B.26}$$

i.e. the power efficiency increases for high $k^2 Q_1 Q_2$ and more particularly for high $k^2 Q_1$, as confirmed by simulation analysis.

During CWM data communication, the efficiency of the CWM modulated system will be equal to the efficiency of the system being activated, i.e., when the modulated signal is high. If the transient process is neglected and considering that '1' and '0' bits will be equiprobable, the power transfer efficiency η_{CWM} get the following expression:

$$\eta_{CWM} = pi * \eta \tag{B.27}$$

with pi is the powering index defined by

$$pi = 0.5\frac{t_{ON_1}+t_{ON_0}}{T_d} = 0.5\frac{(n-1)T_c+(n-2)T_c}{nT_c} = 0.5(2-\frac{3}{n}) \tag{B.28}$$

where T_c is the carrier cycle, n is the number of carrier cycles per data bit cycle T_d, and t_{ON_1}

and t_{ON_0} are the ON widths for either “1” and “0” data bit.

APPENDIX C EXPERIMENTAL PROTOTYPES

This appendix presents photos of the fabricated and tested chip and circuit board of the transmitter and the receiver prototypes.

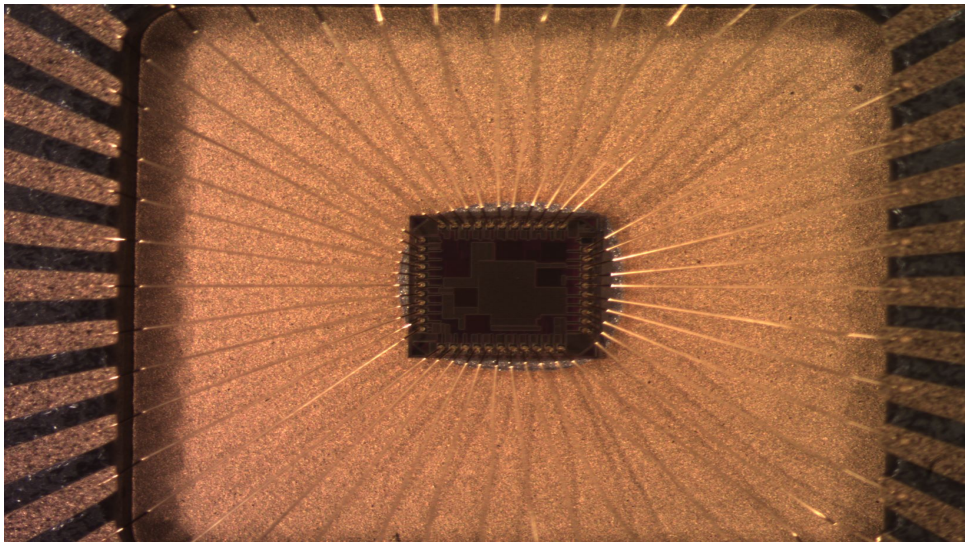

Figure C.1 Photograph of the wirebonded chip

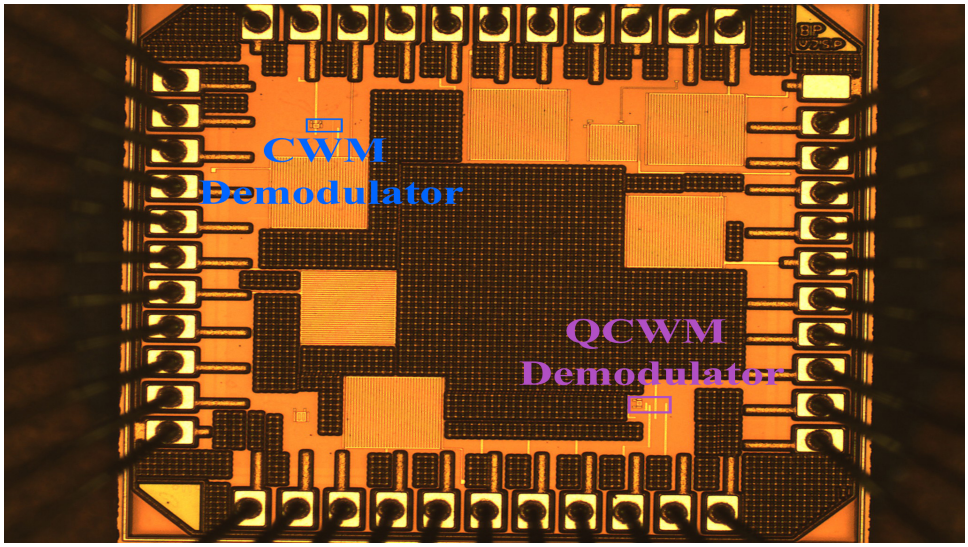

Figure C.2 Microphotograph of the whole die.

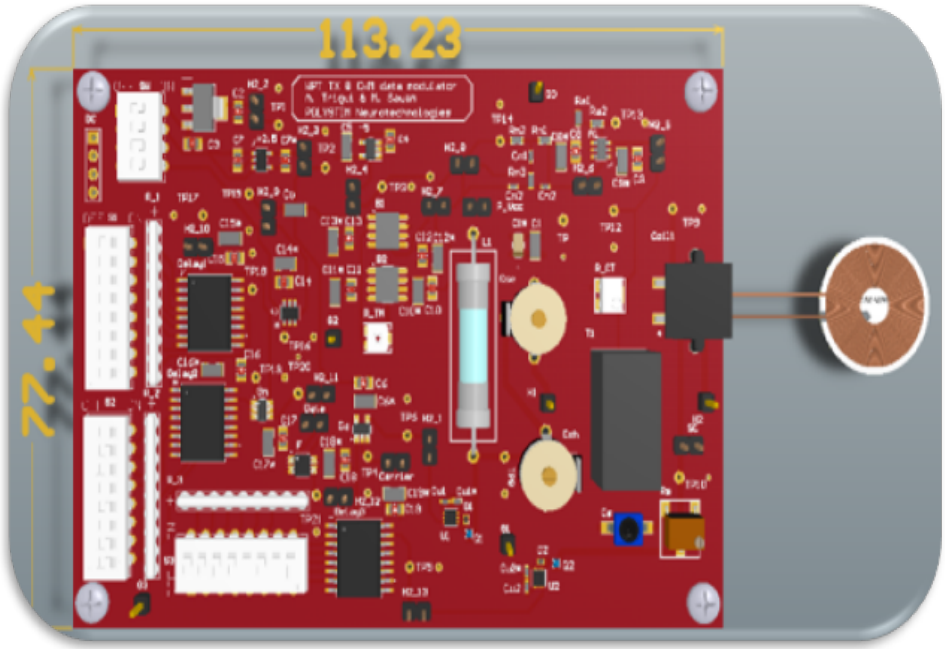

Figure C.3 3D top view of the transmitter circuit board. The dimensions are in millimiters

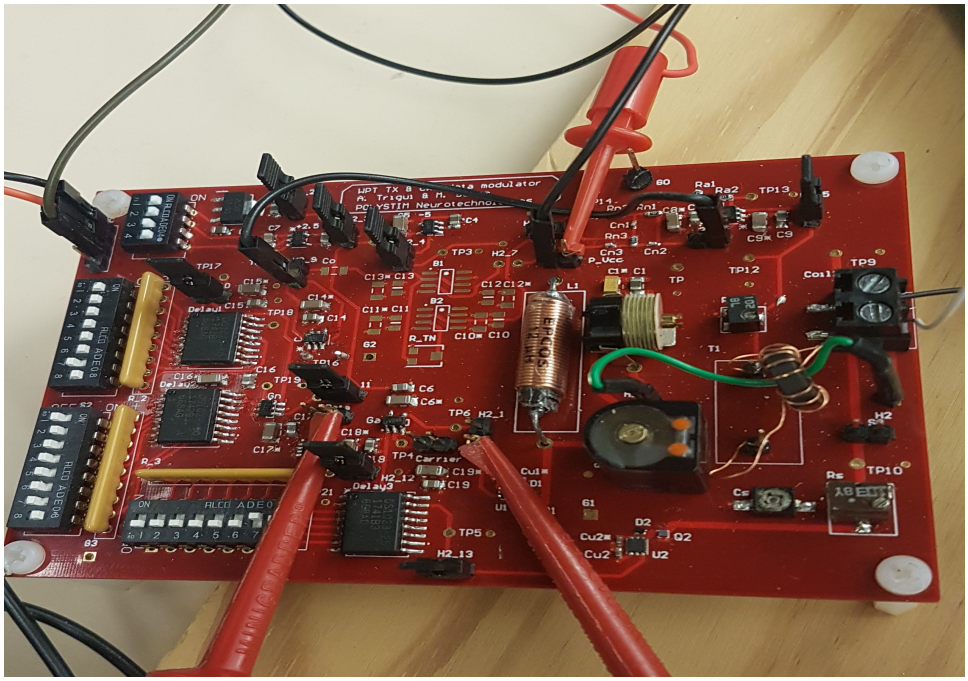

Figure C.4 Photograph of the transmitter-PCB prototype.

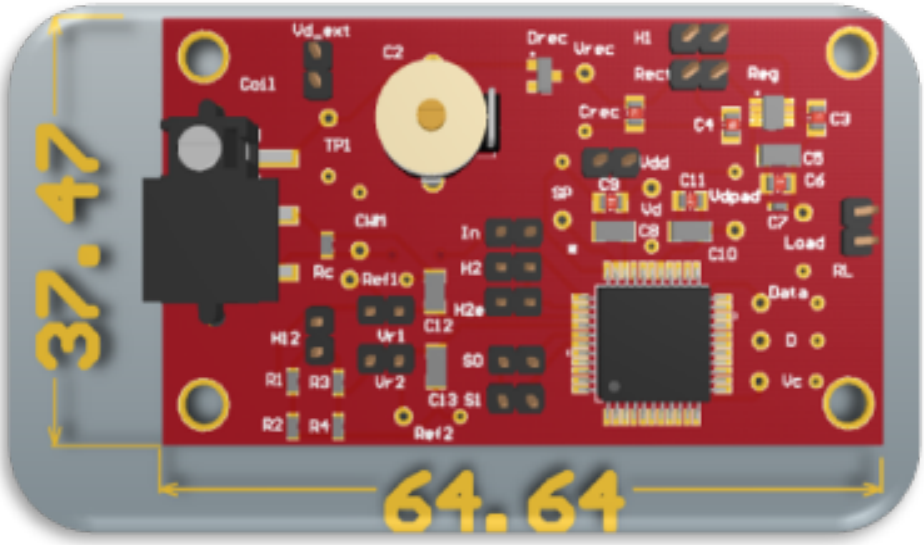

Figure C.5 3D top view of the receiver circuit board. The dimensions are in millimiters

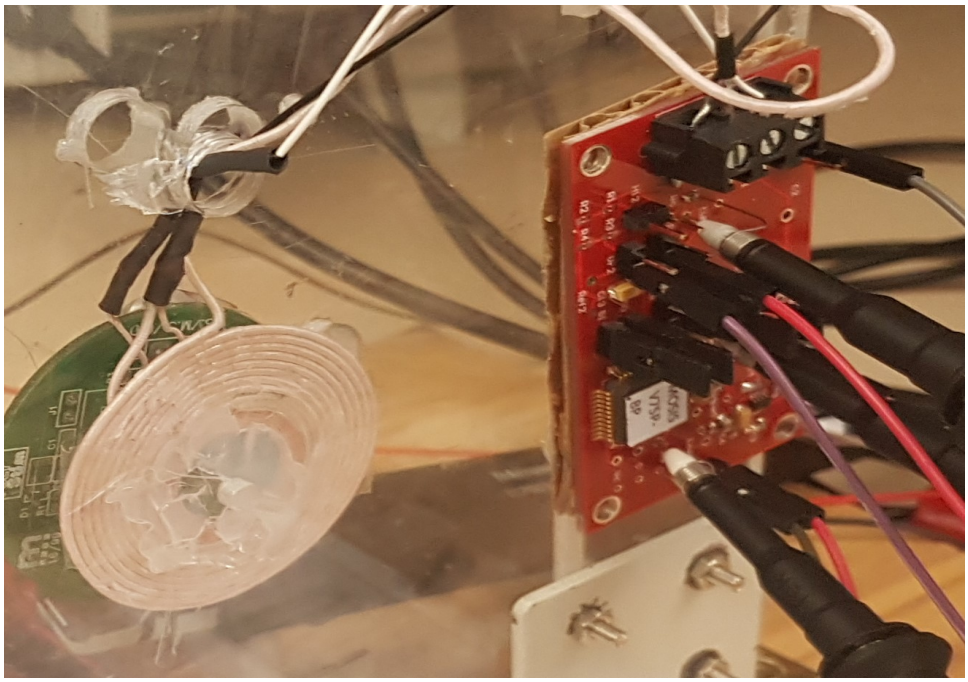

Figure C.6 Photograph of the receiver-PCB prototype.

Figure C.7 Photograph of the receiver tapped coil.